A High Repetition Rate Attosecond Light Source Based on Optical Parametric Amplification

Guo, Chen

2018

Document Version:
Publisher's PDF, also known as Version of record

A High Repetition Rate Attosecond Light Source Based on Optical Parametric Amplification

CHEN GUO

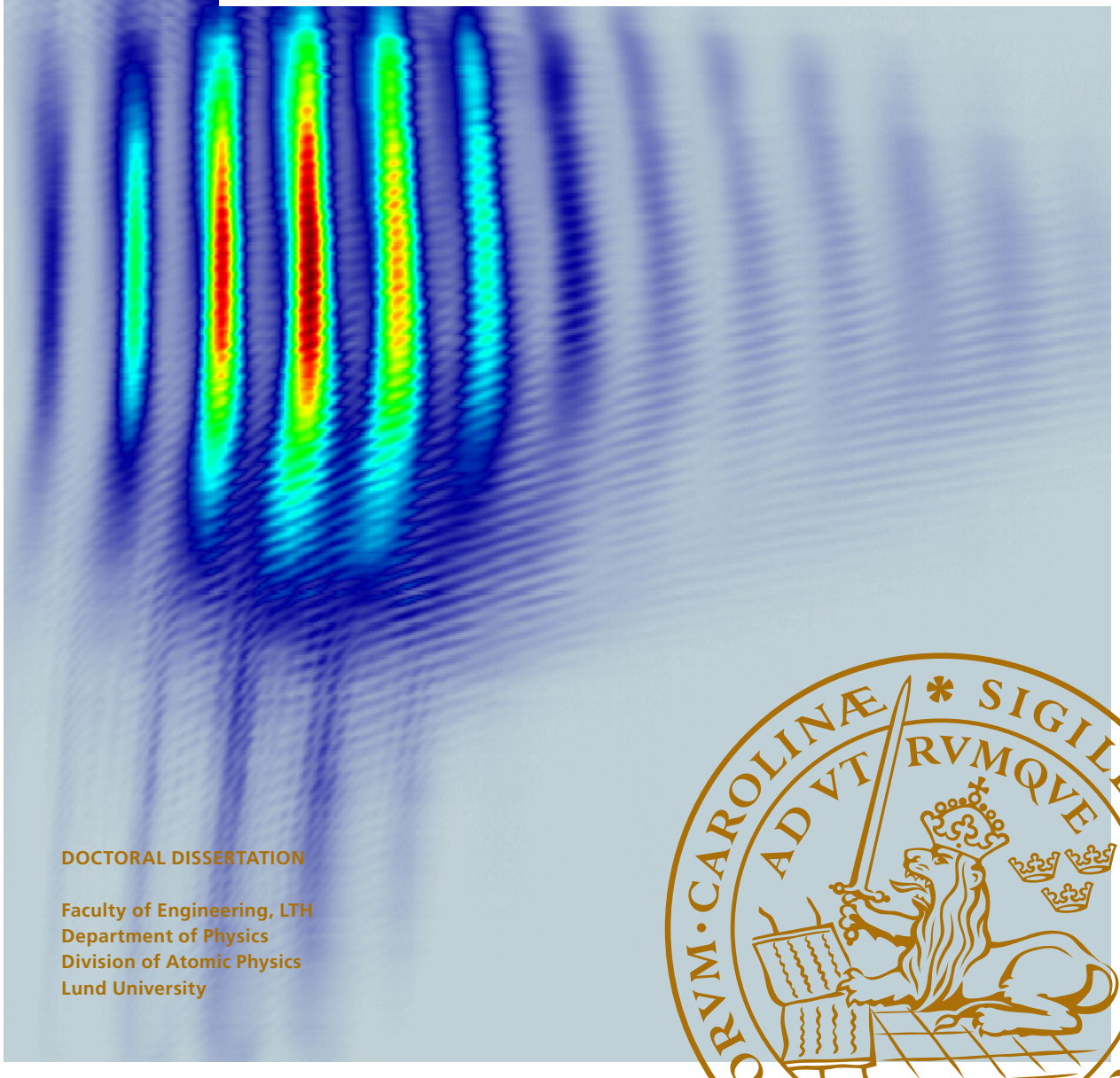

DOCTORAL DISSERTATION

Faculty of Engineering, LTH
Department of Physics
Division of Atomic Physics
Lund University

A High Repetition Rate Attosecond Light Source Based on Optical Parametric Amplification

A High Repetition Rate Attosecond Light Source Based on Optical Parametric Amplification

by Chen Guo

LUND
UNIVERSITY

Thesis for the degree of PhD in Physics
Thesis advisors: Prof. Anne L'Huillier, Dr. Cord L. Arnold, Dr. Miguel Miranda
Faculty opponent: Prof. François Légaré

To be presented, with the permission of the Faculty of Engineering, LTH of Lund University, for public criticism in Rydberg lecture hall at the Department of Physics on Friday, the 9th of February 2018 at 13:00.

Organization
LUND UNIVERSITY
Atomic Physics
Box 118
SE–221 00 LUND
Sweden

Document name
DOCTORAL DISSERTATION
Date of disputation
2018-02-09
Sponsoring organization

Author(s)
Chen Guo

Title and subtitle
A High Repetition Rate Attosecond Light Source Based on Optical Parametric Amplification

Abstract
This thesis focuses on the generation, characterization and application of ultrashort light pulses with a pulse duration from the femtosecond to the attosecond range. We developed an optical parametric chirped pulse amplification (OPCPA) laser system. This laser system generates few-femtosecond pulses in the near infrared (NIR) range. The laser system provides 200 kHz, sub-8 μJ, few-cycle laser pulses.

Several short pulse characterization techniques were developed. The dispersion scan technique, which enables to determine the spectral phase and therefore the pulse duration, was improved with a fast retrieval algorithm and a compact single-shot implementation. A spatially-resolved Fourier transform spectrometer was developed to measure the spatio-temporal couplings of the laser pulses, including vortex pulses.

To generate attosecond pulses, the IR pulses are tightly focused into a gas target and generate high-order harmonics. With correct conditions, the high-order harmonics can form attosecond pulse. We presents a high repetition rate extreme ultraviolet (XUV) source based on high-order harmonic generation (HHG) driven by the OPCPA laser system. The high-order harmonics are generated using noble gases, such as neon, argon and krypton. Furthermore, HHG was studied as a function of dispersion of the fundamental pulse. The HHG spectra were explained and reproduced by a multiple pulse interference model.

Both the IR and XUV light sources were applied to image nanoparticles using a photoemission electron microscopy (PEEM) setup in order to study plasmonic dynamics. We measured the electron yield obtained by absorbing multiple photons as a function of the IR polarization and time delay using an interferometric method. We obtained the first HHG-PEEM image of nanowires at a high repetition rate.

Key words
Ultrafast Optics, Optical Parametric Amplifier, High-order Harmonic Generation, Attosecond Pulse, Extreme Ultraviolet, Short Pulse Characterization

Classification system and/or index terms (if any)
42.65.Ky, 42.65.Re, 32.80.Rm, 42.65.Yj

Supplementary bibliographical information

Language
English

ISSN and key title
0281-2762

ISBN
978-91-7753-557-7 (print)
978-91-7753-558-4 (pdf)

Recipient's notes

Number of pages
247

Price

Security classification

A High Repetition Rate Attosecond Light Source Based on Optical Parametric Amplification

by Chen Guo

LUND
UNIVERSITY

A doctoral thesis at a university in Sweden takes either the form of a single, cohesive research study (monograph) or a summary of research papers (compilation thesis), which the doctoral student has written alone or together with one or several other author(s).

In the latter case the thesis consists of two parts. An introductory text puts the research work into context and summarizes the main points of the papers. Then, the research publications themselves are reproduced, together with a description of the individual contributions of the authors. The research papers may either have been already published or are manuscripts at various stages (in press, submitted, or in draft).

Cover illustration front: High-order harmonic spectra as a function of fundamental dispersion (from Paper III).

Cover illustration back: Spontaneous parametric down-conversion rings generated from the green pulses.

Funding information: The thesis work was financially supported by European Research Council (Grant PALP).

Faculty of Engineering, LTH, Atomic Physics

ISBN: 978-91-7753-557-7 (print)
ISBN: 978-91-7753-558-4 (pdf)
ISSN: <0281-2762>

Printed in Sweden by Media-Tryck, Lund University, Lund 2018

合抱之木，生于毫末；
九层之台，起于累土；
千里之行，始于足下。
— 老子

The tree which fills the arms grew from the tiniest sprout;
the tower of nine storeys rose from a (small) heap of earth;
the journey of a thousand li commenced with a single step.
— Laozi
(translated by James Legge)

Contents

Abstract

This thesis focuses on the generation, characterization and application of ultrashort light pulses with a pulse duration from the femtosecond to the attosecond range. We developed an optical parametric chirped pulse amplification (OPCPA) laser system. This laser system generates few-femtosecond pulses in the near infrared (NIR) range. The laser system provides 200 kHz, sub-8 µJ, few-cycle laser pulses.

Several short pulse characterization techniques were developed. The dispersion scan technique, which enables to determine the spectral phase and therefore the pulse duration, was improved with a fast retrieval algorithm and a compact single-shot implementation. A spatially-resolved Fourier transform spectrometer was developed to measure the spatio-temporal couplings of the laser pulses, including vortex pulses.

To generate attosecond pulses, the IR pulses are tightly focused into a gas target and generate high-order harmonics. With correct conditions, the high-order harmonics can form attosecond pulse. We presents a high repetition rate extreme ultraviolet (XUV) source based on high-order harmonic generation (HHG) driven by the OPCPA laser system. The high-order harmonics are generated using noble gases, such as neon, argon and krypton. Furthermore, HHG was studied as a function of dispersion of the fundamental pulse. The HHG spectra were explained and reproduced by a multiple pulse interference model.

Both the IR and XUV light sources were applied to image nanoparticles using a photoemission electron microscopy (PEEM) setup in order to study plasmonic dynamics. We measured the electron yield obtained by absorbing multiple photons as a function of the IR polarization and time delay using an interferometric method. We obtained the first HHG-PEEM image of nanowires at a high repetition rate.

Popular Science Summary

How fast can we follow an evolving physical phenomenon? It very much depends on the tools that we use. If we just use our eyes, the shortest time during which you can clearly see is about 0.1 second. You may have such an experience: a non-stop train passes the platform where you stand, but you can barely read any labels on the train just because it is too fast. However, if we use a camera, which can act much faster than the human eye, we can easily acquire images of the fast moving train. To illustrate this effect in a "scientific" manner, we take photographs of a movie, in which a white dot orbits around the center rapidly (figure 1(a)). In figure 1(b) and (c), two photographs of this movie are acquired with different exposure time of $1/2$ second and $1/50$ second respectively. In (b), with the relatively long exposure time, we find an arc. With this picture, we can only tell that our object has passed thorough the position of this arc, but we are not able to find its exact location on the orbit, because it moves too fast. If we decrease the exposure time to $1/50$ second, we can find there is (almost) only one circle left in the picture. Thus, with this speed, we are able to capture the position of the object as a function of time.

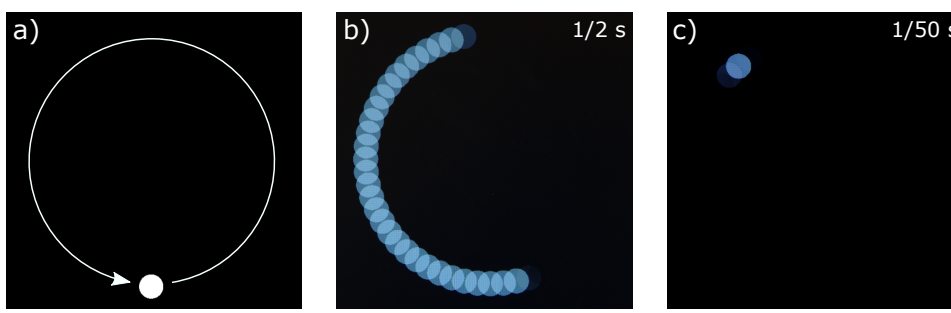

Figure 1: A simple example of how the observation depends on the temporal resolution dependent by photographing a movie on a computer screen, a) the object which is a white dot orbital rotating around the center of the picture; b) photograph taken with $1/2$ second and c) with $1/50$ second exposure time.

Now we change this dot to a real physical system, such as a classical Hydrogen atom where an electron orbits around a proton. How fast does this electron orbit? *Niels Bohr* predicted that the time for a 1s electron to make a full orbit around the nuclei is about 152 attosecond. Attosecond is a very small time unit as one quintillionth (10^{-18}) of a second. To have a feeling of how short an attosecond is, we compare one attosecond to one second: 1 attosecond is to 1 second what 1 second is to 32 billion years, which is more than the age of the universe (14 billion years)! To study the physical phenomena, such as as electron motion, at the attosecond time scale, the conventional cameras are too slow. Our approach is to use a very short laser pulse with duration in the attosecond range. This concept is similar to the flash lamp of the camera: we can still use a slow camera, but we illuminate

the object with a short flash.

To generate attosecond pulses, we use a technique, called *high-order harmonic generation* (HHG). These harmonics of the fundamental laser are analog to the harmonics in music, with a frequency equal to a multiple of the fundamental frequency. For example, the center tone A in a piano (A_4) is at 440 Hertz (oscillating 440 times per second), and the harmonics of this tone have frequencies 880 Hertz, 1760 Hertz, etc. The orders of the harmonics are the integers multiplying to the fundamental frequency. For generating attosecond pulses, harmonics are generated from femtosecond infrared (IR) pulses. In this case, the laser pulses need to be intense. At this intensity, an electron may be pulled out from the atom, gain energy from the laser and return to the parent ion. The acquired energy can be transferred to the new light during a very short time. In other words, arrosecond pulses are generated. However, this technique has very low conversion efficiency. Typically only 0.001% of the laser energy can be converted into attosecond pulses.

This thesis describes the development of an arrosecond light source with very high repetition rate (200 000 shots per second). To achieve the goal we used an IR laser system with optical parametric chirped pulse amplification (OPCPA) technology to drive the HHG process. We developed several tools for measuring and optimizing the laser system. We also designed a novel high-pressure gas jet to maximize the efficiency of our HHG setup. We studied the HHG process by varying the shape of the driving IR field. We used this laser system for time-resolved studies of nano structures.

List of publications

This thesis is based on the following publications, referred to by their Roman numerals:

I **Compact 200 kHz HHG source driven by a few-cycle OPCPA**

Anne Harth, **Chen Guo**, Yu-Chen Cheng, Arthur Losquin, Miguel Miranda, Sara Mikaelsson, Christoph M. Heyl, Oliver Prochnow, Jan Ahrens, Uwe Morgner, Anne L'Huillier, and Cord L. Arnold
Journal of Optics, 2017, 20, 1

II **Carrier-envelope phase dependent high-order harmonic generation with a high-repetition rate OPCPA-system**

Piotr Rudawski, Anne Harth, **Chen Guo**, Eleonora Lorek, Miguel Miranda, Christoph M. Heyl, Esben W. Larsen, Jan Ahrens, Oliver Prochnow, Thomas Binhammer, Uwe Morgner, Johan Mauritsson, Anne L'Huillier, and Cord L. Arnold
The European Physical Journal D, 2015, 69, 1

III **Phase Control of Attosecond Pulses in a Train**

Chen Guo, Anne Harth, Stefanos Carlström, Yu-Chen Cheng, Sara Mikaelsson, Erik Mårsell, Christoph M. Heyl, Miguel Miranda, Mathieu Gisselbrecht, Mette B. Gaarde, Kenneth J. Schafer, Anders Mikkelsen, Johan Mauritsson, Cord L. Arnold and Anne L'Huillier
Journal of Physics B: Atomic, Molecular and Optical Physics, 2017

IV **Fast iterative retrieval algorithm for ultrashort pulse characterization using dispersion scans**

Miguel Miranda, João Penedones, **Chen Guo**, Anne Harth, Maïté Louisy, Lana Neoričić, Anne L'Huillier and Cord L. Arnold
Journal of the Optical Society of America B: Optical Physics, 2017, 56, 9084

V **Compact single-shot d-scan setup for the characterization of few-cycle laser pulses**

Maïté Louisy, **Chen Guo**, Lana Neoričić, Shiyang Zhong, Anne L'Huillier, Cord L. Arnold and Miguel Miranda
Applied Optics, 2017, 56, 9084

VI **Spatiotemporal characterization of ultrashort laser pulses using spatially resolved Fourier transform spectrometry**

Miguel Miranda, Marija Kotur, Piotr Rudawski, **Chen Guo**, Anne Harth, Anne L'Huillier and Cord L. Arnold
Optics Letters, 2014, 39, 5142

VII **Spatiotemporal characterization of ultrashort optical vortex pulses**

Miguel Miranda, Marija Kotur, Piotr Rudawski, **Chen Guo**, Anne Harth, Anne L'Huillier and Cord L. Arnold
Journal of Modern Optics, 2016, 64, 1

VIII **Direct subwavelength imaging and control of near-field localization in individual silver nanocubes**

Erik Mårsell, Robin Svärd, Miguel Miranda, **Chen Guo**, Anne Harth, Eleonora Lorek, Johan Mauritsson, Cord L. Arnold, Hongxing Xu, Anne L'Huillier, Anders Mikkelsen and Arthur Losquin
Applied Physics Letters, 2015, 107, 201111

IX **Size and shape dependent few-cycle near-field dynamics of bowtie nanoantennas**

Eleonora Lorek, Erik Mårsell, Arthur Losquin, Miguel Miranda, Anne Harth, **Chen Guo**, Robin Svärd, Cord L. Arnold, Anne L'Huillier, Anders Mikkelsen and Johan Mauritsson
Optics Express, 2015, 23, 31460

X **Nanoscale imaging of local few-femtosecond near-field dynamics within a single plasmonic nanoantenna**

Erik Mårsell, Arthur Losquin, Robin Svärd, Miguel Miranda, **Chen Guo**, Anne Harth, Eleonora Lorek, Johan Mauritsson, Cord L. Arnold, Hongxing Xu, Anne L'Huillier and Anders Mikkelsen
Nano Letters, 2015, 15, 6601

XI **Imaging Localized Surface Plasmons by Femtosecond to Attosecond Time-Resolved Photoelectron Emission Microscopy –"ATTO-PEEM"**

Soo Hoon Chew, Kellie Pearce, Christian Späth, Alexander Guggenmos, Jürgen Schmidt, Frederik Süßmann, Matthias F. Kling, Ulf Kleineberg, Erik Mårsell, Cord L. Arnold, Eleonora Lorek, Piotr Rudawski, **Chen Guo**, Miguel Miranda, Fernando Ardana, Johan Mauritsson, Anne L'Huillier and Anders Mikkelsen
Attosecond Nanophysics, Wiley-VCH Verlag GmbH & Co. KGaA, 2014, 325-364

Abbreviations

ADK	Ammosov–Delone–Kraĭnov
AMO	Atomic, Molecular and Optical
APD	Avalanche PhotoDiode
BBO	β-Barium Borate
CCD	Charge-Coupled Device
CEP	Carrier-Envelope Phase
CFBG	Chirped Fiber Bragg Grating
CIEL	Coincidences entre Ions et Electrons Localisés
CPA	Chirped Pulse Amplification
DAZZLER	Acousro-optic Programmable Dispersive Filter
DC	Direct Current
DCM	Double Chirped Mirror
DFG	Different Frequency Generation
d-scan	Dispersion Scan
DSMC	Direct Simulation Monte Calro
FA	Fiber Amplifier
FDTD	Finite Difference Time Domain
FEL	Free Electron Laser
FFT	Fast Fourier Transform
FOPA	Frequency-domain Optical Parametric Amplification
FROG	Frequency Resolved Optical Gating
FROG-CRAB	Frequency Resolved Optical Gating for Complete Reconstruction of Attosecond Bursts
FWHM	Full Width at Half Maximum
FWM	Four Wave Mixing
GDD	Group Delay Dispersion
HHG	High-order Harmonic Generation
ImXFROG	Imaging Cross-correlation Frequency-Resolved Optical Gating
IR	Infrared Radiation
IS-PEEM	Integral Sample Stage PhotoEmission Electron Microscope
ITO	Indium Tin Oxide
LLC	Lund Laser Center
MCP	Micro Channel Plate
MIIPS	Multiphoton Intrapulse Interference Phase Scan
NA	Numerical Aperture
NIR	Near Infrared Radiation

NOPA	Noncollinear Optical Parametric Amplifier
OA	Optical Axis
OPA	Optical Parametric Amplification
OPCPA	Optical Parametric Chirped Pulse Amplification
PD	PhotoDiode
PEEM	PhotoEmission Electron Microscopy
PLL	Phase Lock Loop
RABBIT	Reconstruction of Attosecond Beating By Interference of Two-photon transitions
RMS	Root-Mean-Square
SEA-SPIDER	Spatially Encoded Arrangement for Spectral Phase Interference for Direct Electric-field Reconstruction
SEA-TADPOLE	Spatially Encoded Arrangement for Temporal Analysis by Dispersing a Pair Of Light E-fields
SEM	Scanning Electron Microscope
SFA	Strong Field Approximation
SFG	Sum Frequency Generation
SHG	Second Harmonic Generation
SLM	Single Liquid-crystal Modulator
SNR	Signal-to-Noise Ratio
SPDC	Spontaneous Parametric Down-Conversion
SPIDER	Spectral Phase Interference for Direct Electric-field Reconstruction
SRS	Stimulated Raman Scattering
TDSE	Time-Dependent Schrödinger Equation
THG	Third Harmonic Generation
Ti:Sa	Titanium-doped Sapphire
TOD	Third Order Dispersion
UV	Ultraviolet
XPM	Cross-Phase Modulation
XUV	Extreme Ultraviolet

Chapter 1

Introduction

Since the invention of the laser in 1960 [1], nonlinear interactions between light and matter have become feasible due to the high intensity of the laser beam and the first optical harmonic was observed in 1961 [2]. After almost 60 years of development of laser technology, including mode-locking [3], laser pulses from a laser oscillator have become as short as few femtoseconds [4]. In parallel, the chirped pulse amplification (CPA) technique [5], together with titanium-doped sapphire (Ti:Sa) crystals, have allowed the amplification of short laser pulses while maintaining the pulse duration and the observation of high laser intensities, thus opening the door to strong-field physics phenomena. However, due to the energy level configuration of Ti:Sa, the thermal management is challenging and limits the repetition rate of this type of system to a few kHz. To achieve higher repetition rate, new laser media have to be implemented. In recent years, ytterbium (Yb) laser systems have successfully achieved high average power at high repetition rate due to the low quantum defect [6]. The pulse duration from the ytterbium system cannot, however, go below hundreds femtoseconds due to the narrow amplification bandwidth. To reach shorter pulses, one method is to implement post-compression techniques, with which 6.3 fs pulses have been demonstrated [7]. Another approach is to use high-power lasers to pump an optical parametric chirped pulse amplification (OPCPA) system, so that energy can be transferred to short pulses with nonlinear effects [8]. Recently, several high power OPCPA laser systems based on different pump laser technologies have been reported [9–11].

Currently, the pulse duration from conventional visible-infrared ultrafast lasers is limited to a few femtoseconds. According to the uncertainty principle, the spectral bandwidth of an ultrafast pulse with a single cycle duration is comparable to the central frequency of this pulse. The large bandwidth needed to reach even shorter pulses is unpractical to handle. This is known as the "single-cycle limitation". To achieve pulse duration in the attosecond (<1 fs) range, the central frequency has to be shifted to the ultraviolet (UV), extreme ultra-

violet (XUV) or even soft X-ray domain. A technical issue is that there is no suitable laser medium with enough bandwidth at these frequencies, so that conventional mode-locking laser technologies are not applicable. An approach is a free electron laser (FEL), which uses the relativistic radiation emission of fast-moving free electrons [12, 13]. FELs can provide very intense XUV or soft X-ray pulses, but the pulse duration is currently limited to a few femtoseconds. Furthermore, FELs are very big and expensive instruments with limited user access. An interesting alternative is to upconvert short pulses from conventional laser systems to the XUV region, using a highly nonlinear phenomenon called high-order harmonic generation (HHG). HHG, which has been observed and studied since the late 1980s [14, 15], can provide an ultrabroadband spectrum spanning from XUV to hard X-ray [16] and extreme short pulses down to 53 attoseconds [17]. HHG-based attosecond sources are used to study fundamental physics using XUV pump- IR probe schemes. Furthermore, HHG in solid targets has recently been demonstrated [18], allowing experiments of electron dynamics in condensed matter.

Some applications in attosecond science, e.g., photoemission electron microscopy (PEEM) [19] or atomic, molecular and optical (AMO) physics using coincidence measurements [20], require at most a single event per laser shot. These applications often do not need high XUV intensity, but strongly benefit from a high-repetition rate.

Aim and Outline

The aim of this PhD thesis is the *realization of a high repetition rate attosecond extreme ultraviolet source, based on high-order harmonic generation from a few-cycle optical parametric chirped pulse amplification laser, for novel applications in attosecond science.* To achieve this goal, we built and characterized a 200 kHz few-cycle OPCPA laser system (presented in the first part of **Paper I**). We used this laser to generate high-order harmonics and characterized the harmonic flux (second part of **Paper I**). We also studied the harmonics as a function of the dispersion of the driving pulses (**Paper II** and **III**). To measure the duration of ultrashort IR pulses, we developed a compact single-shot dispersion scan (d-scan) setup (**Paper V**) and a fast algorithm to retrieve a d-scan trace (**Paper IV**). To characterize their spatio-temporal properties, we built a spatially-resolved Fourier transform spectrometer (**Paper VI**). This spectrometer was used to characterize a vortex pulse (**Paper VII**). The IR and XUV pulses were sent to a PEEM to study surface plasmonics in nanocubes (**Paper VIII**), bowtie nanoantennas (**Paper IX**), nanorices (**Paper X**) and metallic nanowires (**Paper XI**).

This thesis is based on these eleven papers. They are broken down into four different topics: laser system, short pulse characterization, HHG and PEEM applications, presented in chapters 2–5. As shown in figure 1.1, **Paper I** is presented in both Chapter 2, *Optical Parametric Chirped Pulse Amplification System*, and Chapter 4, *High-order Harmonic Generation*. Chapter 4 also contains the results from **Papers II** and **III**. Chapter 3, *Short Pulse Character-*

ization, discusses the pulse characterization techniques presented in **Papers IV** to **VII**. The results presented in **Papers VII** to **XI** are briefly summarized in Chapter 5, *Application: Attosecond PhotoEmission Electron Microscopy*. Finally, a conclusion and a brief outlook are given in Chapter 6.

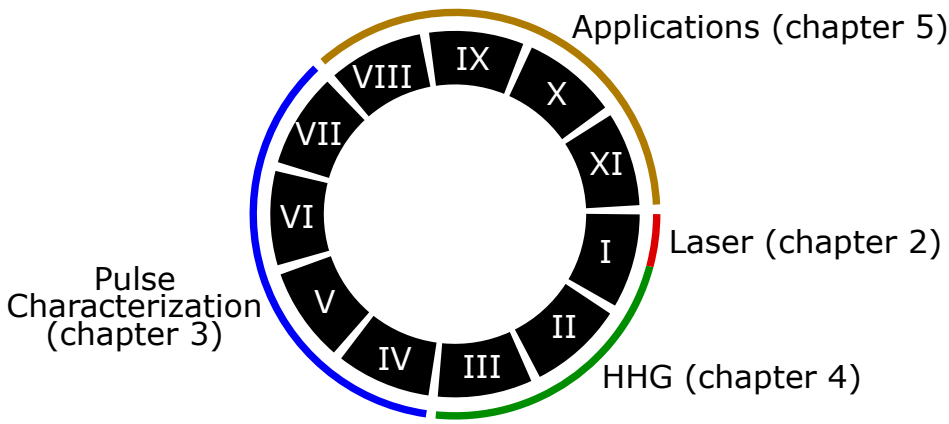

Figure 1.1: The 11 papers included in this thesis are broken down into four topics: laser system, short pulse characterization, HHG and applications.

Chapter 2

Optical Parametric Chirped Pulse Amplification System

1 Theory of Optical Parametric Amplifier for Short Pulses

An optical wave, which is an electromagnetic wave, is described by Maxwell's equations [21], relating the electric field $\vec{E}$ and magnetic field $\vec{B}$ of the wave by,

$$\nabla \cdot \vec{E} = \frac{\rho}{\varepsilon}, \qquad \text{Coulomb's law} \tag{2.1a}$$

$$\nabla \times \vec{E} = -\frac{\partial \vec{B}}{\partial t}, \qquad \text{Faraday's law} \tag{2.1b}$$

$$\nabla \cdot \vec{B} = 0, \qquad \text{Absence of free magnetic poles} \tag{2.1c}$$

$$\nabla \times \vec{B} = \mu\vec{J} + \frac{\partial(\varepsilon\mu\vec{E})}{\partial t}, \qquad \text{Ampère's law} \tag{2.1d}$$

where ρ is the charge density, $\vec{J}$ is the current density and ε and μ are the permittivity and permeability respectively. For a neutral dielectric medium, which is non-conductive and non-magnetic, ρ and $\vec{J}$ are zero and μ is equal to μ_0 which is the permeability in vacuum. The permittivity ε is often described as $\varepsilon_0(1+\chi)$, where ε_0 is the permittivity in vacuum and χ is the susceptibility of the medium. The susceptibility describes the polarization, $\vec{P}$, induced by the field, i.e. $\vec{P} = \varepsilon_0\chi\vec{E}$. Therefore, $\varepsilon\vec{E}$ can be replaced by $\varepsilon_0\vec{E} + \vec{P}$. By calculating the curl of equation 2.1b, inserting equation 2.1d on the right side of equation

2.1b, equation 2.1b becomes a wave equation with a source term,

$$\nabla^2\vec{E} - \mu_0\varepsilon_0\frac{\partial^2\vec{E}}{\partial t^2} = \mu_0\frac{\partial^2\vec{P}}{\partial t^2} \tag{2.2}$$

For a medium responding only linearly to the electric field, χ is a constant. Thus, equation 2.2 can be simplified to,

$$\nabla^2\vec{E} - \frac{n^2}{c_0^2}\frac{\partial^2\vec{E}}{\partial t^2} = 0 \tag{2.3}$$

where c_0 is speed of light in vacuum given by $1/\sqrt{\mu_0\varepsilon_0}$ and n is the refractive index equal to $\sqrt{1+\chi}$. A general solution of this equation is a traveling plane wave given by,

$$\vec{E}(\vec{r},t) = \vec{E}_0\exp(-i\omega t + i\vec{k}\vec{r}) \tag{2.4}$$

where $\vec{E}_0$ is the amplitude, ω is the angular frequency of the wave and $\vec{k}$ is the wave vector that points in the direction of propagation, with magnitude equal to $n\omega/c_0$. In principle, an arbitrary optical field can be decomposed as a superposition of plane waves by Fourier transform in both space and time.

1.1 An Ultrafast Introduction to Ultrafast Optics

An ultrashort optical pulse requires a broadband spectrum, where the minimum bandwidth is limited by the uncertainty principle,

$$\Delta\omega\cdot\Delta t \geq \frac{1}{2}. \tag{2.5}$$

where $\Delta\omega$ and Δt are the standard deviation of the spectrum and the temporal intensity structure. When $\Delta\omega\cdot\Delta t = 1/2$, the pulse is called Fourier limited. Under this condition, the pulse achieves the highest intensity and the shortest duration. It should be noted that when using the full width at half maximum (FWHM) width, this relation should be modified. For example, a Gaussian pulse follows $\Delta\omega_{\mathrm{FWHM}}\Delta t_{\mathrm{FWHM}} \geq 2.76$.

The temporal profile of the pulse is determined by both the spectrum and the spectral phase. The spectral phase, $\Phi(\omega)$, can be Taylor expanded around the central frequency, ω_0, as

$$\Phi(\omega) = \Phi_0 + \left.\frac{\mathrm{d}\Phi}{\mathrm{d}\omega}\right|_{\omega_0}(\omega-\omega_0) + \frac{1}{2}\left.\frac{\mathrm{d}^2\Phi}{\mathrm{d}\omega^2}\right|_{\omega_0}(\omega-\omega_0)^2 + \frac{1}{6}\left.\frac{\mathrm{d}^3\Phi}{\mathrm{d}\omega^3}\right|_{\omega_0}(\omega-\omega_0)^3 + \cdots \tag{2.6}$$

The first term, Φ_0, is a phase constant. By varying this phase term, the carrier-envelope phase (CEP), which is the phase delay between the peak of the pulse intensity profile to the peak of the electric field, can be changed accordingly. We should note that Φ_0 can be

directly transferred to the CEP, but not vice versa. This is because the CEP depends on the exact waveform, which can be influenced by other phase terms. The second term in equation 2.6 determines the temporal translation of the envelope, known as the group delay. The third term, the quadratic term, is the group delay dispersion (GDD), implying that different frequency components appear at different times, leading to a frequency ramping, known as chirp, in the temporal domain. The last term is the third order dispersion (TOD). The influences from TOD and higher order terms are not intuitive. Higher order dispersion often leads to a complex temporal structure with satellite pulses.

1.2 Nonlinear Effects and Coupled Wave Equations

The polarization, $\vec{P}$, induced by the external field originates from the displacement of the electrons in the medium. For strong fields, the displacement does not follow linearly to the field. The response of the medium is nonlinear and the polarization can be described by a polynomial in power of the electric field, $\vec{E}$, as,

$$\vec{P} = \varepsilon_0(\chi^{(1)}\vec{E} + \chi^{(2)}\vec{E}^2 + \chi^{(3)}\vec{E}^3 + \cdots) \tag{2.7}$$

where $\chi^{(1)}$, $\chi^{(2)}$ and $\chi^{(3)}$ are the linear, second order and third order susceptibility respectively. For birefringence media, these susceptibilities become tensors, which describe the coupling between the different polarization directions.

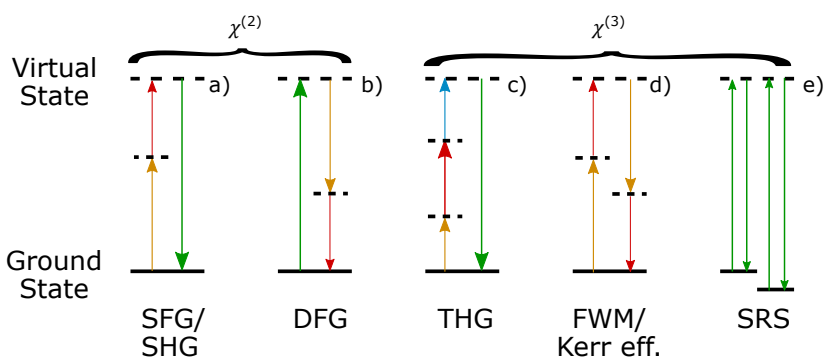

Figure 2.1: Photon representation of nonlinear processes, (a) Sum Frequency Generation (SFG) or Second Harmonic Generation (SHG), (b) Different Frequency Generation (DFG), (c) Third Harmonic Generation (THG), (d) Four Wave Mixing (FWM) or Kerr effect and (e) Stimulated Raman Scattering (SRS). The real states are indicated as solid lines and the virtual states are indicated as dashed lines.

The nonlinear interactions are wave mixing processes. In a quantum picture, wave mixing can be photon absorption and/or emission between levels or virtual levels as shown in 2.1. $\chi^{(2)}$ processes are presented in (a) and (b). The sum frequency generation (SFG) is a phenomenon where two photons are combined and a photon with energy equal to the sum of the energy of the initial photons is generated. When the two initial photons are

identical, this process is also called second harmonic generation (SHG). The reversed process of SFG, where one high energy photon is split into two photons, can be implemented in a few different ways depending on the initial conditions, leading to different frequency generation (DFG), optical parametric amplification (OPA) and spontaneous parametric down-conversion (SPDC). The third order process ($\chi^{(3)}$ process) involves many phenomena such as (c) third harmonic generation (THG), (d) four wave mixing (FWM) and (e) stimulated Raman scattering (SRS). FWM is a coupling process between four waves, which allows the generation of new frequency components. In SRS, the two different ground states are coupled by a virtual upper state. This effect behaves similarly to the FWM process, but a fundamental difference is that SRS involves energy storage in the medium. We can distinguish between parametric and non-parametric processes, where a parametric process (such as SFG) does not involve energy storing in the medium.

To demonstrate how the nonlinear response of the medium to the field leads to wave mixing phenomena, we calculate the second order nonlinear polarization for two laser fields in the medium. We assume that these two fields are cosine waves. They are described by their amplitude E_1, E_2 and frequency ω_1, ω_2 respectively. Thus, the second-order polarization (P_{NL}) is

$$P_{\mathrm{NL}} = \varepsilon_0 \chi^{(2)} \left(E_1 \cos(\omega_1 t) + E_2 \cos(\omega_2 t)\right)^2 \tag{2.8a}$$

$$= \frac{\varepsilon_0 \chi^{(2)}}{2} [\underbrace{E_1^2 + E_2^2}_{\text{DC term}} + \underbrace{E_1^2 \cos(2\omega_1 t) + E_2^2 \cos(2\omega_2 t)}_{\text{SHG}} + \underbrace{2E_1 E_2 \cos((\omega_1 - \omega_2)t)}_{\text{DFG}} + \underbrace{2E_1 E_2 \cos((\omega_1 + \omega_2)t)}_{\text{SFG}}]. \tag{2.8b}$$

Four terms can be identified. The first term is the DC term. The second term oscillates at the double frequency of the incoming waves, which represents the SHG process. The last two terms yield DFG and SFG.

To propagate the waves involved in a nonlinear wave mixing, coupled wave equations must be employed [22, 23]. Here, we consider two waves $E_1(z)\exp(ik_1 z - i\omega_1 t)$ and $E_2(z)\exp(ik_2 z - i\omega_2 t)$ generating the sum frequency wave $E_3(z)\exp(ik_3 z - i\omega_3 t)$ with $\omega_3 = \omega_1 + \omega_2$. E_1, E_2 and E_3 are often referred to signal, idler and pump respectively. The

1D coupled equations in complex form are given by,

$$\frac{\mathrm{d}E_1(z)}{\mathrm{d}z} = i\frac{\omega_3\chi^{(2)}}{n_3c_0}E_3(z)E_2^*(z)\exp(-i\Delta kz) \tag{2.9a}$$

$$\frac{\mathrm{d}E_2(z)}{\mathrm{d}z} = i\frac{\omega_3\chi^{(2)}}{n_3c_0}E_3(z)E_1^*(z)\exp(-i\Delta kz) \tag{2.9b}$$

$$\frac{\mathrm{d}E_3(z)}{\mathrm{d}z} = i\frac{\omega_3\chi^{(2)}}{n_3c_0}E_1(z)E_2(z)\exp(i\Delta kz) \tag{2.9c}$$

with,

$$\Delta k = k_1 + k_2 - k_3. \tag{2.10}$$

Obviously, E_1, E_2 and E_3 are strongly coupled. These equations are usually solved numerically, to simulate the nonlinear interactions [24].

1.3 Phase Matching

When the generated field is much weaker than the two input fields, energy conversion is negligible, so that $E_1(z)$ and $E_2(z)$ can be assumed to be constant. Equation 2.9c can be solved analytically,

$$E_3(z) = i\frac{\omega_3\chi^{(2)}}{n_3c_0}E_1E_2L\exp(i\frac{\Delta kL}{2})\mathrm{sinc}\frac{\Delta kL}{2} \tag{2.11}$$

where L is the length of the medium.

This expression shows that the generation efficiency is optimized when $\Delta k = 0$. Under this condition, the generated wave from each position along the propagation axis is in phase with the wave propagated from previous position in the medium, which is called phase matching. In a quantum picture, phase matching implies photon momentum conservation, which is simply expressed by multiplying equation 2.10 by $\hbar$. The phase matching conditions are generally not straightforward to achieve due to the dispersion of the medium. One approach is to use a birefringent crystal as a nonlinear medium. In this case, the refractive index for a certain polarization ("extraordinary wave") can be tuned by changing the orientation of the crystal and the wavenumber (k) is changed accordingly, so that phase matching can be achieved at a certain orientation. Another approach is to use non-collinear geometry. For non-collinearly propagation waves, equation 2.10 must be written in vector form, i.e.,

$$\Delta\vec{k} = \vec{k}_1 + \vec{k}_2 - \vec{k}_3. \tag{2.12}$$

Thus, by choosing certain propagation directions, it is also possible to achieve phase matching.

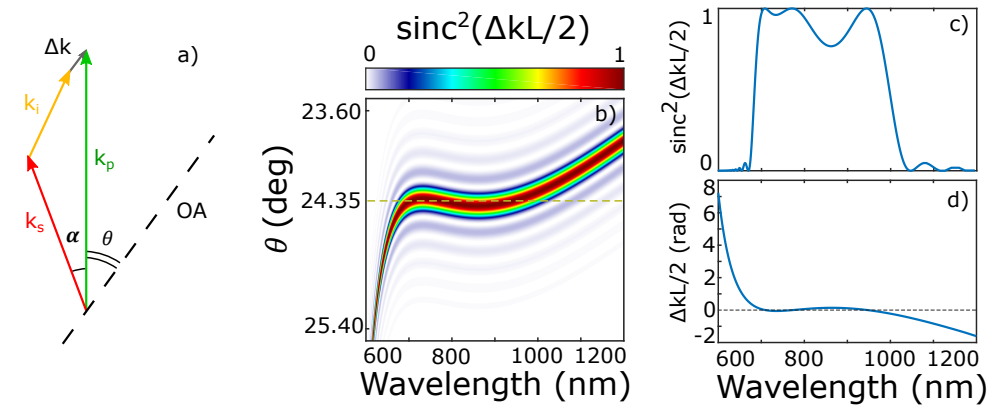

Figure 2.2: Non-collinear phase matching for BBO. (a) shows the optical axis (OA), the wavevectors for the pump (k_p), the signal (k_s), the idler (k_i) and the phase mismatch (Δk). (b) is the phase matching map ($\mathrm{sinc}^2(\Delta kL/2)$) for $\alpha = 2.44°$ as a function of signal wavelength and phase matching angle θ. (c) and (d) present the phase matching spectrum ($\mathrm{sinc}^2(\Delta kL/2)$) and phase mismatch $\Delta kL/2$ as a function of signal wavelength.

The OPCPA laser system requires a broadband phase matching condition to support sub-7 fs pulses. In our system, broadband phase matching is achieved by using a β-barium borate (BBO) crystal with a "magic angle" configuration. This phase matching condition is described by two angles: the angle between the optical axis of the crystal and the pump beam θ and the angle between the pump and signal beam α, as presented in figure 2.2(a). With these two angles, the phase mismatch Δk can be determined by solving the triangle. The phase matched intensity, proportional to $\mathrm{sinc}^2(\Delta kL/2)$, for a 2 mm thick crystal at $\alpha = 2.44°$ is calculated as a function of signal wavelength and phase matching angle θ and the result is presented in figure 2.2(b). At $\theta = 24.35°$, indicated by a dashed green line, the phase matching spectrum is the broadest (see figure 2.2(c)). Due to the symmetry of the crystal, the same phase matching spectrum can be found at $\theta = -24.35°$. These two angles are, however, different due to the Poynting vector walk-off effect of the pump beam. For positive θ, the Poynting vector walk-off angle is close to α. This configuration is called Poynting vector walk-off compensated configuration, so that the seed and the pump pulses can maintain transverse overlap, leading to efficient energy conversion. In figure 2.2(d), the corresponding phase mismatch, $\Delta kL/2$, is presented. As shown in equation 2.11, this is an additional phase applied to the field as described by the term of $\exp(i\Delta kL/2)$. This phase contributes to the pulse as a TOD, leading to a reduction of the peak intensity. This effect was observed in the d-scan measurements for the OPCPA laser system and was later compensated by a pulse shaper, as presented section 3.1.

2 Optical Parametric Chirped Pulse Amplification (OPCPA) Laser System

The OPCPA laser system used in this thesis work contains three main parts: a front-end, including an oscillator and a pulse shaper, a fiber amplifier chain and a non- collinear optical parametric amplifier (NOPA).

2.1 Front-end: Oscillator and Pulse Shaper

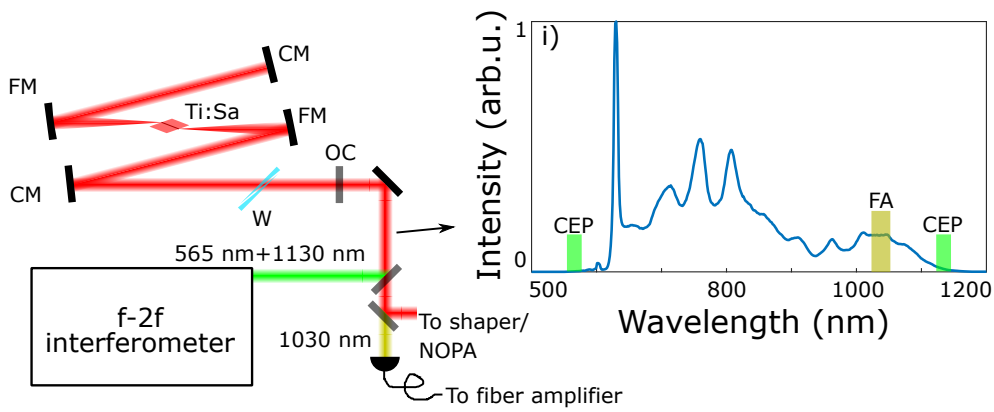

Figure 2.3: Schematic of the oscillator. CM – chirped mirror; FM – focusing mirror; W – wedge; OC – output coupler. Insert i) shows the spectrum; FA indicates the part of the spectrum around 1030 nm sent to the fiber amplifier; CEP indicates the spectra used for the CEP measurement with an f-2f interferometer.

The laser system starts from a Kerr-lens mode-locked titanium-doped sapphire (Ti:Sa) oscillator. The schematic of this oscillator is shown in figure 2.3. The cavity is an extended cavity consisting of a Ti:Sa crystal, two concave mirrors, several chirped mirrors, an output coupler, a wedge pair and a continuous pump laser centered at 532 nm. This cavity is designed to be stable when operating in mode-locking, using the Kerr-lens effect, but unstable for continuous wave operation. The Kerr effect also leads to frequency broadening so that the full gain bandwidth of the Ti:Sa crystal can be used. The oscillator spectrum, as shown in figure 2.3(i), can support a sub-5 fs pulse. The glass wedge and the chirped mirrors in this cavity are used to achieve optimized dispersion management so that the pulse is shortest in the crystal for optimized Kerr effect.

A part of the spectrum around 1030 nm, indicated in figure 2.3(i), is split to seed the fiber amplifier system, which is described and discussed in the following section. Two other parts of the spectrum, around 565 nm and 1130 nm, are split and sent to an f–2f interferometer for stabilizing the CEP. The concept of CEP stabilization is shown in figure 2.4. In the f-2f interferometer, the low frequency component is up-converted by

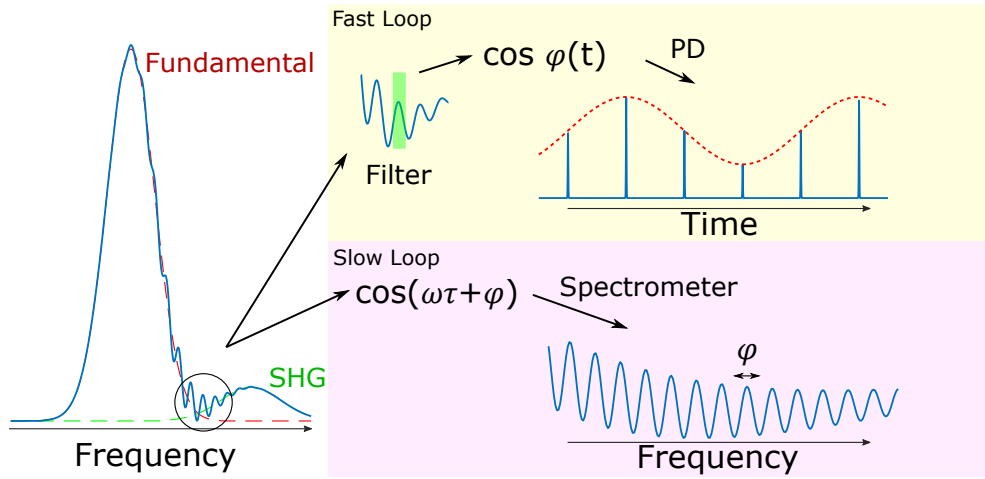

Figure 2.4: Principles of CEP stabilization using an f-2f scheme. PD – Photodiode

generating the second harmonic, which spectrally overlaps and interferes with the original component at the same frequency. The phase of the fundamental, φ, is doubled in the second harmonic, i.e. 2φ. Thus, by analyzing the interference pattern between the second harmonic and the fundamental that is proportional to $\cos\varphi$, the phase variation of the pulse can be determined, reflecting the CEP variation when there are no significant changes to the pulse structure. Technically, there are two methods for CEP detection and stabilization. In this oscillator, the intensity signal is measured as a function of time using an avalanche photodiode (APD). This method requires the fundamental pulse and the second harmonic to be temporally overlapped and uses a narrow band filter to maximize the signal-to-noise ratio of the interference signal. In the oscillator, we lock the time-dependent signal $\cos\varphi(t)$ to a reference waveform with a phase lock loop (PLL) by controlling the refractive index of the Ti:Sa crystal. The refractive index is controlled by the pump power using cross-phase modulation (XPM). The frequency of the reference wave used in this system is equal to a quarter of the repetition rate, so that the phase is the same every four pulses. The other method, which is used later in the parametric amplifier system, is based on measuring the interference pattern spectrally. In this case, a reasonable time delay τ is needed to create spectral fringes as $\cos(\omega\tau+\varphi)$. Thus, the CEP variation can be directly determined from the shifting of the fringes. The speed of this method is often limited by the speed of the spectrometer and data processing. The first technique, called "fast loop," is used in the oscillator, while the second method is implemented as a "slow loop" in the amplifier to compensate the phase drifting.

The rest of the broadband spectrum is sent to a pulse shaper including a liquid crystal modulator. This shaper, presented in figure 2.5, has a 4f geometry. In this configuration, the grating diffracts different frequency components, e.g. shown in purple and dark red in

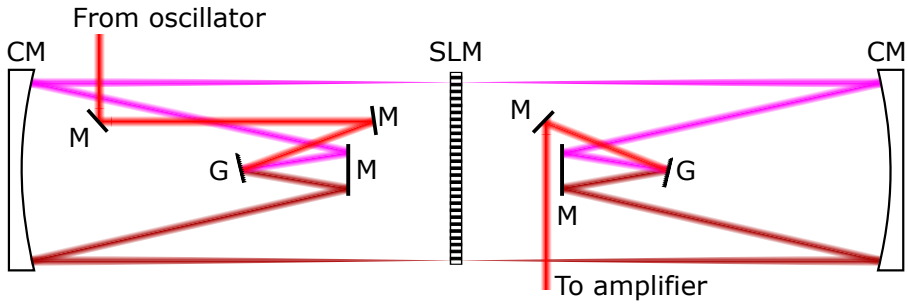

Figure 2.5: Principle of the 4f pulse shaper. M – mirror; G – grating; CM – curved mirror; SLM – single liquid-crystal modulator.

the figure 2.5, to different angles. Afterwards, a focusing mirror is placed one focal length away from the grating so that the refracted frequency components are collimated. On the other side of the setup, a replica of the focusing mirror and the grating is built so that the pulse can be reconstructed without spatial and angular distortions. A liquid crystal modulator (produced by Jenoptik) is placed in the middle of the setup, i.e., the Fourier plane, where the different frequency components are spatially separated. This liquid crystal modulator contains 640 pixels, whose index of refraction is controlled by applying voltage to each pixel. In this way, the spectral phase of the pulse can be manipulated, which helps us to compress the amplified pulses as close to the Fourier limit as possible.

2.2 Pump: Fiber Amplifier

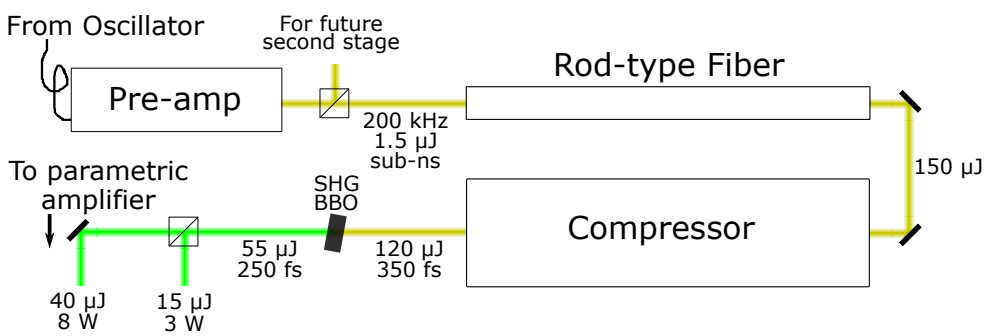

Figure 2.6: Schematics of the fiber amplifier system, as well as the second harmonic generation setup.

The schematic of the fiber amplifier system is presented in figure 2.6. The 1030 nm component is filtered out, coupled to a fiber and sent to an ytterbium-doped fiber preamplifier system. The preamplifier contains a chirped fiber Bragg grating (CFBG) stretcher, two pulse pickers and three amplifier stages. It reduces the repetition rate from 80 MHz to 200 kHz and amplifies the pulse energy from picojoule to microjoule. The beam from

the fiber amplifier is subsequently collimated and split equally to seed two main amplifier stages. Each main amplifier contains an ytterbium-doped photonic crystal rod-type fiber (NKT Photonics) individually pumped by a continuous diode laser centered at 972 nm. In **Papers I** and **III**, only the first fiber amplifier stage, indicated in figure 2.6, was used. The pulses are subsequently compressed by a grating compressor with an efficiency of 80%. The pulse duration of the compressed pulses, evaluated by an autocorrelator, is about 350 fs assuming a Gaussian pulse. The output from this stage (after compression) has a maximum power of 24 W corresponding to 120 µJ per pulse. In such an amplifier, the maximum output power is limited by output beam profile distortions, which are subsequently transferred to the second harmonic and the parametric amplifiers which we therefore want to avoid. To obtain a good beam, the coupling of the main amplifier often has to be deliberately misaligned, which also limits the amplification efficiency.

The 1030 nm beam from the fiber amplifier is subsequently converted to the second harmonic (515 nm) by using a 1 mm thick BBO crystal as the pump. The optimized second harmonic power is 11 W, corresponding to an efficiency of 46%. The pulse duration of this green pump beam is measured to be about 250 fs, using an autocorrelator. This beam is subsequently split by a beam splitter into two beams with 3 W and 8 W power to pump the first and second NOPA stages, respectively (figure 2.6). This splitting ratio is optimum for the NOPA stages to achieve the best beam quality, as discussed below in more detail.

2.3 Parametric Amplifier

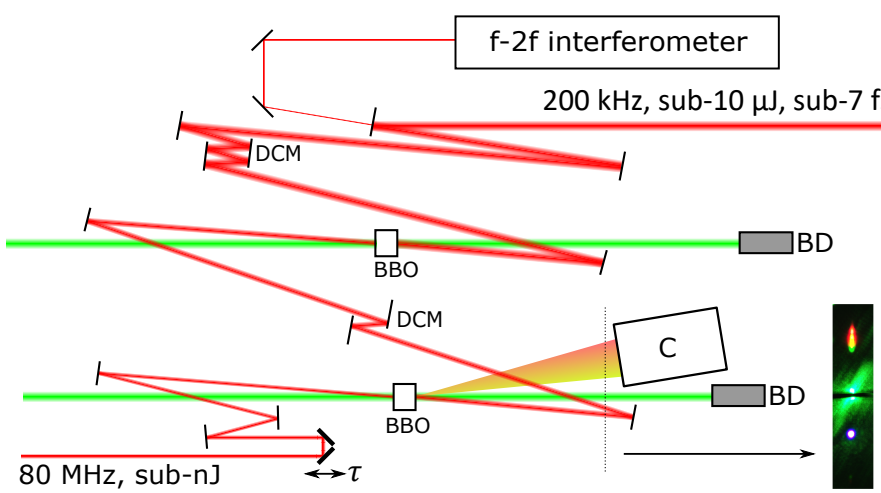

Figure 2.7: Schematics of the optical parametric amplifier. C–Camera; BD–Beam dump; DCM–Double chirped mirror.

The parametric amplifier system contains two non-collinear optical parametric stages, as presented in figure 2.7. To amplify a broadband spectrum, these two stages are implemen-

ted using the non-collinear phase matching configuration as discussed in section 1.3. The seed beam from the front-end is first delayed by two delay stages, including a motorized stage, to control and stabilize synchronization between the seed and the pump pulses for maximum amplification. Subsequently, the seed and the pump pulse are individually focused and mixed in a 2 mm thick BBO crystal. Optimization of the alignment for such a stage is not easy. The parameters for a good alignment, such as the phase matching angle θ, the non-collinear angle α, the spatial overlap and the temporal overlap, have to be adjusted iteratively. In addition, the laser characteristics, including the spectrum, output power and pulse duration, should be monitored in order to achieve the best performance. An idler beam is generated (figure 2.7) and it generates second harmonic in the visible range. This idler beam and its second harmonic are angular chirped, so that the different frequency components are separated spatially in the far field. When the delay between the seed and the pump pulses is not optimum, part of the seed spectral components does not overlap with the pump and subsequently cannot be amplified, leading to a narrow spectrum. This effect is also reflected in the idler beam. Thus, we use a camera to monitor the beam profile of the frequency doubled idler beam, which sends feedback to the motorized delay stage, allowing us to stabilize the delay drifting. Typically, the first NOPA stage amplifies the 10 mW seed signal (at 80 MHz) to 260 mW (at 200 kHz). The amplification factor is 10 000 and the conversion efficiency is 8.3%.

The second NOPA stage is configured with the same concept as the first stage. Between the two stages, a chirped mirror pair (DCM7) and a 2 mm thick fused silica plate are used to compensate the dispersion induced by the first BBO crystal and the 60 cm long air path so that the seed pulse is not stretched too much in the second BBO crystal. In optimum conditions, the second NOPA stage is pumped by 7.3 W (36 µJ per pulse) green (at 515 nm) and amplifies the seed beam to 2.3 W (11.5 µJ per pulse). This stage is designed to energy transfer, leading to a saturated amplification process, while the first stage is more close to a small signal amplifier. The saturated amplification may introduce phase jumps, structured spectrum and spatio-temporal couplings, which leads to a reduction of the peak intensity of the pulses. Hence, the optimization of this stage requires a compromise between a higher output power and a beam with good quality.

After amplification, the laser beam is compressed by a pair of chirped mirrors (DCM7). A broadband beam splitter subsequently splits about 4% of the power towards a second f-2f interferometer to monitor and stabilize the CEP drifting of the laser system (slow loop). Another pair of chirped mirrors (DCM11) is then used to pre-compensate for the dispersion up to where the high-order harmonics are generated, including a wedge pair, the entrance window for the vacuum chamber and an achromatic lens. After compression, the output power of this laser is about 1.7 W (8.5 µJ).

3 Laser Properties

3.1 Pulse Duration

The output of this laser is mostly characterized by the dispersion-scan (d-scan) technique, which is discussed in the chapter entitled *Short Pulse Characterization* in detail. The d-scan setup used in this measurement shares a motorized wedge pair with the high-order harmonic generation setup to vary dispersion of the pulses. The rest of the setup is built with the same path length in air, an identical glass window and an achromat as in the HHG setup, in order to mimic the generation condition. A 10 µm thick BBO crystal is placed in the focus where the second harmonic is generated. The second harmonic spectrum is subsequently coupled to a fiber and characterized by a spectrometer.

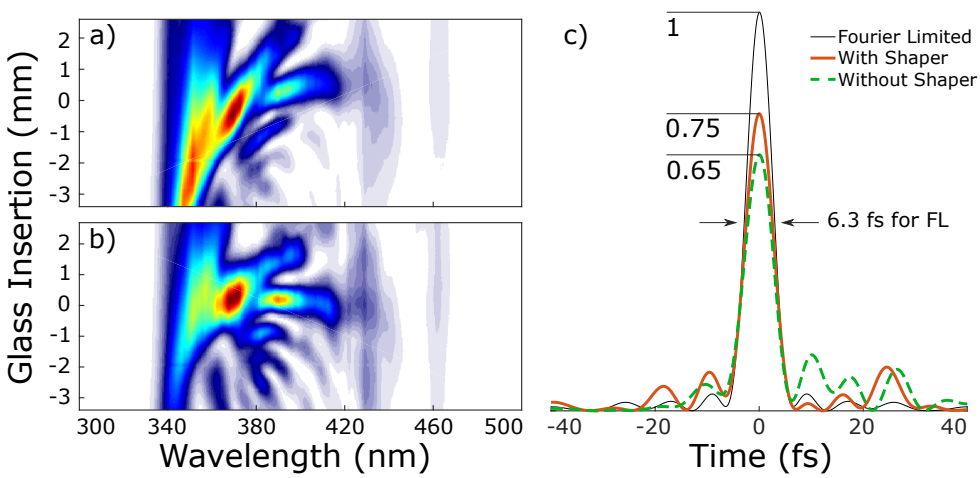

Figure 2.8: The d-scan traces with (a) a zero phase applied and (b) an optimized phase correction. In (c), the retrieved pulse structures are compared with the Fourier limited (FL) pulse.

Figure 2.8(a) shows a d-scan measurement result without using the pulse shaper. This spectrogram appears with a clear tilt, indicating strong TOD. This TOD is attributed to the phase induced by the phase matching condition (equation 2.11). By applying the opposite of retrieved phase to the shaper, the phase distortion can be pre-compensated. In practice, we applied a polynomial phase with the first five orders. This is a trade-off between a compressed pulse and a good amplified spectrum. When the retrieved phase was directly applied, we observed that the amplified spectrum became very different. The d-scan trace measured after correcting the high-order phase is presented in figure 2.8(b), where all frequency components of the second harmonic almost appear at the same glass insertion, indicating a better compression. The retrieved pulse intensity structure from the two measurements are compared to the Fourier limited pulse in figure 2.8(c). This comparison

shows that the FWHM pulse duration of these three pulses is almost the same, but the peak intensity increases from 65% to 75% of the Fourier limited pulse and the intensity of the post satellite pulses decreases, by implementing the shaper for phase correction. Since this laser is designed to drive the high-order harmonic generation, only the intensest part of the pulse participates in the generation process. Hence, it is very important to have a pulse (to remove the high-order dispersion) that is as compressed as possible for good HHG efficiency.

3.2 Spatio-temporal Coupling

As presented in figure 2.2, the different frequency components are not exactly phase matched for the same angle of propagation. The amplified beam may then have different propagation directions depending on the frequency, i.e., angular chirp. This property motivated us to develop a spatially-resolved Fourier transform spectrometer to characterize the laser pulses both spatially and temporally. The technical details of this spectrometer are presented in **Paper VI** and highlighted in chapter 3 section 2.2. In **Paper I**, we use this technique to characterize the laser pulses at the focus, and determine a 3D Strehl ratio, which is the ratio of the maximum intensity between the measured pulse and an idealized pulse, in which the spatial phase distortion is removed but the pulse energy and spatial profile are identical to the measured pulse.

Since the measurement is performed in the far field, we calculate numerically the propagation of the beam to focus by applying an angular spectrum method. Each frequency component is decomposed into the plane waves, which are propagated and recombined after propagation. This method is implemented in the following steps:

1. Transforming the complex scalar field of the beam at $z = z_0$, $E(x, y, z_0, t)$, to k_x, k_y space by a 2D-Fourier transform, $\mathfrak{F}\{\}$, i.e. $\tilde{E}(k_x, k_y, z_0, t) = \mathfrak{F}\{E(x, y, z_0, t)\}$;
2. Multiplying an angular propagator, $h(k_x, k_y, l)$, where l is the distance of propagation.
3. Finally, the field after propagation is determined by inverse Fourier transform of the new field in k-space, i.e. $E'(x, y, z_0 + l, t) = \mathfrak{F}^{-1}\{\tilde{E}(k_x, k_y, z_0, t) \cdot h(k_x, k_y, l)\}$.

The propagator, $h(k_x, k_y, l)$, describes the amplitude and phase induced by the propagation process. For an isotropic medium, the propagator, $h(k_x, k_y, l)$, is given by,

$$h(k_x, k_y, l) = \exp\left(il\sqrt{k^2 - k_x^2 - k_y^2}\right) \tag{2.13}$$

When the beam propagates within a small angle around the optical axis, i.e., $k_x, k_y \ll k$, $\sqrt{k^2 - k_x^2 - k_y^2}$ can be approximated as $k - (k_x^2 + k_y^2)/2k$, which is called paraxial or Fresnel

approximation. With this approximation, the spherical wavefront is replaced by a quadratic wavefront. Thus, the beam can be propagated analytically when using a Gaussian shape beam profile. When the beam propagates in an anisotropic medium, such as a birefringent crystal, the spherical term has to be replaced by an elliptical function to account for the refractive index dependence of the propagation direction. An alternative for these calculations would be to use diffraction integrals, which integrate the field propagated from each point in the source plane. In principle, there is no fundamental difference between these two methods, which are related by Fourier optics. In this thesis, the angular spectrum method was mostly used due to the efficient fast Fourier transform (FFT) algorithm for numerical calculations, particularly for large matrices.

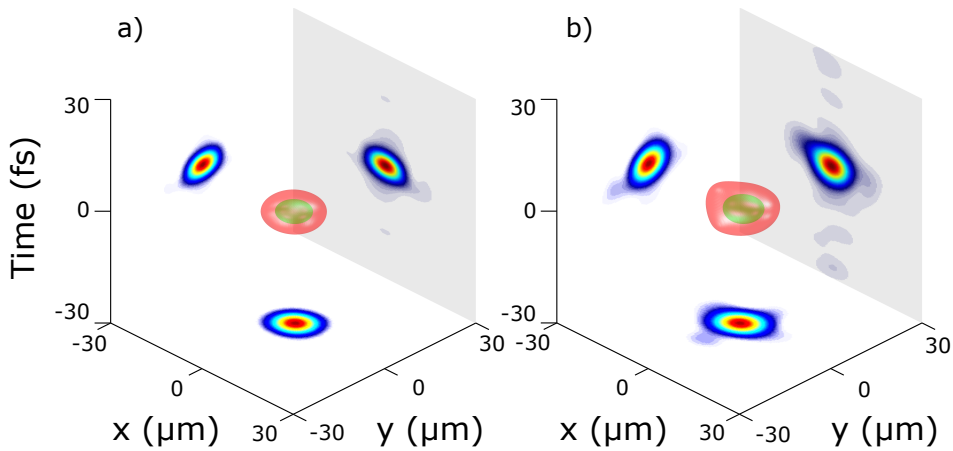

Figure 2.9: Numerically focused pulse using (a) an idealized pulse and (b) an actual pulse.

Figure 2.9(a) and (b) show the 3D plots in (x, y, t) space of actual and idealized pulses, respectively. In these two plots, the green and red isosurfaces indicate the size of the pulse at $1/2$ and $1/20$ of the maximum intensity respectively, and intensity projections are displayed in color scale at the back and bottom of the 3D plots. Compared to the idealized pulse, the energy of actual pulse spreads in a larger area in space and a longer time scale, indicating a reduction of the peak intensity. This yields us a Strehl ratio of 0.71 for this laser system. Remarkably, when we consider the intensity reduced due to higher-order dispersion (75%) measured by the d-scan (see figure 2.8), the estimated peak intensity is equal to the product of these two contributions, i.e., 53% of the possible peak intensity, which can have a considerable influence on the harmonic generation process.

We also studied the spatio-temporal couplings induced by a misaligned NOPA stage. The measurements were performed with only the first NOPA stage. Figure 2.10 compares the spatio-temporal couplings along the x-axis for a well-aligned stage and a deliberately misaligned stage by detuning the phase matching angle θ. In (a) and (c), the intensity maps in

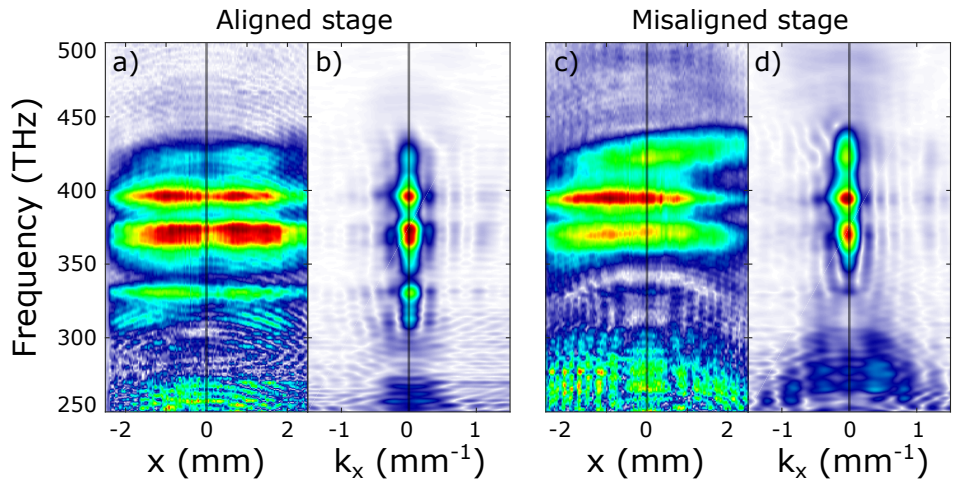

Figure 2.10: The intensity maps of a well-aligned first NOPA stage in (a) (x, ω) space and (b) (k_x, ω) space; and a misaligned first NOPA stage in (c) (x, ω) space and (d) (k_x, ω) space.

(x, ω) space are plotted for the well-aligned stage and the misaligned stage respectively. The noisy spectral components from 250 THz to 300 THz are attributed to the low quantum efficiency of the silicon based camera. In figure 2.10(a), the spectra are almost the same across the optical dimension x, indicating there is no observable spatial chirp. The misaligned stage, however, behaves differently. As shown in (c), the amplified spectrum shifts towards higher frequency and the spectra vary with x. In the (k_x, ω) space, the spectral component are aligned around $k_x = 0$ in both the aligned and the misaligned case [(b) and (d)], showing that all frequency components propagate in the same direction. This can explained as angular chirp from the amplification process is transferred to spatial chirp by collimation using the concave mirror. We also numerically focused these two pulses. The Strehl ratios were 0.81 and 0.63 for the well-aligned and misaligned stages respectively. These measurements underscore the importance of implementing spatio-temporal characterization when aligning and optimizing such a few-cycle OPCPA laser system for studying nonlinear phenomena, including high-order harmonic generation.

Chapter 3

Short Pulse Characterization

Ultrashort short pulse characterization is as crucial as the development of the ultrashort pulse source itself. A reliable short pulse characterization is required to validate the short pulse duration of the source. From an application point of view, the actual pulse shape can have crucial impact to the experimental results, so that pulse characterization is important for explaining the experimental observations. In this thesis, two types of characterization methods have been developed for determination of the spectral phase and the spatio-temporal couplings.

Direct electronic measurements of ultrashort light pulses are not feasible, because the response time for the fastest photodiode is in the range of hundreds of picoseconds and the bandwidth of a modern oscilloscope is limited to 100 GHz. Thus, direct pulse profile measurement is not possible for sub-picosecond pulses. A reference pulse with similar pulse duration is required to obtain reasonable temporal resolution. The reference pulse can be from an auxiliary source, such as a laser with well-characterized pulses, or even attosecond pulses from HHG [25]. A good alternative is to use the unknown pulse itself as reference (self-reference), which is more practical. Autocorrelation is a straightforward implementation. It can be realized by recording the second harmonic as a function of the delay between two replicas of the unknown pulse, thus providing the pulse width directly [26]. However, this method may provide faulty information. A direct alternative is to measure the spectrum of the second harmonic, instead of measuring the total intensity, which is known as frequency resolved optical gating (FROG) [27, 28]. Another commonly used method is spectral phase interference for direct electric-field reconstruction (SPIDER) [29], which is an interferometric method with nonlinear conversion. A different approach for characterizing ultrashort pulses is to measure the SHG signal while manipulating the pulses by applying additional spectral phase. For this task, multiphoton intrapulse interference phase scan (MIIPS) [30] uses a 4f pulse shaper. MIIPS characterizes short pulses by compressing

them as close to the Fourier limit as possible. MIIPS iteratively measures a trace, retrieves the scan, and applies the retrieval to a new scan until it is Fourier limited. Instead of using a 4f pulse shaper, the phase can also be controlled by different setups, such as Dazzler (chirp scan) [31] and glass wedges (dispersion scan or d-scan) [32].

Short pulses have a broad spectral range and each frequency component is often assumed to have an identical beam profile and wavefront. However, this assumption may not be valid due to diffraction, chromatic aberrations, a misaligned grating compressor or nonlinear wave mixing, etc. In this case, the pulse can have frequency-dependent optical properties, known as spatio-temporal coupling [33]. An ultrashort pulse with spatio-temporal couplings may lead to unwanted or unsatisfactory results in nonlinear interactions, due to complicated pulse structure or reduced peak intensity. However, spatio-temporal couplings can sometimes be used for certain purpose, such as rotating wavefront [34, 35] or achieving orbital angular momentum [36]. In recent works, several spatio-temporal coupling characterization methods have been reported, such as, SEA-TADPOLE [33], ImXFROG [37], SEA-SPIDER [38, 39] and the interferometric method [40].

In this thesis, the d-scan technique was further developed, with a fast retrieval algorithm (**Paper IV**) and a compact implementation of a single-shot d-scan (**Paper V**). To characterize the spatio-temporal coupling effects, an interferometric method was developed, implemented (**Paper VI**) and used to characterize the beam after going through a spiral phase plate (**Paper VII**), as well as the beam from the OPCPA laser system (**Paper I**).

1 Dispersion Scan

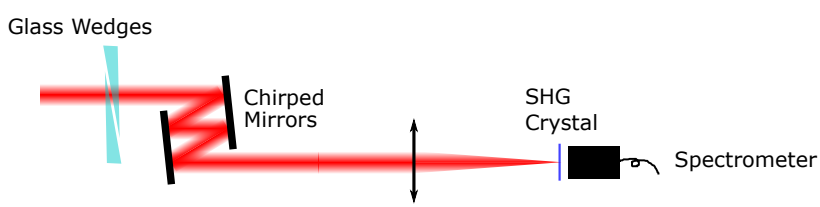

Figure 3.1: Typical d-scan setup.

The dispersion scan technique, or d-scan in short [32], consists in recording second harmonic spectra as a function of dispersion. This technique is closely related to MIIPS [30] as well as chirp scans [31]. A typical d-scan setup, presented in figure 3.1, uses a glass wedge pair and a chirped mirror compressor to vary the spectral phase of the unknown pulses. The pulses are subsequently focused into a crystal to generate the second harmonic, which is analyzed by a fiber spectrometer. Mathematically, the complex amplitude ($\tilde{A}(\omega', \ell)$) of

the pulse before generating the second harmonic is

$$A(\omega)\exp(i\Phi(\omega)+i\phi(\omega,\ell)), \tag{3.1}$$

where $A(\omega)$ and $\Phi(\omega)$ are the spectral amplitude and the phase of the unknown pulse respectively and $\phi(\omega,\ell)$ is the phase applied by the dispersion element, with an "insertion length" ℓ. When using a glass wedge, the insertion length ℓ is the physical length that the pulse passes through, i.e., $\phi(\omega,\ell)=k(\omega)\ell$ where $k(\omega)$ is the wavenumber in glass. The second harmonic field is proportional to the Fourier transform of the square of the field in the temporal domain, which can be expressed as the convolution of the spectral complex amplitude of the fundamental with itself, i.e.,

$$\tilde{A}_{\mathrm{SHG}}(\omega,\ell)=\mathfrak{F}(\tilde{U}^2(t,\ell))=\int_{-\infty}^{+\infty}\mathrm{d}\omega'\tilde{A}(\omega',\ell)\tilde{A}(\omega-\omega',\ell), \tag{3.2}$$

where $\tilde{U}(t,\ell)$ is the temporal complex field of the unknown pulse at ℓ. The convolution also distributes the field information over the SHG spectra, which increases the redundancy of the acquired spectrogram, leading to a robust retrieval. D-scan is straightforward to implement. Dispersion control elements, such as glass wedges and grating compressors, are generally mandatory for ultrafast laser systems. Hence, by simple modifications, d-scan can be easily achieved by adding a thin SHG crystal as well as a spectrometer.

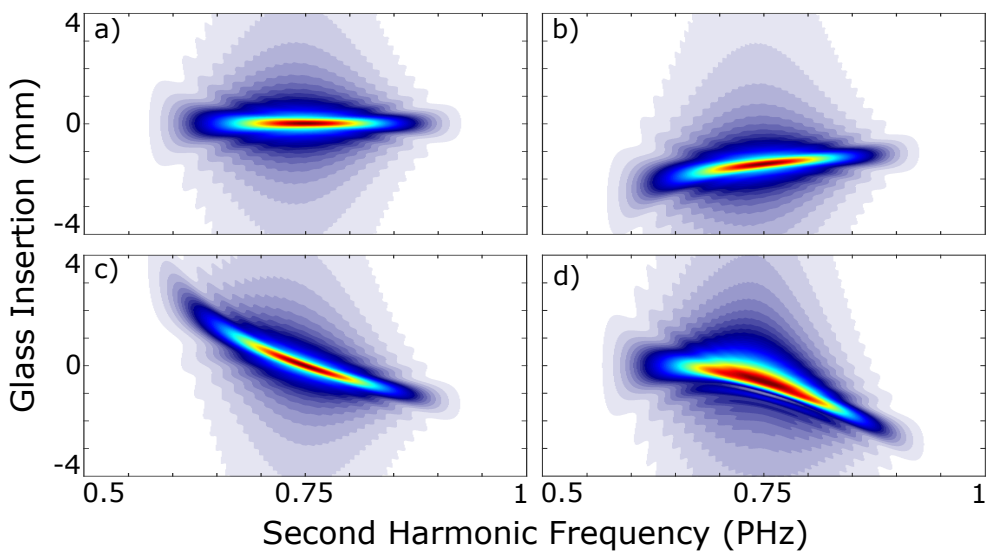

Figure 3.2: Simulations of d-scan traces: (a) ideal Gaussian pulses, (b) Gaussian pulses with positive chirp, (c) Gaussian pulses with TOD and (d) Gaussian pulses with zeros on lower frequency and chirped on higher frequency.

To demonstrate the sensitivity of the d-scan technique, a few simulated examples are presen-

ted in figure 3.2. The dispersive element is set to be BK7 glass, which is very common used in our laboratory. In figure 3.2(a), an ideally compressed Gaussian pulse is used to generate a d-scan trace, where it is obvious that the second harmonic spectra have a maximum at zero glass insertion for all frequency components. By applying a positive quadratic phase, or a positive chirp, the trace looks similar to the ideal one, but shifts towards negative glass insertion, as seen in figure 3.2(b). This is because the "negative" glass insertion compensates the positive chirp applied to the pulse. The bending of the d-scan trace can be attributed to the TOD induced by the glass. In figure 3.2(c), additional TOD is applied to the fundamental field. The d-scan trace is tilted, indicating that the different frequency components are locally compressed at different glass insertions. In figure 3.2d, a special phase is applied: at the lower frequency side, the phase is constant zero, but at the higher frequency side, the phase is set to be quadratic. The d-scan trace appears with a complicated structure, which is hard to understand intuitively. However, we can see that the phase applied to the higher frequency side also influences the lower frequencies, which come from the convolution in equation 3.2. This property allows us to retrieve the phase, even if the trace is partly cut, due to phase matching of the SHG crystal and/or contamination from the fundamental field.

Retrieval

The retrieval algorithm for the d-scan is relatively complicated. The common method is an iterative algorithm [41] that minimizes the error between the measurement and the simulated traces. At each iteration this algorithm applies a new phase by modifying the previous one. This method is robust but computationally inefficient. With the standard retrieval method, a typical retrieval requires a few tens of seconds to a few minutes. For a real-time diagnostic, this is too slow, which led us to develop a faster retrieval algorithm. In **Paper IV**, a fast retrieval algorithm is demonstrated. This method is similar to the ptychography method which is used to determine phase information from a diffraction image [42]. This method can decrease the retrieval time to only a few seconds.

This new algorithm retrieves a d-scan trace, $S_{\mathrm{SHG}}(\omega, \ell)$, in the following steps:

1. Give a first guess of the fundamental complex amplitude, $\tilde{A}(\omega)$;
2. Apply the spectral phase corresponding to glass insertions ℓ to the fundamental field; then convert this field to time domain by inverted Fourier transform, i.e., $\tilde{U}(t, \ell) = \mathfrak{F}^{-1}\{\tilde{A}(\omega)\exp(i\phi(\omega, \ell))\}$, where $\mathfrak{F}\{\}$ is Fourier transform operator.
3. Calculate the spectral complex field of the d-scan trace, $\tilde{A}_{\mathrm{SHG}}(\omega, \ell)$, using equation 3.2;

4. Generate a new trace, $\tilde{A}'_{\mathrm{SHG}}(\omega,\ell)$, by combining the phase from the calculated trace, $\mathrm{Arg}\{\tilde{A}_{\mathrm{SHG}}(\omega,\ell)\}$, with the amplitude from the measured trace, $\sqrt{S_{\mathrm{SHG}}(\omega,\ell)}$;

5. Convert the new trace into the time domain by Fourier transform, yielding $\tilde{U}'_{\mathrm{SHG}}(t,\ell)$;

6. Calculate a new temporal field of the fundamental pulse as a function of glass insertion, $\tilde{U}'(t,\ell)$. To do so, we first multiply the complex conjugation of $\tilde{U}(t,\ell)$ with $\tilde{U}'_{\mathrm{SHG}}(t,\ell)$, from which the amplitude and the phase is equal to the cube root of the modulus of this product and the phase of this product respectively, i.e., $\tilde{U}'(t,\ell) = \sqrt[3]{|\tilde{U}'_{\mathrm{SHG}}(t,\ell)\tilde{U}^{*}(t,\ell)|}\exp(i\mathrm{Arg}\{\tilde{U}'_{\mathrm{SHG}}(t,\ell)\tilde{U}^{*}(t,\ell)\})$;

7. Convert $\tilde{U}'(t,\ell)$ of the fundamental pulse back to the spectral domain, yielding $\tilde{A}'(\omega,\ell)$;

8. Generate a new complex fundamental field by removing the spectral phase induced by glass insertions and following by averaging, i.e., $\tilde{A}''(\omega) = \mathrm{Avg}\{\tilde{A}'(\omega,\ell)\exp(-i\phi(\omega,\ell))\}$;

9. Repeat from step 2 by using the new field until the root-mean-square (RMS) error between the calculated trace and measured trace is below a certain target value.

For an uncalibrated, clipped, or noisy trace, a fundamental spectrum is required, which is applied to each iteration by replacing the envelope of the generated fundamental spectrum with the measured one in step 8. This method is computationally efficient for pulse retrieval and easy to implement. However, it is not as robust as the standard method, i.e., more sensitive to noise, as demonstrated in **Paper IV**.

Single Shot D-scan

In **Paper V**, we developed a single-shot version of the d-scan setup, motivated by measuring the pulse duration of ultrashort pulses from a hollow capillary, as well as ultrashort pulses generated at a low repetition rate (10 Hz). The single-shot capability is not necessary when the laser system is considerably stable and the measurements are reproducible. However, for many lasers, such as low-repetition rate lasers or unstable lasers, the scanning version can be either impractical or generate meaningless results. Furthermore, the single-shot pulse characterization method is convenient for inline optimization and monitoring. For a single-shot implementation of d-scan, the main challenge is achieving the dispersion variation with only a single pulse. In the previous work by Fabris at el. [43], a prism was used, with which the dispersion modulation was encoded spatially. In our work, presented in **Paper V**, a more compact version of the single-shot d-scan setup is presented, implemented and evaluated. This setup requires lower laser power and has a better signal-to-noise

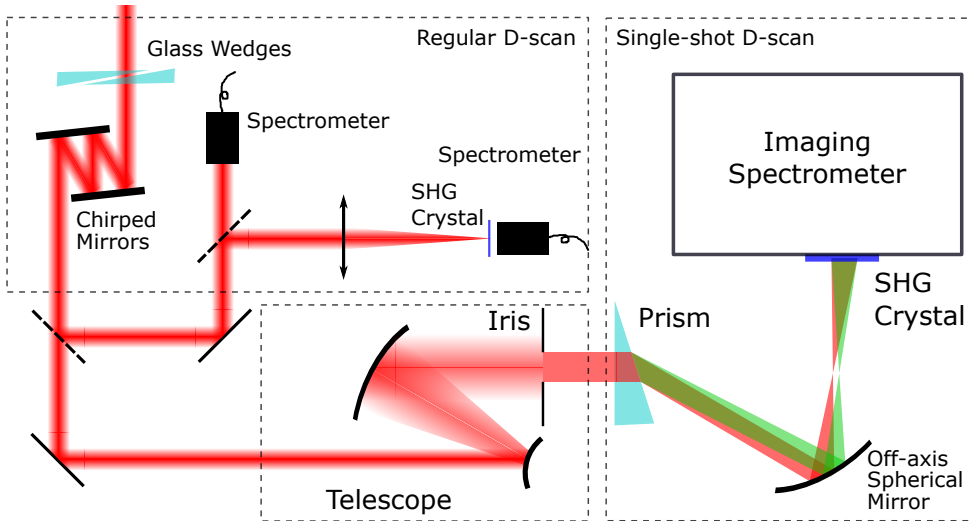

Figure 3.3: Setup for testing the single-shot d-scan setup.

ratio (SNR). A patent application for this single-shot d-scan implementation was filed in collaboration with the spin-off company SPHERE Ultrafast Photonics.

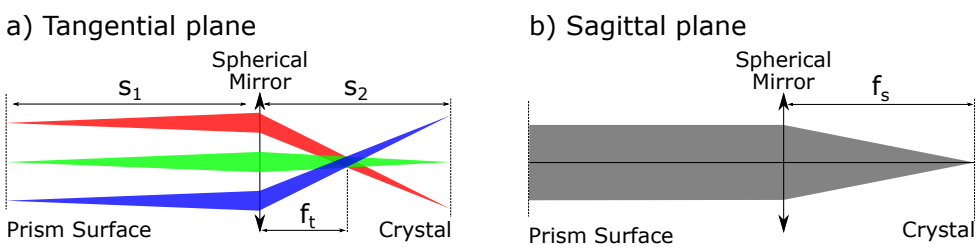

Figure 3.4: Principle of the beam path for the off-axis spherical mirror in the (a) tangential plane and (b) sagittal plane.

Our setup contains two main parts: a setup to generate a beam with a varying dispersion in one dimension and an imaging spectrometer. A prism is used to disperse the pulse spatially, so that different parts of the beam pass through different glass thicknesses, encoding a spatially varying amount of dispersion across the beam. By imaging the surface of the prism to the SHG crystal, the second harmonic is generated as a function of glass insertion over the crystal dimension. The second harmonic signal is subsequently analyzed by an imaging spectrometer. In our approach, as shown in figure 3.3, we use a spherical mirror off-axis, which has different effective focal lengths in the tangential and sagittal planes. In the tangential plane, the end surface of the prism is imaged to the SHG crystal, while in the sagittal plane, the parallel beam is focused into the crystal (figure 3.4). The SHG crystal

was mounted at the position of the entrance slit of the imaging spectrometer, thus avoiding the need for an additional imaging system. In contrast to the design in reference [43], our setup is very compact and provides a good SNR for laser systems with limited power and pulse energy.

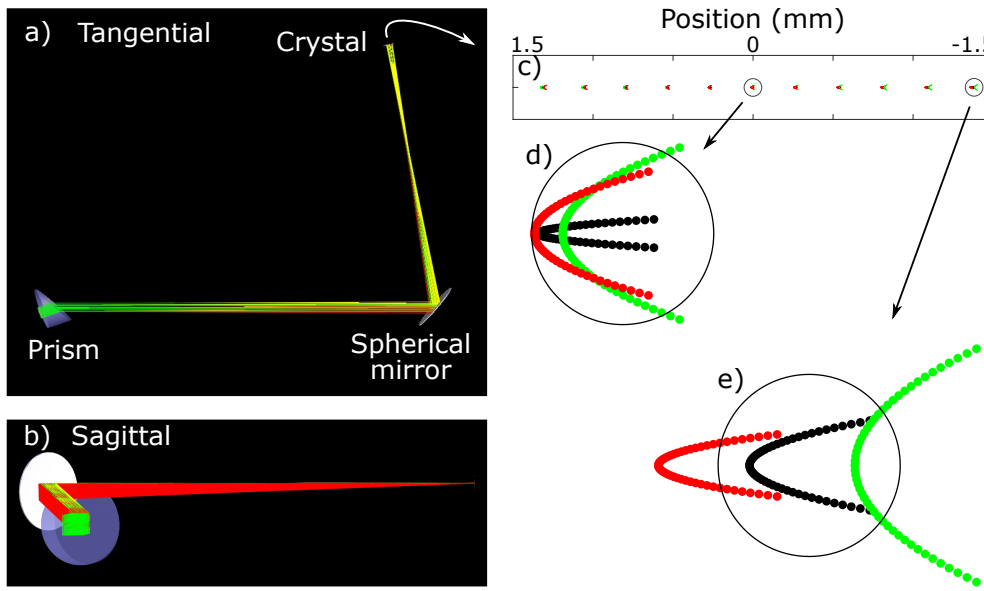

Figure 3.5: Ray tracing simulation results for the spherical mirror used at 40° in (a) the tangential plane and (b) the sagittal planes. The imaging quality is evaluated in (c), showing that the beam is focused in the sagittal plane (vertical direction) and imaged in the tangential plane. The magnified spots at the (d) center and the edge of the beam (e) are compared to the first minimum of an Airy disk focused by a 5 mm top-hat beam at 800 nm. The three colors indicate three different spectral components: red for 1200 nm, black for 800 nm and green for 600 nm.

A schematic of the off-axis spherical mirror imaging setup is shown in figure 3.4. In the tangential (a) and the sagittal (b) plane, the focal lengths are given by

$$f_\mathrm{t} = f_0 \cos\theta \tag{3.3a}$$

$$f_\mathrm{s} = \frac{f_0}{\cos\theta} \tag{3.3b}$$

where θ is the incident angle on the spherical mirror and $f_0 = R/2$ is the paraxial focal length for a spherical mirror with a radius of curvature of R. To focus in the sagittal plane, the distance s_2 from the spherical mirror to the crystal has to be equal to f_s. In the tangential plane, the prism is imaged to the crystal. The distance s_1 from the spherical mirror to the prism can be calculated using the imaging equation

$$\frac{1}{s_1} + \frac{1}{f_\mathrm{s}} = \frac{1}{f_\mathrm{t}}. \tag{3.4}$$

Hence, s_1 and s_2 are given by

$$s_1 = \frac{f_0 \cos\theta}{\sin^2\theta} \tag{3.5a}$$

$$s_2 = \frac{f_0}{\cos\theta}. \tag{3.5b}$$

The simplest solution is to choose $\theta = \pi/4$ or 45°, resulting in a one-to-one imaging condition. The actual angle used in our setup was 40°, which slightly demagnifies the image for a larger range of glass insertion. This design is validated by raytracing simulations using the FRED program, which are presented in figure 3.5. In figure 3.5(a) (tangential plane) and (b) (sagittal plane), a parallel beam containing 600 nm (blue), 800 nm (green) and 1200 nm (red) passes through a BK7 glass prism and is subsequently dispersed. The spherical mirror, with $f_0 = 50\,\mathrm{mm}$, images and focuses the beam into the crystal in the tangential and the sagittal planes respectively. The image spots at the plane of the crystal are shown in figure 3.5(c). To evaluate image quality, the spots at the center and the edge are compared with an ideal beam size, which is calculated by the first minimum of the Array disk for a top-hat beam, shown in figure 3.5(d) and (e), respectively. In this system, coma is considered to be the dominating aberration, due to the asymmetric use of the spherical mirror.

The imaging spectrometer used in this experiment is a modified Czerny-Turner imaging spectrometer [44–46]. This type of imaging spectrometer uses standard spherical mirrors and a grating, with special angles of incidence to minimize aberrations resulting from astigmatism. Since there are no transmission components, this design is also suitable for a broadband spectral range. The simulation of the imaging spectrometer is presented in figure 3.6. Three different colors that cover the spectral range of the SHG signal are analyzed in the simulation and indicated as red (460 nm), green (350 nm) and blue (260 nm) in figure 3.6(a). Figure 3.6(b) shows the direct image for different wavelengthes at the detector. As expected from the Czerny-Turner design, the spot in the middle of the field for 350 nm (figure 3.6(d)) is almost confined within the circle of the Array disk, i.e., this spot is almost diffraction-limited. For the two spots at the corner, as presented in figure 3.6(c) and (e), the imaging quality is worse due to possible astigmatism, coma and curvature of the image field. Even though the imaging condition is not ideal, the spot size for the worst spot is still less than the effective pixel size (80 µm×80 µm). This means that the imaging quality of this imaging spectrometer is still well-suited for recording single-shot d-scan traces.

This single-shot d-scan setup was tested with a 1 kHz repetition rate, titanium-doped-sapphire CPA laser system, behind a hollow capillary post-compression setup, similar to the one described in reference [47]. After compression with chirped mirrors, the beam size is magnified by a factor of 6 using a telescope, containing a concave and a convex mirror, so that the beam, after passing through an 8×5 mm rectangle aperture, can be considered

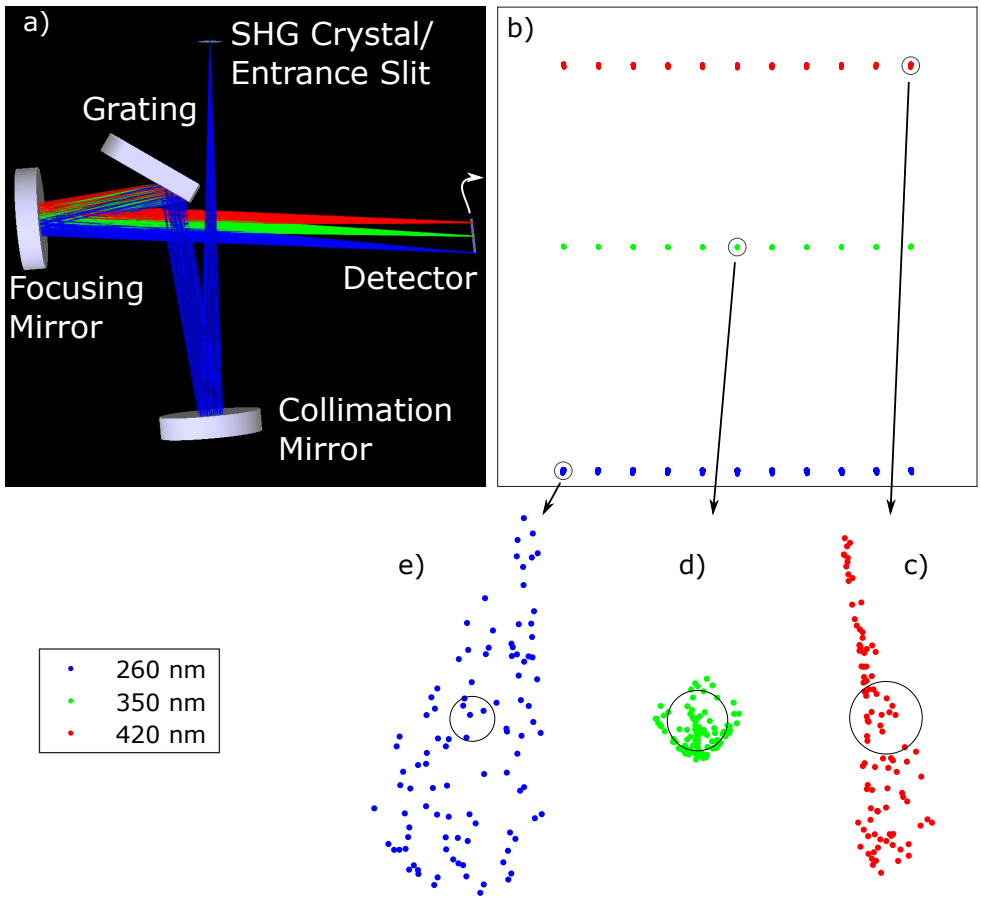

Figure 3.6: FRED simulation results for the imaging spectrometer: (a) schematic, (b) image on the detector, (c) magnified focal spot for 420 nm at the corner, (d) magnified focal spot for 350 nm in the middle of the field and (e) magnified focal spot for 260 nm at the opposite corner.

sufficiently homogeneous. A scanning d-scan was implemented for comparison purposes (figure 3.3). Figure 3.7 presents the measurement results. In (a), the standard d-scan trace is compared to the signal from the single-shot setup with (b) an average (25 shots) and (c) a true single-shot signal. These three traces agree well with each other. However, the signal around 260 nm is missing in the single-shot traces, due to the limited spectral range of the imaging spectrometer. The trace (d–f) are retrieved from the measured traces (a-c) respectively. The retrieved phase, blue for the standard scanning setup, red for the averaged single-shot measurement and green for the true single-shot measurement, as well as the temporal structures, are compared between the three measurements in (g) and (h) respectively. The spectral phases and the reconstructed temporal structures are very similar to each other, underlining the power of our single-shot d-scan implementation, even for the case

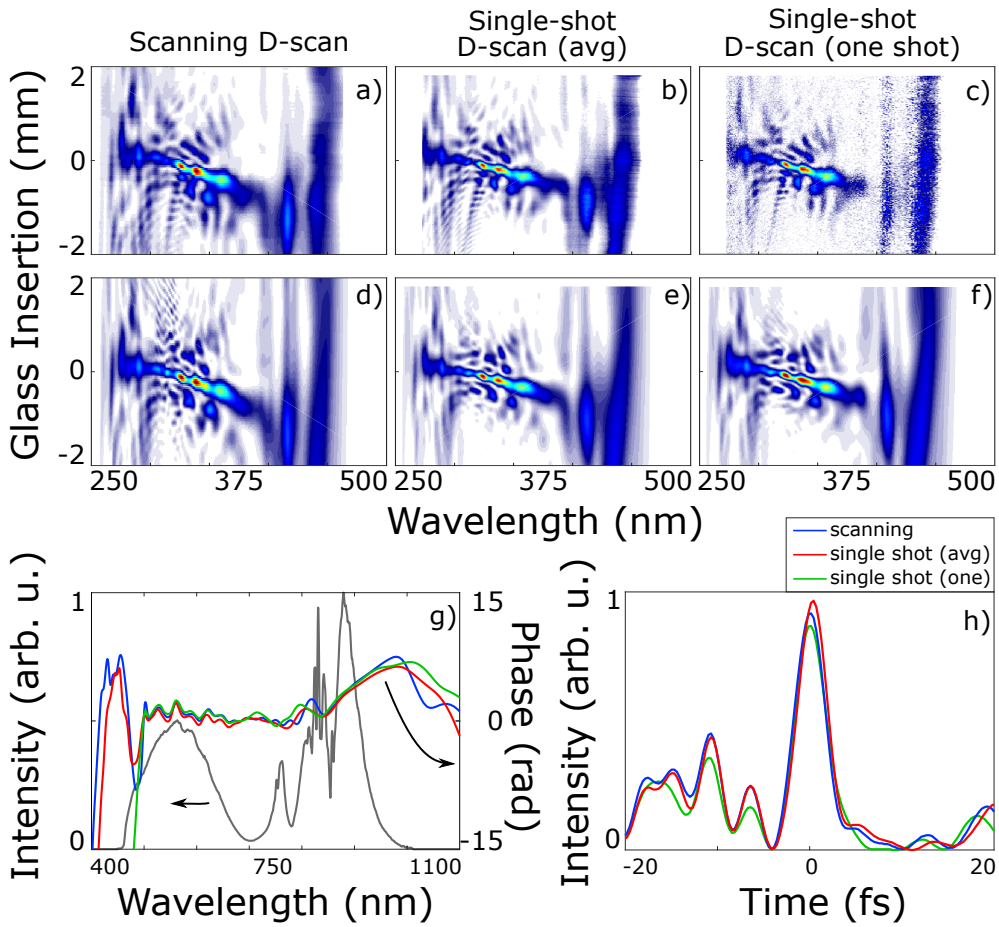

Figure 3.7: Comparison between the measurements and retrievals of (a,d) conventional d-scan, (b,e) averaged single-shot d-scan (over 25 shots) and (c,f) true one shot d-scan. The retrieved d-scan phases from the three measurements are compared in (g) and the retrieved temporal structures of the three measurements are compared in (h). The scanning d-scan, averaged single-shot d-scan and one-shot single-shot d-scan are indicated by blue, red and green respectively.

of a true single-shot measurement.

2 Spatio-temporal Coupling

A laser pulse is often described as a product of a spatial profile and a temporal profile that are independent from each other. This approximation is valid and works well for long pulses with a narrow spectrum ("monochromatic"). However, for ultrashort pulses with a broadband spectrum, the beam properties of each frequency component, such as wavefront

and beam shape, may have clear differences, so that this approximation is invalid. These differences may lead to complicated spatio-temporally coupled pulses. Part of this thesis work has been to develop a method to measure spatio-temporal couplings, motivated by characterizing the OPCPA laser system, as mentioned in chapter 2 and in **Paper I**. For OPCPAs with noncollinear parametric amplification stages, a tool to analyze spatio-temporal couplings is extremely important [48].

To determine the spatio-temporal couplings of a laser pulse, complete information of the pulse in space and time is necessary. We first introduce a mathematical description of spatio-temporal coupling within the framework of the Helmholtz equation [21, 22], where the beam propagates in the z-direction. In a given z position and at a given polarization, the complex amplitude of an ultrashort pulse can be written as:

$$A(x, y, \omega) \exp(i\Phi(x, y, \omega)), \tag{3.6}$$

where $A(x, y, \omega)$ and $\Phi(x, y, \omega)$ are the field amplitude and phase at a given point in space (x, y) and frequency ω respectively.

The laser beam is traditionally characterized by a camera (beam profiler), a spectrometer and some pulse duration measurement technique. With these instruments, the short pulse is described by the beam profile, the spectrum and the spectral phase:

$$A_0(x, y)s(\omega) \exp(i\Phi_0(\omega)), \tag{3.7}$$

where $A_0(x, y)$ is an averaged beam profile, $s(\omega)$ is the spectral amplitude, and $\Phi_0(\omega)$ is the spectral phase. An alternative method of measuring the beam profile is to use a fiber spectrometer and scan the fiber tip over the beam. Using this technique, the beam with a spatially inhomogeneous spectrum can be characterized, which yields:

$$A(x, y, \omega) \exp(i\Phi_0(\omega)), \tag{3.8}$$

This method does not give information on the spatial dependence of the spectral phase. Obviously, none of the methods mentioned above can provide complete information about the pulse. Hence, new techniques are needed to obtain a complete characterization of a short pulse.

2.1 Simple Examples: Spatial Chirp and Angular Chirp

In this section, two "typical" spatio-temporal couplings, i.e., spatial chirp and angular chirp, are briefly discussed. These two couplings, which are very simple and intuitive to understand, are illustrated in figure 3.8. The beam profile for each frequency component and the total spectrum are assumed to have a Gaussian shape. In figure 3.8(a)-(d), an ideal

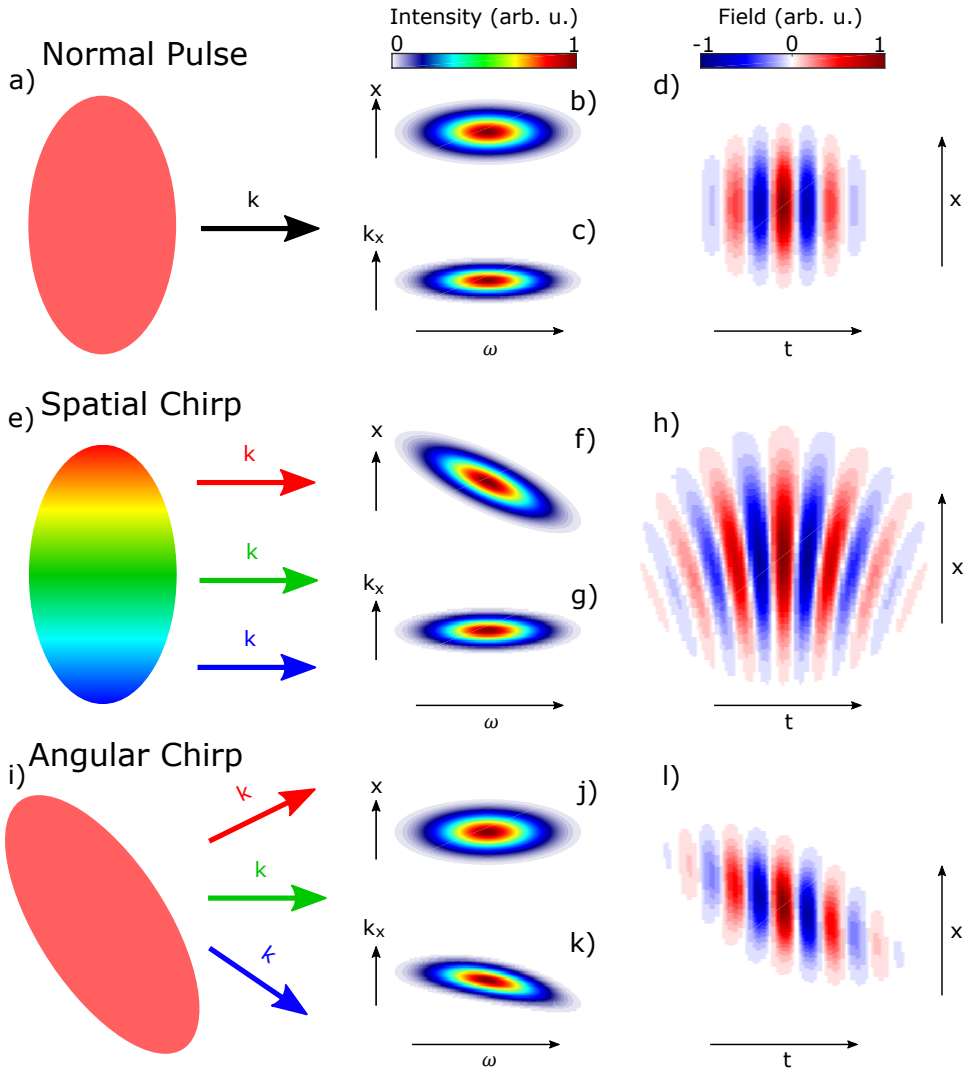

Figure 3.8: Examples of spatio-temporal couplings: (a-d) an ideal Gaussian pulse with no coupling, (e-h) a pulse with spatial chirp and (i-l) a pulse with angular chirp. In (x, ω) representation (b,f,j), the normal pulse and angular chirped pulse are the same, while in (f), the (x, ω) spectrogram is tilted. In (k_x, ω) space (c,g,k), the frequency components of normal and spatially chirped pulse propagate in the same direction, while for the angular chirped pulse, they do not. (d,h,l), the (x, t) representations show corresponding electric field.

Gaussian pulse without spatio-temporal coupling is presented for comparison purposes. In practice, spatio-temporal couplings are often a combination of these two simple cases. A more complicated example, a vortex pulse, is studied in **Paper VII** and section 2.3.

Linear spatial chirp, as shown in figure 3.8(e), refers to a situation where the frequency

components of a pulse vary over one direction, which is the x-direction in this case. Figure 3.8(f) shows the (x, ω) representation of the pulse, illustrating how the spectrum changes in space. Figure 3.8(g) presents the (k_x, ω) representation, indicating that all frequency components propagate into the same direction. By Fourier transforming the field over frequency, figure 3.8(h) is obtained and shows the field of the pulse. Different frequency components are found at different x positions and the wavefront of the pulse is rotating over the pulse. When using this pulse to generate high-order harmonics, the attosecond pulses from each half-cycle are emitted into different directions, which is known as the "lighthouse effect" [49].

For a pulse with angular chirp, different frequency components propagate in different directions, while the spectrum is spatially homogeneous (figure 3.8(i)). In contrast to spatial chirp, the angular chirp is observed in the (k_x, ω) representation (figure 3.8(k)). Figure 3.8(l) shows that the pulse generally propagates forward, but the pulse appears earlier or later on the side relative to the central part. This effect is called "pulse front tilt". This phenomenon is attributed to the additional group delay from the varying wavefront of each frequency component.

2.2 Measurement Method: Spatial-Resolved Fourier Transform Interferometry

In **Paper VI**, we present a spatially-resolved pulse characterization technique based on Fourier transform spectrometry. This method was independently developed in Lund and at CEA Saclay [40]. It measures the spectral amplitude in the (x, y) plane, as well as the phase difference with respect to a well-defined reference wave, which can be characterized with the d-scan technique. The measurement determines:

$$A(x, y, \omega) \exp(i(\Phi_r(x, y, \omega) + \Phi_0(\omega))) \tag{3.9}$$

with

$$\Phi_r(0, 0, \omega) = 0, \tag{3.10}$$

where $A(x, y, \omega)$ and $\Phi_r(x, y, \omega)$ are obtained with the spatially-resolved Fourier transform spectrometer, and $\Phi_0(\omega)$ is retrieved from a conventional ultrashort pulse characterization technique.

The basic idea of this technique is to combine holography and Fourier transform spectroscopy. The reference pulse spatially interferes with the unknown pulse and the interference pattern contains the phase difference between the two beams, like a hologram. Spectral information is obtained by varying the time delay between the reference pulse and the unknown pulse, while recording the interference pattern with a CCD camera. The inter-

ference pattern can be mathematically described as:

$$I(x,y,\tau) = \int_{-\infty}^{+\infty} \mathrm{d}t \left| \tilde{U}(x,y,t) + \tilde{U}_{\mathrm{ref}}(x,y,t+\tau) \right|^2, \tag{3.11}$$

where $I(x,y,\tau)$ is the measured intensity in the (x,y) plane for a given time delay τ, and $\tilde{U}$ and $\tilde{U}_{\mathrm{ref}}$ are the complex fields for the unknown and reference pulse respectively. Equation 3.11 can be written as:

$$\begin{aligned} I(x,y,\tau) = \int_{-\infty}^{+\infty} \mathrm{d}t [& \tilde{U}(x,y,t)\tilde{U}^*(x,y,t) && \text{(3.12a)} \\ & + \tilde{U}_{\mathrm{ref}}(x,y,t+\tau)\tilde{U}^*_{\mathrm{ref}}(x,y,t+\tau) && \text{(3.12b)} \\ & + \tilde{U}^*(x,y,t)\tilde{U}_{\mathrm{ref}}(x,y,t+\tau) && \text{(3.12c)} \\ & + \tilde{U}(x,y,t)\tilde{U}^*_{\mathrm{ref}}(x,y,t+\tau)]. && \text{(3.12d)} \end{aligned}$$

The first two terms (equations 3.12(a) and (b)) give a constant intensity, which are the beam profile information of the unknown and reference beam, noted as $I_0(x,y)$ and $I_{\mathrm{ref}}(x,y)$, respectively. By Fourier transforming the signal $I(x,y,\tau)$, equation 3.12 yields:

$$\begin{aligned} \tilde{S}(x,y,\omega) &= \int_{-\infty}^{+\infty} \mathrm{d}\tau \mathrm{e}^{-i\tau\omega} I(x,y,\tau) && \text{(3.13a)} \\ &= \delta(\omega)\left(I_0(x,y) + I_{\mathrm{ref}}(x,y)\right) \\ &\quad + \int_{-\infty}^{+\infty} \mathrm{d}t e^{it\omega} \left[\tilde{U}^*(x,y,t)\tilde{A}_{\mathrm{ref}}(x,y,\omega) + \tilde{U}(x,y,t)\tilde{A}^*_{\mathrm{ref}}(x,y,-\omega)\right] && \text{(3.13b)} \\ &= \delta(\omega)\left(I_0(x,y) + I_{\mathrm{ref}}(x,y)\right) + \tilde{A}^*(x,y,\omega)\tilde{A}_{\mathrm{ref}}(x,y,\omega) + \tilde{A}(x,y,-\omega)\tilde{A}^*_{\mathrm{ref}}(x,y,-\omega), && \text{(3.13c)} \end{aligned}$$

where $\delta(\omega)$ is the Dirac delta function and $\tilde{A}(x,y,\omega)$ and $\tilde{A}_{\mathrm{ref}}(x,y,\omega)$ are the complex spectral amplitude for the unknown and reference pulse. Thus, by Fourier transforming the signal $I(x,y,\tau)$, we can extract three different terms in equation 3.13c: the first term is the total beam profile which does not vary with time delay; the second term is the field product between the unknown and reference pulse, where the complex conjugate implies that the measured phase is the phase difference between the two beams, for a positive frequency; and the third term is the complex conjugation to the previous term for a negative frequency. By selecting either the second or the third term, we can determine the spectral amplitude and phase information at each point in space if the reference pulse is known. It is not convenient to use an auxiliary laser for reference, and our approach to solve this problem is self-referencing. We split part of the incoming beam and focus it to a pinhole for spatial filtering and expand the beam as much as possible at the detector. The reference pulse generally overfills the detector and is assumed to be homogeneous over the size of the

detector, both in amplitude and phase. Furthermore, it is assumed that the reference pulse is a homogeneously expanded copy of the pulse at the center. Thus,

$$\tilde{A}_{\mathrm{ref}}(x, y, \omega) \approx \tilde{A}(0, 0, \omega). \tag{3.14}$$

With this approximation, equation 3.13c can be rewritten as

$$\tilde{S}(x, y, \omega) = \delta(\omega)\,(I_0(x, y) + I_0(0, 0)) + \tilde{A}^*(x, y, \omega)\tilde{A}(0, 0, \omega) + \tilde{A}(x, y, -\omega)\tilde{A}^*(0, 0, -\omega). \tag{3.15}$$

For positive ω, equation 3.15 is reduced to

$$\tilde{S}(x, y, \omega) = \tilde{A}^*(x, y, \omega)\tilde{A}(0, 0, \omega) = A(x, y, \omega)A(0, 0, \omega)\exp(-i\Phi_r(x, y, \omega)) \tag{3.16}$$

where $A(x, y, \omega)$ is the spectral amplitude over (x, y) plane. At the center of the field $(0, 0)$, $A(0, 0, \omega) = \sqrt{|\tilde{S}(0, 0, \omega)|}$. Therefore, we can retrieve the position dependent spectral amplitude $A(x, y, \omega)$ and the relative phase $\Phi_r(x, y, \omega)$ by removing $A(0, 0, \omega)$ from $\tilde{S}(0, 0, \omega)$.

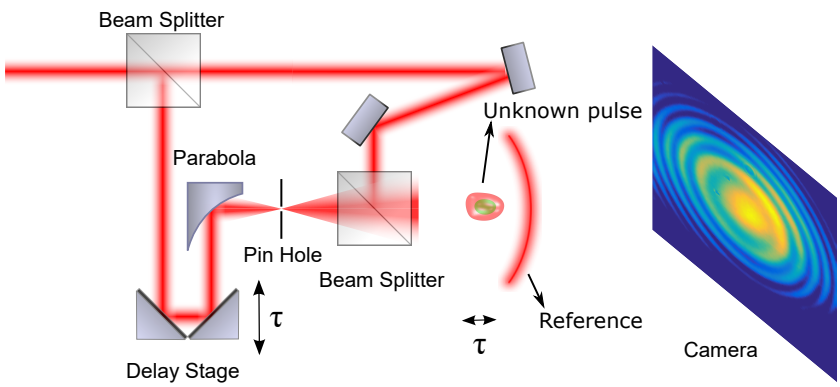

Figure 3.9: Principle of the spatially resolved Fourier Transform spectrometer.

Experimentally, as shown in figure 3.9, this setup is implemented as a modified Mach – Zehnder interferometer. The incoming beam is first split by a 90:10 beamsplitter. The arm with higher power is subsequently delayed with a piezo-driven delay stage and focused by an off-axis parabola into a pinhole with 20 µm diameter. The spatially filtered beam subsequently passes through another 50:50 beamsplitter and illuminates the camera, with a spherical wavefront. In the other arm of the interferometer, the beam goes through a delay line to match acquired in the other arm and is recombined with the reference beam using a beamsplitter. The unknown and reference beams interfere on the camera chip as shown in the figure 3.9. The interferometer is constructed in a compact way on a 25 cm × 25 cm breadboard, for good stability.

There are a few practical issues when implementing this technology. The first one is the numerical aperture. The numerical aperture in this setup is limited by the transverse resolution of the camera. In the experiment, the typical resolution is 160×128 pixels (after binning), corresponding to 26.6 lines/mm sampling rate or 13.3 lines/mm of maximum spatial frequency. Binning was performed to increase the effective dynamic range and keep the size of a data set manageable. The spatial resolution limits the numerical aperture to NA $\approx$ 0.01, which means that the camera has to be far away from the focus of the spatial filter, so that the spherical wavefront from the reference beam is not the limiting factor of detection. Otherwise, the circular fringes originating from the spherically curved wavefront of the reference pulses could not be resolved with efficient resolution. The second issue is the camera. The dynamic range limits the signal-to-noise ratio of the reconstructed spectrum. The nonlinear response to intensity of the camera can also reduce the effective dynamic range. The last issue is data size. For a typical scan, the data size is 160 × 128 × 2048, corresponding to 640 megabits. This limitation is even more critical for data analysis when the data format is converted to floating point numbers (1.25 gigabits for single precision).

2.3 Characterization of Optical Vortex Pulses

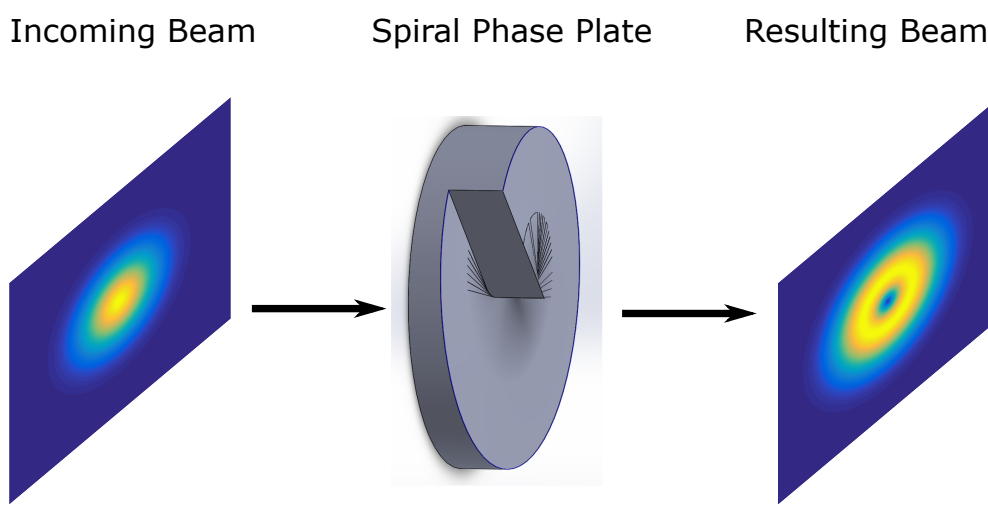

Figure 3.10: Spiral phase plate. This plate can convert a fundamental Gaussian pulse to a higher-order Laguerre-Gaussian beam.

An optical vortex is a laser beam containing a phase singularity around which the phase spatially spins. This spinning is quantized due to the continuity of the phase. An optical vortex carries spatial angular orbital momenta. This property is interesting e.g. in quantum information [50] and for optical tweezers [51]. When using an optical vortex pulse to generate high-order harmonics, as a number of early works have shown [36, 52], orbital angular

momentum of the fundamental pulse can be transferred to high-order harmonics, thus transferring quantum control from the visible to the XUV and X-ray range. In the space and time domain, an optic vortex has a spiral waveform, with spatio-temporal coupling. This motivated us to text our spatially resolved Fourier transform spectrometer by characterizing an optical vortex pulse (**Paper VII**).

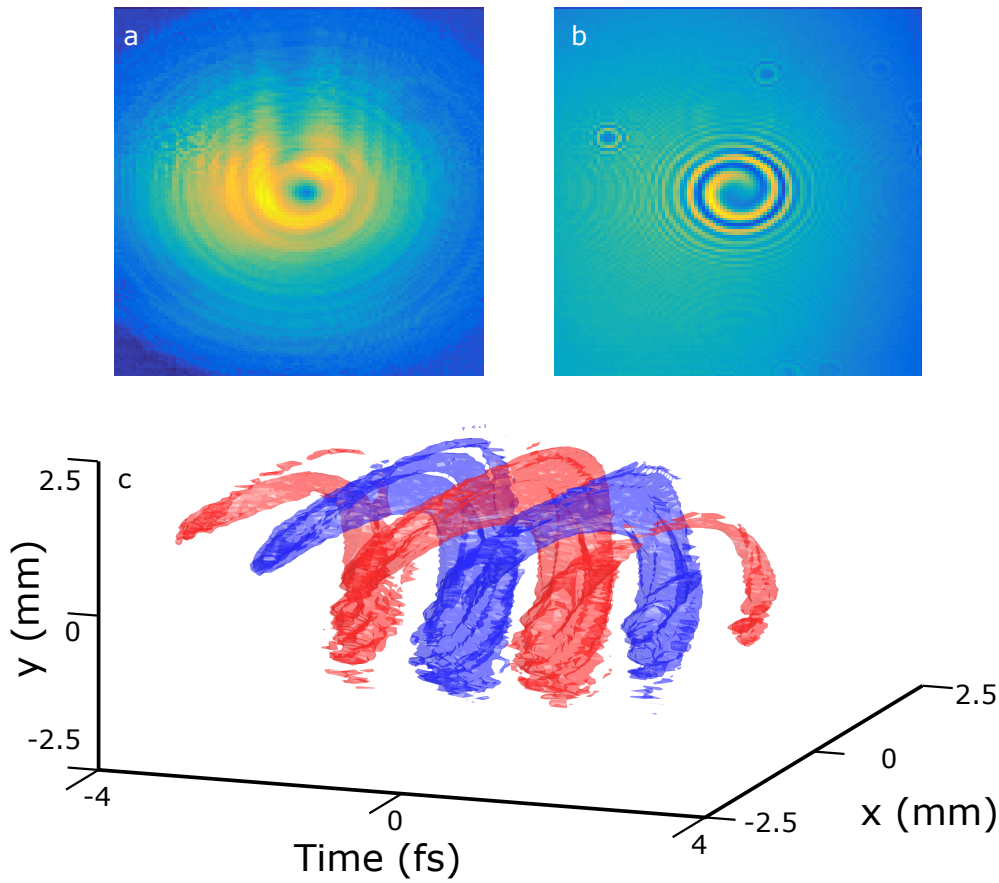

Figure 3.11: Spatial temporal characterization of the vortex pulse: (a) averaged beam profile, (b) interference pattern on the detector at zero time delay and (c) the reconstructed pulse field, where red and blue isosurfaces indicate the positive and negative fields.

The optical vortex pulse is generated by a spiral phase plate [53, 54]. The phase plate, schematized in figure 3.10, introduces different delays around the center of the beam. This phase difference leads to spatial angular orbital momentum to the beam, i.e., inducing higher-order Laguerre-Gaussian modes [22]. In our experiment, we insert the spiral phase plate (RPC Photonics) into one arm of the spatially resolved Fourier transform spectrometer to generate an optical vortex pulse (the "unknown pulse"). Figure 3.11 shows the main results of this experiment. Figure 3.11(a) shows the average beam profile as a "donut" shape as ex-

pected. Figure 3.11(b) shows one of the frames with clear fringes. Compared to the typical concentric fringes (mostly due to the spherical wavefront of the reference beam) shown in figure 3.9, the fringes here have a spiral shape, indicating that the phase varies angularly. Finally, figure 3.11(c) shows the reconstructed field with a spiral structure, where the negative and positive fields are indicated by red and blue isosurfaces respectively, which is very similar to what theory would predict.

Chapter 4

High-order Harmonic Generation

High-order harmonic generation is an important part of this thesis. **Paper I** presents a HHG source driven by the 200 kHz OPCPA laser system where high-order harmonics were generated by different noble gases and the conversion efficiency was optimized by designing and implementing a high-pressure gas jet. **Papers II** and **III** present HHG studies as a function of fundamental CEP and chirp. The results were interpreted by a multiple-pulse interference model (**Paper III**).

1 Single Atom Response: Three-step Model

HHG is a highly nonlinear response of an atom (or molecule) to a strong linearly-polarized electromagnetic field. It can be described theoretically by numerically solving the time-dependent Schrödinger equation (TDSE). However, solving the TDSE is a computationally expensive task [55]. And the physical process is often hidden behind the numerical calculations. Thus, a model with a clear physical picture is needed. In the perturbative regime, the strength of the high-order harmonics is expected to decrease exponentially as the order increases. However, this theory cannot yield a good explanation of the plateau harmonics that have similar intensity over a broad spectrum range. Recollision theory, introduced by the pioneers of this field in the early 1990s [56–58], explains the HHG as a three-step process: first, an electron is ionized from the atom (multiphoton or tunneling ionization); second, the free electron is accelerated in the laser field and gains kinetic energy; third, the electron recombines with the parent ion and emits a photon with total energy equal to the sum of the kinetic energy (E_k) and ionization potential (I_p).

The simplest way of implementing the three-step model is to describe the electron, once it is ionized, as a classical particle and to solve the Newtonian motion equation in one

dimension:

$$\frac{\mathrm{d}^2x}{\mathrm{d}t^2} = -\frac{eE(t)}{m_\mathrm{e}}, \tag{4.1}$$

where x is the position of the electron relative to the parent ion, e and m_e are the charge and mass of electron respectively and $E(t)$ is the time-dependent electric field. For further simplification, we neglect the Coulomb potential from the ion relative the strong laser field and assume that the size of the ion is small so that the electron recombines to the ion when $x = 0$. Hence, for a sinusoidal driving wave, the velocity v and position x of the electron are,

$$v(t) = \frac{eE_0}{m_\mathrm{e}\omega_0}\left(\cos(\omega_0 t) - \cos(\omega_0 t_\mathrm{i})\right), \tag{4.2a}$$

$$x(t) = \frac{eE_0}{m_\mathrm{e}\omega_0^2}\left(\sin(\omega_0 t) - \sin(\omega_0 t_\mathrm{i}) - (\omega_0 t - \omega_0 t_\mathrm{i})\cos(\omega_0 t_\mathrm{i})\right), \tag{4.2b}$$

where E_0 and ω_0 are the amplitude and frequency of the driving field respectively and t_i is the time at which the electron is ionized. At time t_r, the electron meets the parent ion and recombines, i.e., $x(t_\mathrm{r}) = 0$. Hence, t_r is given by solving

$$0 = \sin(\omega_0 t_\mathrm{r}) - \sin(\omega_0 t_\mathrm{i}) - (\omega_0 t_\mathrm{r} - \omega_0 t_\mathrm{i})\cos(\omega_0 t_\mathrm{i}). \tag{4.3}$$

This equation is a transcendental equation, which is very hard to solve analytically.

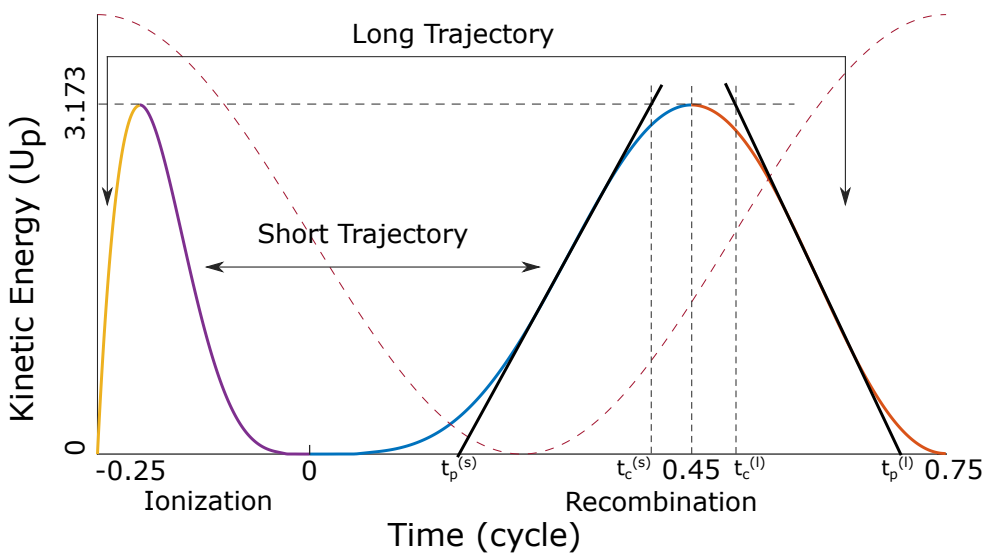

Figure 4.1: Kinetic energy as a function of the ionization and recombination time. The yellow and red curves indicate the ionization and recombination times for long trajectories and the purple and blue curves present the ionization and recombination times for short trajectories. The two black curves are the tangents at the midpoint of E_k. These two curves cross zero at $t_\mathrm{p}^{(\mathrm{s})}$ and $t_\mathrm{p}^{(\mathrm{l})}$ respectively, reaching the cutoff at $t_\mathrm{c}^{(\mathrm{s})}$ and $t_\mathrm{c}^{(\mathrm{l})}$ respectively.

The kinetic energy of the electron is given as

$$E_{\mathrm{k}} = \frac{1}{2} m_{\mathrm{e}} v^2 = 2U_{\mathrm{p}} \left[\cos(\omega_0 t_{\mathrm{r}}) - \cos(\omega_0 t_{\mathrm{i}})\right]^2 , \tag{4.4}$$

where $U_{\mathrm{p}} = e^2 E_0^2 / 4 m_{\mathrm{e}} \omega_0^2$, which is the ponderomotive energy, i.e., the cycle-averaged energy of a free electron in the laser field. Figure 4.1 shows kinetic energy E_{k} as a function of t_{i} ($[-0.25, 0]$)and t_{r} ($[0, 0.75]$). The maximum kinetic energy E_{k} is equal to $3.173 U_{\mathrm{p}}$ at about 0.45 cycles, which is known as the classical cutoff energy. For the spectral components generated before the cutoff, the trajectories are called short trajectories, while the others are long trajectories. In this figure, the yellow and red curve indicates the ionization and recombination times for the long trajectories, while the purple and blue curve represents the ionization and recombination times for the short trajectories. The two black curves are the tangents at the middle of the plateau for the short and long trajectories. These tangents cross at intersections $t_{\mathrm{p}}^{(\mathrm{s})}$ and $t_{\mathrm{p}}^{(\mathrm{l})}$ for the short and long trajectories respectively, when $E_{\mathrm{k}} = 0$. These tangents also reach the cutoff energy at time $t_{\mathrm{c}}^{(\mathrm{s})}$ and $t_{\mathrm{c}}^{(\mathrm{l})}$.

1.1 Intensity-dependent Dipole Phase

As shown in figure 4.1, the different frequency components are generated at different times, leading to a chirped attosecond pulse. This chirp is known as the "atto chirp". Strong Field Approximation (SFA) [59], which is a quantum mechanic derivation recovering many features of the semi-classical model, predicts the phase corresponding to this chirp. This phase is also known as the "dipole phase" of the attosecond pulses. The intensity dependence of the dipole phase has been studied for more than two decades, both experimentally and theoretically [60–63]. In this thesis, an analytical model is developed based on analyzing the classical trajectories [64], also presented in **Paper III**.

Figure 4.1 represents the energy-time link of the trajectories. The plotted curves maintain their shape when intensity is varied, reflecting the fact that equation 4.4 is proportional to the intensity, while the ionization and recombination time pair, t_{i} and t_{r}, is not (equation 4.3). The slopes of the tangent at the midpoint of the plateau increase linearly with intensity while the times, $t_{\mathrm{p}}^{(\mathrm{s})}$, $t_{\mathrm{p}}^{(\mathrm{l})}$, $t_{\mathrm{c}}^{(\mathrm{s})}$ and $t_{\mathrm{c}}^{(\mathrm{l})}$, are intensity-independent.

We assume that the recombination time t_{r} is also the time at which the corresponding frequency component of the XUV pulse appears. We neglect possible delays for the recombination and tunneling processes [65]. The group delay as a function of the XUV frequency Ω can be written as:

$$GD^{(\mathrm{s,l})}(\Omega) = t_{\mathrm{p}}^{(\mathrm{s,l})} + \frac{t_{\mathrm{c}}^{(\mathrm{s,l})} - t_{\mathrm{p}}^{(\mathrm{s,l})}}{\Omega_{\mathrm{c}} - \Omega_{\mathrm{p}}} (\Omega - \Omega_{\mathrm{p}}) \tag{4.5}$$

where Ω_c and Ω_p are equal to $(3.17U_p + I_p)/\hbar$ and $I_p/\hbar$, corresponding to the cutoff and ionization energy respectively.

The phase of the attosecond pulse is approximated by the integral of the group delay (equation 4.5), i.e.,

$$\phi^{(s,l)}(\Omega) = \mathcal{C}^{(s,l)} + t_p^{(s,l)}(\Omega - \Omega_p) + \frac{t_c^{(s,l)} - t_p^{(s,l)}}{2(\Omega_c - \Omega_p)}(\Omega - \Omega_p)^2 \tag{4.6}$$

where $\mathcal{C}^{(s,l)} = \phi^{(s,l)}(\Omega_p)$. Since $\hbar(\Omega_c - \Omega_p) = 3.17U_p \propto I$, equation 4.6 can be rewritten as,

$$\phi^{(s,l)}(\Omega) = \mathcal{C}^{(s,l)} + \beta^{(s,l)}(\Omega - \Omega_p) + \frac{\gamma^{(s,l)}}{I}(\Omega - \Omega_p)^2 \tag{4.7}$$

with

$$\beta^{(s,l)} = t_p^{(s,l)}; \tag{4.8a}$$

$$\gamma^{(s,l)} = \frac{(t_c^{(s,l)} - t_p^{(s,l)})\hbar m_e \omega_0^2 \varepsilon_0 c_0}{3.17e^2} \tag{4.8b}$$

$$\approx \frac{137(t_c^{(s,l)} - t_p^{(s,l)})m_e\omega_0^2}{3.17 \cdot 4\pi} \tag{4.8c}$$

where ε_0 and c_0 are the permittivity and speed of light in vacuum. In equation 4.8c, some of the physics constants are replaced by the fine structure constant, with $4\pi\hbar\varepsilon_0 c_0/e^2 \approx 137$.

Considering that there is only one cutoff trajectory, the phase for short and long trajectory, $\phi^{(s)}$ and $\phi^{(l)}$, should merge at the cutoff frequency (or at an effective cutoff frequency that is generally higher than that given by the semi-classical model [66]), yielding,

$$\phi^{(s)}(\Omega_c) = \phi^{(l)}(\Omega_c) \tag{4.9a}$$

$$\mathcal{C}^{(s)} + \beta^{(s)}(\Omega_c - \Omega_p) + \frac{\gamma^{(s)}}{I}(\Omega_c - \Omega_p)^2 = \mathcal{C}^{(l)} + \beta^{(l)}(\Omega_c - \Omega_p) + \frac{\gamma^{(l)}}{I}(\Omega_c - \Omega_p)^2 \tag{4.9b}$$

$$\mathcal{C}^{(s)} + \mathcal{F}\beta^{(s)}I + \mathcal{F}^2\gamma^{(s)}I = \mathcal{C}^{(l)} + \mathcal{F}\beta^{(l)}I + \mathcal{F}^2\gamma^{(l)}I, \tag{4.9c}$$

with a factor

$$\mathcal{F} = \frac{3.17e^2}{2\hbar m_e \omega_0^2 \varepsilon_0 c_0}. \tag{4.10}$$

Equation 4.9c indicates that the difference between the "constants" $\mathcal{C}^{(s)} - \mathcal{C}^{(l)}$ is proportional to the intensity I, since $\mathcal{F}$, $\beta^{(s,l)}$ and $\gamma^{(s,l)}$ are constant. However, $\mathcal{C}^{(s)}$ and $\mathcal{C}^{(l)}$ are still not determined. To keep an uniform formula, we rewrite $\mathcal{C}^{(s,l)}$ as $\alpha_0^{(s,l)}I$, and equation

4.7 becomes,

$$\phi^{(s,l)}(\Omega) = \alpha_0^{(s,l)} I + \beta^{(s,l)}(\Omega - \Omega_p) + \frac{\gamma^{(s,l)}}{I}(\Omega - \Omega_p)^2 \tag{4.11}$$

The value of $\beta^{(s,l)}$ and $\gamma^{(s,l)}$ can be directly determined by the values of $t_p^{(s,l)}$ and $t_c^{(s,l)}$, where $t_p^{(s)} = 0.1784$ cycle, $t_p^{(l)} = 0.6935$ cycle, $t_c^{(s)} = 0.4006$ cycle and $t_c^{(l)} = 0.5048$ cycle. Thus, for a laser field centered at 800 nm, $\beta^{(s,l)}$ and $\gamma^{(s,l)}$ are determined by equation 4.8a and 4.8c as,

$$\beta^{(s)} = 0.4758\,\text{fs}; \tag{4.12a}$$

$$\beta^{(l)} = 1.8496\,\text{fs}; \tag{4.12b}$$

$$\gamma^{(s)} = 1.030 \times 10^{12}\,\text{fs}^2\,\text{W}\,\text{cm}^{-2}; \tag{4.12c}$$

$$\gamma^{(l)} = -0.874 \times 10^{12}\,\text{fs}^2\,\text{W}\,\text{cm}^{-2}. \tag{4.12d}$$

The values of $\alpha_0^{(s,l)}$ are not straightforward to determine. For the long trajectory, the value of $\alpha_0^{(l)}$ can be determined by equation 4.9c when $\alpha_0^{(s)}$ is known. $\alpha_0^{(s)}$ is the intensity-dependent phase for the shortest trajectory, for which the time of propagation in the continuum is zero. The Strong Field Approximation (SFA) theory [59] predicts that $\alpha_0^{(s)}$ should be zero. However, in a recent study [66], $\alpha_0^{(s)}$ is found to have a small negative value, due to the influence of bound states below the ionization potential.

The form of the intensity dependent dipole phase is often written as αI in the literature [60, 61, 63]. This form was derived from the SFA theory, where α is a function of t_i and t_r, and $\alpha(t_i, t_r)$ is intensity independent. However, when α is written as a function of XUV frequency Ω, this form is not strictly valid.

2 Multiple Pulse Interference

The total HHG spectrum results from the interference of the attosecond pulses generated from each half-cycle of the driving laser field. In this thesis, we consider mainly the contribution of the short trajectories, as shown in **Paper III**. Thus, in the following sections, $\phi^{(s)}(\Omega)$ is replaced by $\phi(\Omega)$ for simplification of notification, and $\phi^{(s)}(\Omega)$ is approximated by equation 4.11 where $\alpha_0^{(s)}$ is equal to zero. The total spectral complex amplitude $\tilde{A}_{tot}(\Omega)$

is given by the sum of the complex amplitudes of each attosecond pulse:

$$\tilde{A}_{\mathrm{tot}}(\Omega) = \sum_{m=n}^{l} A_m(\Omega) \exp\left(i(t_m\Omega + m\pi + \phi_m(\Omega))\right), \tag{4.13}$$

where m is the index of the attosecond pulses, $A_m(\Omega)$ is the spectral amplitude of the mth attosecond pulse, t_m is the time at which the shortest trajectory is generated i.e., when the fundamental field crosses zero, the $m\pi$ term describes the sign-flip of $A_m(\Omega)$ for every consecutive half-cycle of the fundamental field and $\phi_m(\Omega)$ is the dipole phase of the mth attosecond pulse, which delays each frequency component with respect to t_m.

The spectral amplitude $A_m(\Omega)$ is determined by both the ionization and the recombination processes. The ionization rate, which is calculated by the Ammosov–Delone–Kraĭnov (ADK) approximation [67], yields the strength ($\int \mathrm{d}\Omega |A_m(\Omega)|^2$) of the attosecond pulses. The generated spectrum is initially set to be a super-Gaussian shape spectrum, and this spectrum is dressed by the recombination probability, proportional to the photoionization cross section [68]. The time t_m depends on the exact waveform of the fundamental pulse. Usually t_m can only be determined numerically due to the difficulty of calculating the waveform of an arbitrary pulse. For Gaussian pulses, the electric field is well-defined, so that an analytical solution of t_m can be used (see **Paper III**). The intensity-dependent dipole phase term, $\phi_m(\Omega)$, leads to an irregular attosecond pulse train. This is because different attosecond pulses experience different intensities, particularly when the fundamental pulse is short and the intensity varies rapidly over each half-cycle. This effect leads to complex harmonic spectra depending on the parameters of the fundamental pulses, such as CEP and chirp. The effect is further discussed in section 4.3 as well as **Paper III**.

3 Phase Matching

In the previous sections, we discussed the single atom response of HHG. For efficient HHG, a certain phase matching condition must be realized, such that the radiation from each emitter (atom) in the medium should add coherently. Phase matching for HHG is very similar to phase matching when using crystals, i.e., the phase velocity of XUV and the IR driving field must be equal. Often, several effects contribute to dephasing between the fundamental field and XUV radiation [69], described by the wave vector mismatch Δk,

$$\Delta k = \Delta k_{\mathrm{g}} + \Delta k_{\mathrm{d}} + \Delta k_{\mathrm{n}} + \Delta k_{\mathrm{p}}. \tag{4.14}$$

Here, Δk_{g} is the contribution from the focusing geometry, Δk_{d} is the mismatch due to the dipole phase, and Δk_{n} and Δk_{p} are due to dispersion from the neutral gas and free electrons generated during the generation process respectively. The geometry term, Δk_{g}, is due to

phase delay over the waist of the focus, known as the Gouy phase [22]. On the optical axis, Δk_{g} is given $\mathrm{d}\Phi(z)/\mathrm{d}z$ where $\Phi(z)$ is the Gouy phase. The intensity-dependent dipole phase also plays an important role due to intensity variation over the focus. Similar to the geometry term, $\Delta k_{\mathrm{d}} = \mathrm{d}\phi(\Omega, z)/\mathrm{d}z$. As discussed above, the long trajectories are more sensitive to intensity variation, so it is more difficult to achieve phase matching for long trajectories than for short trajectories [70]. The Δk_{n} and Δk_{p} terms depend on the generation gas, gas density and for the latter term ionization degree. For a given gas and intensity, these two terms are proportional to the gas density ρ, such as $\Delta k_{\mathrm{n}} + \Delta k_{\mathrm{p}} = \Lambda\rho$.

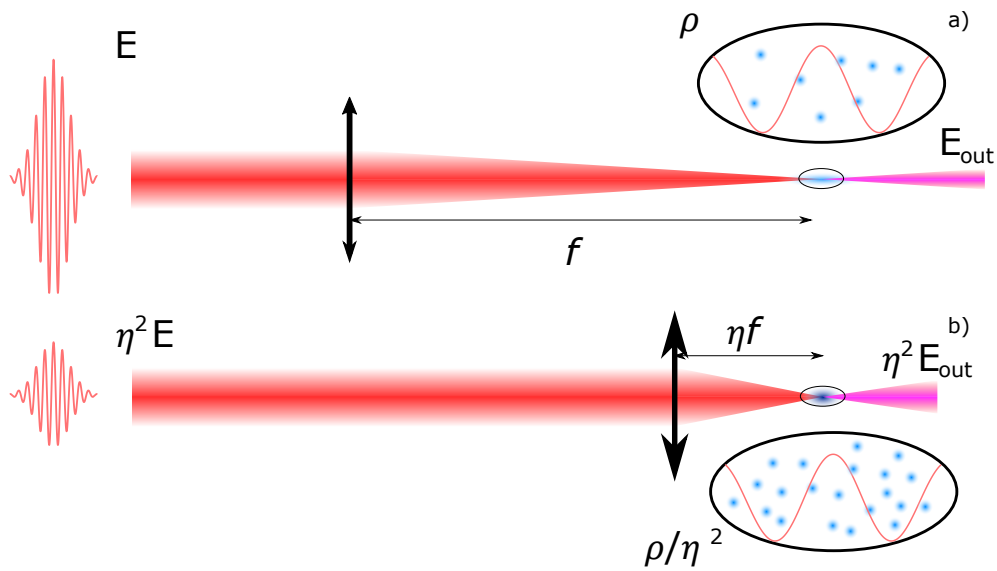

Figure 4.2: Scaling of HHG. In (a), a pulse with energy E is focused by a lens with focal length of f into a gas medium with density ρ. (b) shows a scaled setup with a lower pulse energy tightly focused in a dense gas medium.

In recent work, Heyl et. al. [71] suggest that HHG is scalable by varying parameters in a certain way, including the f number, the pulse energy and the gas density. The scaling law was derived from the nonlinear propagation equation and generally applies to many nonlinear optics phenomena in a gas medium. Here, a one dimensional derivation of the scaling law is presented. A more general discussion can be found in [69]. Let us assume that for one set of parameters, such as pulse energy E, beam waist w, Rayleigh length z_0 and gas density ρ, HHG is phase matched, i.e., $\Delta k = 0$. When the pulse energy is scaled by a factor of η^2, $E' = \eta^2 E$, the beam size has to be scaled as $w' = \eta w$, so that the intensity is the same to maintain the strength of the nonlinear interaction. Thus, the new Rayleigh length z_0' is equal to $\eta^2 z_0$, indicating that the z axis has to be scaled accordingly, i.e., $z' = \eta^2 z$. For the geometry and dipole phase terms, the scaling factor is introduced by the derivation

operator $\mathrm{d}/\mathrm{d}z' = \mathrm{d}/\eta^2\mathrm{d}z$. Hence, for the new focusing geometry, equation 4.14 becomes

$$\Delta k' = \Delta k'_{\mathrm{g}} + \Delta k'_{\mathrm{d}} + \Delta k'_{\mathrm{n}} + \Delta k'_{\mathrm{p}} \tag{4.15a}$$

$$= \frac{\mathrm{d}\Phi(z')}{\mathrm{d}z'} + \frac{\mathrm{d}\phi(\Omega, z')}{\mathrm{d}z'} + \Lambda\rho' \tag{4.15b}$$

$$= \frac{\Delta k_{\mathrm{g}}}{\eta^2} + \frac{\Delta k_{\mathrm{d}}}{\eta^2} + \Lambda\rho'. \tag{4.15c}$$

To achieve $\Delta k' = \Delta k/\eta^2 \approx 0$, the pressure, ρ', should be scaled according to ρ/η^2. Accordingly, the output pulse energy E_{out} is scaled by η^2, i.e., E'_{out} is equal to $\eta^2 E_{\mathrm{out}}$. Thus, this scaling law predicts that the laser should be focused with a large focal length (loosely) into a low density gas medium for energetic pulses and focused with a small focal length (tightly) into a dense gas medium for pulses with low energy (see figure 4.2). This result leads us to redesign a compact and high-pressure gas target, as described below.

4 Experiments and Results

4.1 Harmonic Generation Setup

In this thesis, a simple harmonic generation setup is used to generate and characterize the high-order harmonics. Figure 4.3 shows the setup used in **Papers I, III**. A previous version of the setup used in **Paper II** is described in reference [72]. A glass wedge pair controls the dispersion of the fundamental pulses, and an iris is used to vary the beam size to optimize phase matching. The laser beam is subsequently sent into a vacuum chamber and focused into a high-pressure gas jet with an achromatic lens. In the previous HHG setup, the gas jet was a needle gas jet which provided limited gas density for generation. The harmonics are subsequently sent to the characterization chamber for measuring of the spectrum and the photon flux. Between the generation chamber and the characterization chamber, a filter wheel is employed, with which the XUV spectrum can be selected by different materials, such as aluminum (Al), chromium (Cr), iron (Fe) and tin (Sn). The flat field XUV spectrometer includes a grating and an imaging detector with microchannel plates (MCP) and a phosphor screen. The grating used in this setup is an achromatic curved grating with variant groove spacing (Hitachi, 001-0640), so that the diverging XUV beam can be refocused into the detector plane for good spectral resolution [73]. The XUV beam profile, as shown in the insertion obtained using neon as the generating gas and a 200 nm Al filter, was measured by a calibrated XUV camera (Andor, iKon-L). A toroidal mirror with f=60 cm is placed in a 2f–2f configuration to focus the attosecond pulses to application setups, such as a PEEM setup. During the measurement of the XUV beam profile, the grating and the toroidal mirror were translated out of the beam by motorized translation stages.

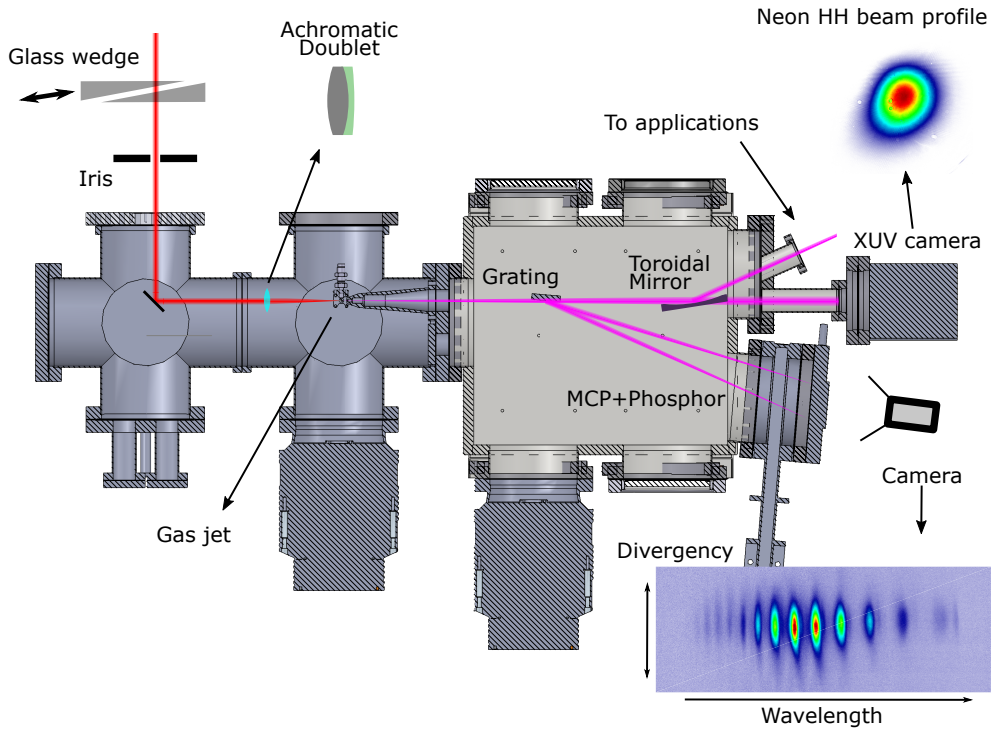

Figure 4.3: Setup for harmonic generation. The motorized wedge pair and the iris can adjust the phase of the pulse and the beam size respectively. The achromatic doublet focuses the beam into the gas jet system.

High-pressure Gas Jet

For our OPCPA system, the pulse energy is low (7 µJ) compared to conventional Ti:Sa laser systems (few mJ). This requires a tight focusing (f#≈10) to achieve sufficient light intensity in the medium. When considering our experimental condition where the laser beam (with diameter about 5 mm) is focused by an achromatic lens with a focal length of 5 cm, achieving a 100 µm confocal parameter, the estimated gas pressure for optimized phase matching is about 1 bar, according to the scaling law. This is challenging to implement in a vacuum environment. Our approach is a high-pressure gas jet, shown in figure 4.4(a). This gas nozzle contains two parts, an ejection and an extraction nozzle. The ejection nozzle is backed with high back pressure (10 bar) gas, and releases the gas to the interaction region through a pinhole (50 µm of diameter). The extraction nozzle with a 1 mm hole is placed 200 µm from the ejection nozzle, so that most of the gas is captured and pumped out through a rough pump. The extraction nozzle keeps the gas pressure in the vacuum chamber low, which is important for the applications. Figure 4.4(b) is a photo of the nozzle system when the system is operating. In this picture, the ejection nozzle is at

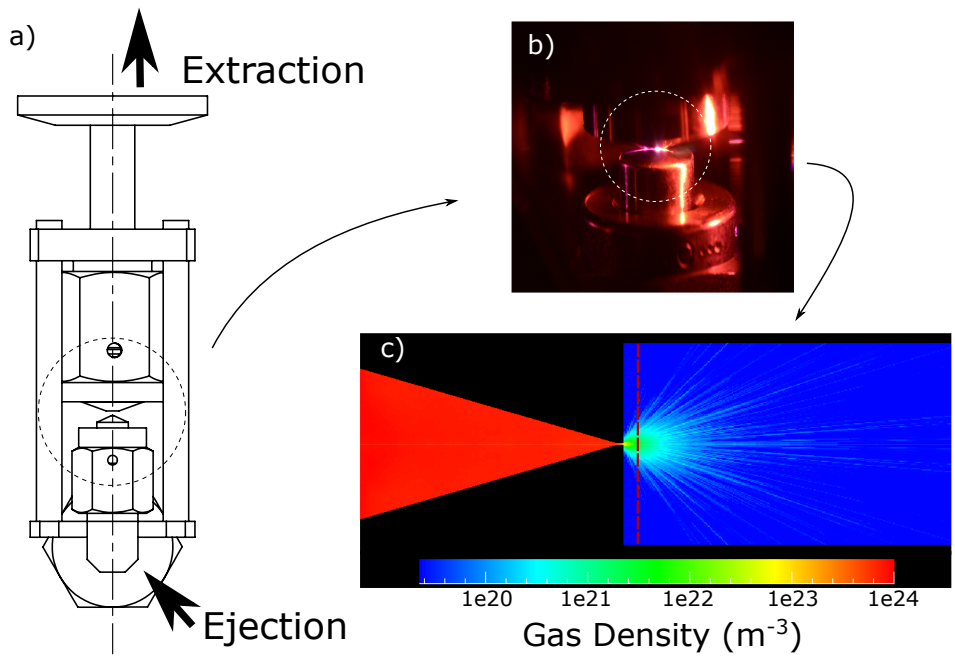

Figure 4.4: High-pressure gas jet. (a) is a drawing of the gas jet system, (b) a photograph of the high-pressure gas jet when operating and (c) a gas density map obtained by DSMC simulation.

the bottom and the extraction nozzle is at the top. The laser beam propagates from the left side and a bright spot is formed between the two nozzles due to plasma generation.

To evaluate the nozzle design and estimate the required backing pressure, a simple Direct Simulation Monte Carlo (DSMC) method was implemented. The *DS2V* program for this simulation was retrieved from reference [74]. The DSMC method is more suitable for this problem than the finite difference method which solves the Navier-Stokes equations, due to the supersonic flows and low gas density environment. Figure 4.4(c) shows the argon density map in logarithm scale for a nozzle with 50 µm diameter and 100 µm long pinhole. In this simulation, the gas is supplied from the left side. After passing through the pinhole, the gas quickly expands and propagates to the right side, leading to low gas density. The distance such that the laser beam can go through without clipping is estimated to be 100 µm away from the nozzle tip (indicated by a dashed red line). At this distance, according to the simulation, the gas density is reduced by about 30 times (−15 dB) from the back pressure. From this point, the length of the gas medium is about 100 µm long with a 3-fold reduction (−5 dB) at the beginning and end relative to the center. The experimental results, presented in **Paper I**, show that the harmonics are generated in an absorption-limited condition, with no observable Maker's fringes.

4.2 Conversion Efficiency Measurement

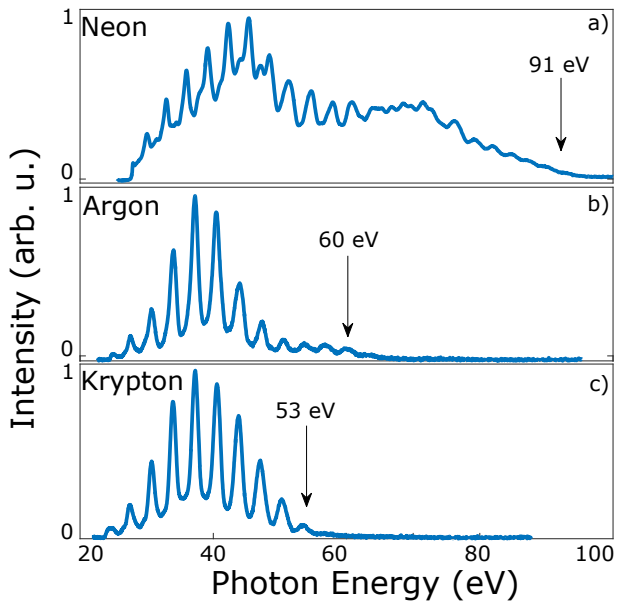

Figure 4.5: HHG spectra using (a) neon, (b) argon and (c) krypton. For the neon measurement, the metallic filter was not employed, and for Argon and Krypton results, a 200 nm Al filter was used.

In **Paper I**, the high-pressure gas jet was implemented and used to generated high-order harmonics with neon, argon and krypton. Figure 4.5 presents typical spectra in optimized conditions. The neon spectrum was measured without any filter and the argon and krypton spectra were measured with a 200 nm thick aluminum filter (transmitting from 25 eV to 75 eV). For the neon spectrum, the sharp edge on the left side (about 25 eV) is due to the limited detector size. Harmonics up to the 60th (about 90 eV) are observed. The complex spectral structure around 45 eV is due to the overlap of the first and second order diffraction of the grating. The harmonics close to the cutoff are blurred because the spectral resolution of the spectrometer is limited and because these frequency components are generated within fewer attosecond pulses. For the argon and krypton spectra, the drop of the harmonic strength at 25 eV is due to the cut-off of the Al filter (including the oxide layer), and the highest harmonic orders are 41 (62 eV) and 33 (52 eV) respectively. In the argon spectrum, the strength decreasing around 50 eV is due to the Cooper minimum of the photoionization cross section [75]. The different cutoff photon energy for these gases is due to the different ionization potentials, I_p, of these gases. The deeper the ionization potential, the higher the intensity required to reach the "optimum" ionization degree. Hence, the maximum ponderomotive energy (and therefore cutoff energy) is higher for neon than argon and krypton. In contrast, the direct contribution of the ionization potential, in the formula $\hbar\Omega = E_\mathrm{k} + I_\mathrm{p}$, is small.

The conversion efficiency was calculated by comparing the total energy detected by the XUV camera to the laser pulse energy. The results and experimental conditions of the measurements are listed in table 4.1. The conversion efficiency were found to be 4.0×10^{-8}, 1.3×10^{-6} and 4.2×10^{-6} for neon, argon and krypton respectively. These results are comparable to those achieved with kHz laser systems (slightly lower for Ar and Kr). Remarkably, the krypton harmonics were efficiently generated using only 2.2 µJ, indicating a good potential of this OPCPA-HHG system for applications.

Table 4.1: Generation conditions and results for neon, argon and krypton harmonics.

	Neon	Argon	Krypton
IR Pulse Energy (µJ)	5.0	3.1	2.2
Backing Pressure (bar)	30	10	8
XUV Energy per Shot (pJ)	0.056	0.155	0.280
Conversion Efficiency	4.0×10^{-8}	1.3×10^{-6}	4.2×10^{-6}

4.3 XUV-dispersion Scan

In **Papers II** and **III**, the HHG spectra are studied as a function of the fundamental dispersion and the CEP that are controlled by the glass wedges (figure 4.3). The few-cycle pulses from the OPCPA laser system are so short that the intensity at each half-cycle of the pulse varies rapidly, leading to rapid phase variation between the attosecond pulses in the pulse train. In the spectral domain, this effect leads to complex interference structures which change when the waveform of the fundamental pulse is different, such as by varying the CEP. This effect has been observed over many years [76–79]. In this thesis, we propose an interpretation of the interference pattern using a multiple pulse interference model. Figure 4.6 presents an argon spectrogram obtained at the beginning of this thesis work, which exhibits fringes over the whole range. The fringes in the spectrogram are spaced about 30 µm of glass insertion, corresponding to a π shift of the fundamental field.

With the upgraded laser system and HHG setup, a similar study was repeated by using three different gas media, neon, argon and krypton. Figure 4.7(a) and (b) present two XUV spectrograms in krypton and neon respectively. In the neon spectrogram, an interference pattern is observed, while in krypton, the fringes are not clearly visible due to insufficient resolution on the y-axis. In Kr, the position of the harmonics moves significantly when changing the glass insertion. This indicates a shift of the central frequency of the driving laser pulse due to the creation of a plasma that reshapes the fundamental pulse. In Ne, some CEP instabilities are present, leading to discontinuity of the fringes, such as the s shape fringes around 70 eV at -0.5 mm of glass insertion.

In **Paper III**, the result from argon was presented (figure 4.8(a)) and compared to a simulation (figure 4.8(b)) using our multiple pulse interference model. The simulation used the

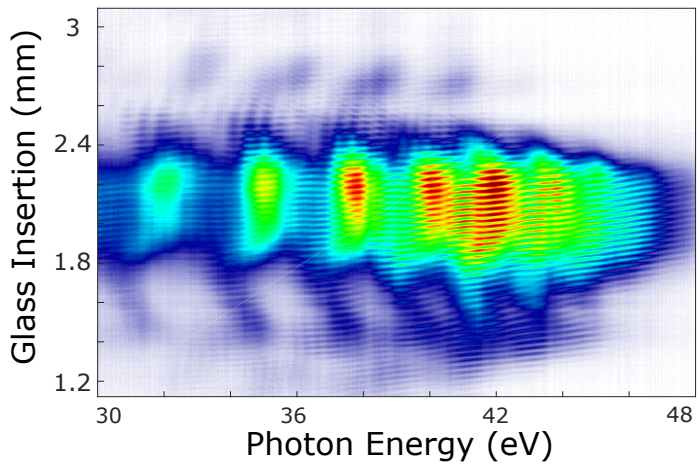

Figure 4.6: Argon XUV-dispersion scan obtained at the beginning of this thesis work, before the upgrade of the laser and HHG setup.

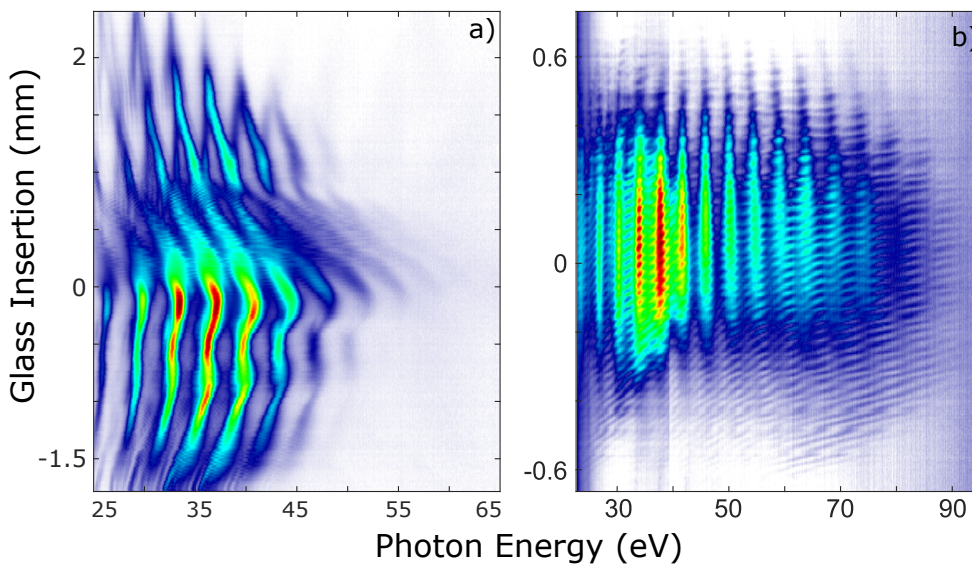

Figure 4.7: XUV spectrograms generated from (a) krypton and (b) neon. The abnormal harmonic structure in the krypton spectrogram is attributed to coupling between the plasma and the fundamental pulse.

fundamental pulse retrieved from the d-scan measurement. Generally speaking, the simulation result shows excellent agreement with the experimental result, including not only the CEP dependent fringes and harmonic structures, but also the vertical fringes around $\pm 0.7\,\mathrm{mm}$ glass insertion which is due to the complex pulse structure.

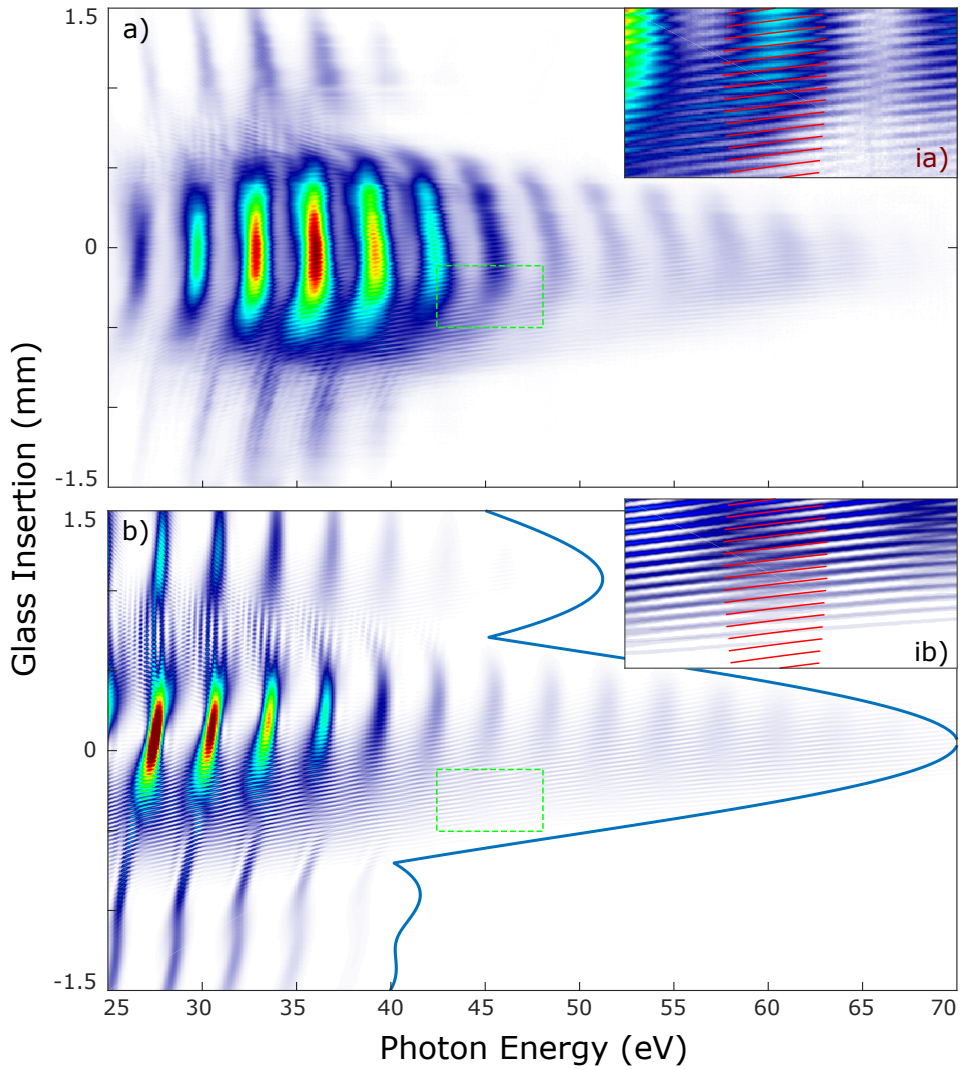

Figure 4.8: XUV spetrograms as a function of glass insertion from (a) measurement and (b) simulation. The blue curve in (b) indicates the classical cutoff calculated from the fundamental pulse. In the simulation plot, the color scale is adjusted to highlight the low intensity area. The areas measured in the green boxes are magnified and presented in insertions (ia) and (ib). In the insertions, the solutions of $f(\Omega) = 32\pi$ is plotted as red lines.

In order to understand the interference pattern, the multiple interference model was derived analytically by assuming a Gaussian fundamental pulse. More details on the derivation are given in **Paper III**. With this approximation, the phase term of equation 4.13 can be

rewritten as a polynomial of the pulse number m as

$$\tilde{A}_{\mathrm{tot}}(\Omega) = \sum_{m=n}^{l} A_m(\Omega) \exp\left(i(z(\Omega) + mf(\Omega) + m^2 s(\Omega))\right), \tag{4.16}$$

where $z(\Omega), f(\Omega)$ and $s(\Omega)$ are the zeroth, first and second order factors respectively, given by

$$\begin{aligned} z(\Omega) =& -\frac{\Omega\varphi}{\omega_0}\left(1 + \frac{b\varphi}{2\omega_0^2}\right) + \beta(\Omega - \Omega_{\mathrm{p}}) \\ &+ (1 + \frac{\varphi^2}{\omega_0^2\tau^2})\frac{\gamma}{I_{\max}}(\Omega - \Omega_{\mathrm{p}})^2 \end{aligned} \tag{4.17a}$$

$$f(\Omega) = \pi + \frac{\pi\Omega}{\omega_0} + \varphi\kappa(\Omega) \tag{4.17b}$$

$$s(\Omega) = -\frac{\pi}{2}\kappa(\Omega) \tag{4.17c}$$

with

$$\kappa(\Omega) = \frac{b\pi\Omega}{\omega_0^3} - \frac{2\pi}{\omega_0^2\tau^2}\frac{\gamma}{I_{\max}}(\Omega - \Omega_{\mathrm{p}})^2 \tag{4.18}$$

where $\alpha_0^{(\mathrm{s})}$ is assumed to be zero. These three terms depend on the peak intensity $I_{\max}$, chirp b, CEP φ and pulse duration τ of the fundamental pulse. The zeroth order term, $z(\Omega)$, is the phase of the zeroth ($m = 0$) attosecond pulse. It does not contribute to the final spectrum which measures the modulus square of the total spectral amplitude, $|\tilde{A}_{\mathrm{tot}}(\Omega)|^2$. To measure this term, a nonlinear measurement is required, such as reconstruction of attosecond beating by interference of two-photon transitions (RABBIT) [80] or streaking [25] which can be analyzed by the frequency resolved optical gating for complete reconstruction of attosecond bursts (FROG-CRAB) scheme [81].

The first order term $f(\Omega)$ acts like a multiple slit interference, and gives the basic structure of the harmonic spectrum, where the spectral strength reaches maxima when $f(\Omega)$ is equal to an integer times 2π. For example, when $\varphi\kappa(\Omega)$ is equal to zero, the regular odd harmonics are generated. The CEP dependence of $f(\Omega)$ can shift and change the spacing between harmonics, leading to the CEP dependent fringes that are observed in the experimental results and simulations. In the insertions of figure 4.8, a magnified area from the experimental result and simulation around zero glass insertion is shown. The solution of $f(\Omega) = 32\pi$ is also indicated as a red line. To match the plot to the experimental fringes in the y-direction, the absolute CEP of the fundamental pulse at zero glass insertion is set to 0.3π.

The contribution of the second order term $s(\Omega)$ is not intuitive, particularly when more

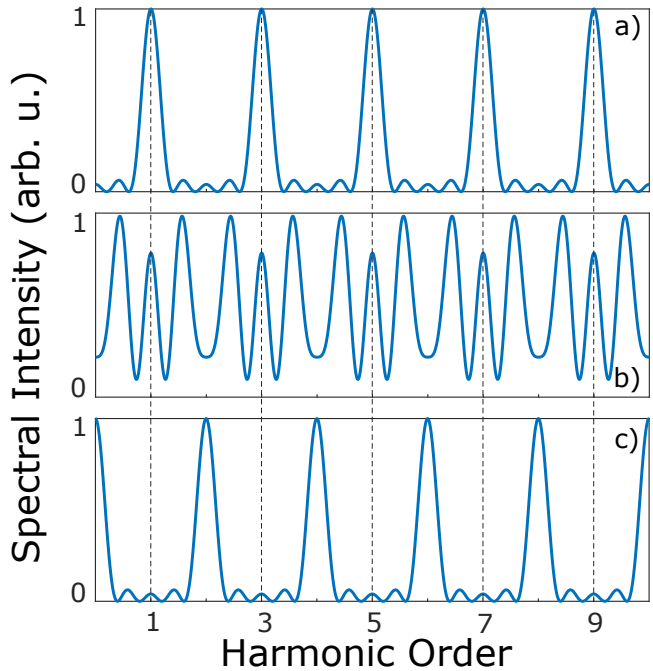

Figure 4.9: Calculated spectra with different $s(\Omega)$ values, (a) $s(\Omega) = 0$, (b) $s(\Omega) = 0.75\pi$ and (c) $s(\Omega) = \pi$.

than two pulses are interfering. In order to show the effect of the $s(\Omega)$ term, a simple simulation, including five equally strong pulses, is presented in figure 4.9. In (a), $\kappa(\Omega)$ and φ are set to be zero, so the spectrum appears as a regular odd-order harmonics. Using $s(\Omega) = 0.75\pi$, the spectrum becomes very complicated, and the small maxima become much stronger. When $s(\Omega) = \pi$, as presented in (c), the even harmonics dominate instead of the odd orders. This calculation also indicates that $s(\Omega)$ influences the "shape" of the harmonics: the harmonics are spectrally narrow when $s(\Omega)$ is close to zero; otherwise, the harmonics are broadened.

Chapter 5

Application: Attosecond PhotoEmission Electron Microscopy

In this thesis, an important application of our light source has been to characterize the surface electron dynamics on nanostructures. Electron dynamics in designed subwavelength structures can result in many interesting phenomena, such as negative refractive index [82] and surface plasmon [83, 84], leading to several applications, including metameterial [85], optical cloaking [86], surface enhancement Ramman scattering, and subwavelength wave guide [87]. To understand electron motion on the surface, our approach is a pump-probe scheme proposed by Stockman et al. in 2007 [19]. In this scheme, known as "Atto-PEEM", the attosecond temporal resolution from the pump-probe streaking measurement [25] is combined with the nanometer spatial resolution using a photoemission electron microscope (PEEM) setup.

Toward implementation of the concept of Atto-PEEM, we use the OPCPA laser system together with a PEEM setup. The high repetition laser system allows for a good signal-to-noise ratio for data acquisition while avoiding space charge effects [88]. Space charge occurs when electrons are highly concentrated in a small volume where they repel each other due to the Coulumb interaction, leading to a blurry image. To avoid this effect, we reduce the power of the laser beam on the sample so that only a few electrons are generated by one laser pulse. We studied several metallic samples with relatively simple geometry, such as nanocube, nanorice and nanowire. Using multiphoton photoemission from these metallic nanoparticles, we investigated the dynamic of field enhancements in the nanoparticles and the surface plasmon response to the external excitation field. We also utilized HHG radiation to acquire PEEM images using our 200 kHz HHG source, demonstrating better signal-to-noise ratio and spatial resolution than similar measurements at 1 kHz.

This part of the thesis was done in collaboration. The PEEM setup was provided by a local collaborator, Prof. Anders Mikkelsen, at the Division of Synchrotron Radiation Research; the samples were obtained trough NanoLund as well as the Chinese Academy of Science in Beijing.

In this chapter, we first give a small introduction to plasmonics and PEEM before summarizing the articles. We studied the electron yield using multiple photon absorption of nanocubes as a function of the polarization of the driving laser field (**Paper VIII**). We also studied the plasmon dynamics of nanorices and bowtie nanoantennas using interferometric autocorrelation (**Papers IX** and **X**). Finally, we presented our first XUV-PEEM image using the 200 kHz HHG source in **Paper XI**.

1 Nano-Optics: Plasmonics

When interacting with an electromagnetic field, the free electron gas in a plasma is polarized and is described by electric permittivity, given by [21, 89]:

$$\epsilon(\omega) = \epsilon_0 \left(1 - \frac{\omega_p^2}{\omega^2 + i\gamma\omega}\right) \tag{5.1}$$

where ω is the angular frequency of the field, ϵ_0 is the permittivity in vacuum, ω_p is the plasma frequency, and γ is the characteristic collision frequency. For an ideal undamped free electron gas, such that the collision frequency, γ, is zero, the plasma resonantly oscillates at a frequency called plasma frequency with an opposite phase to the driving field. This phenomenon is called plasma oscillation, plasmon or "Langmuir waves" [90].

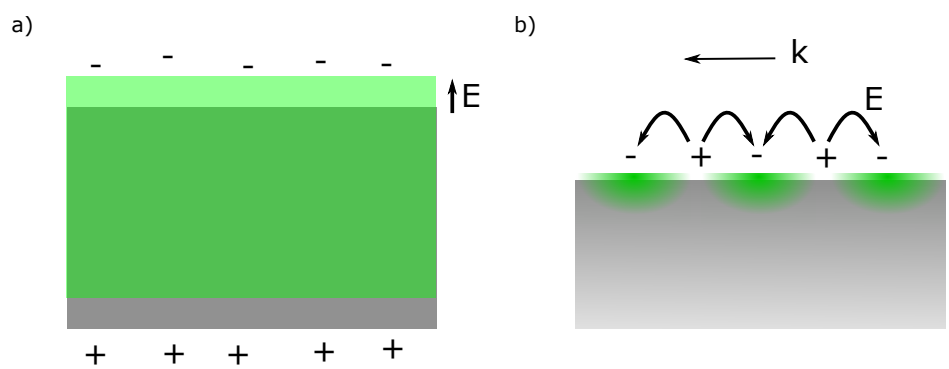

Figure 5.1: Schematic representation of a) a volume plasmon and b) a surface plasmon. The free electron gas is presented as green and the metal substrate is gray.

In noble metals, such as gold (Au) and silver (Ag), the conduction band with free electrons and ions behaves as a plasma, oscillating at its plasma frequency. This oscillation is called volume plasmon or bulk plasmon. The typical plasma frequency ω_p for these metals is in the UV range [91]. As figure 5.1(a) shows, the volume plasmon can be illustrated as the oscillating center of mass of the electron gas relative to the geometric center of the metal. However, this type of plasmon cannot be directly excited by optical waves. The volume plasma wave is a longitudinal wave, where the wave vector is parallel to the field, so that momentum can not be conserved.

In contrast, electrons at the interface between a conductor and vacuum can couple with the electromagnetic field. The created plasmon is called surface plasmon [89]. A simple example is the surface wave propagating along the surface, as shown in figure 5.1(b). When the physical size of the nanostructrure is comparable to the wavelength of the excitation field, the plasmons are confined to a small area and form a standing wave called localized surface plasmon. In the rest of this thesis, plasmon will refer to this localized surface plasmon, since we are concentrating on studying plasmons in nano-particles induced by optical waves.

Surface plasmon or localized plasmon may lead to localized electron distributions at the surface of nanostructures. According to Maxwell equations, $\nabla\vec{E} \propto \rho$, a high density of charges can induce very strong electric fields, which can be much stronger than the excitation field. This property is called surface enhancement. An intuitive understanding of surface enhancement is that the nanostructures can "focus" the light into a sub-wavelength area. Thus, a small focal spot and high intensity can even be achieved beyond the diffraction limit. In recent work [92], this localized field enhancement is used to probe the phase evolution over the beam waist of focused ultrafast pulses using a nanotip.

However, lifetimes of plasmon are often very short, due to the resistance of the material as described by the characteristic collision frequency γ. The characteristic collision frequency is typically around 100 THz [89], meaning the lifetime of plasmon is about ten femtoseconds ($1/\gamma$). Hence, ultrashort pulses should be used to study the dynamics of plasmonic fields.

2 PhotoEmission Electron Microscope

The electron microscope used in this thesis work is an integral sample stage photoemission electron microscope (IS-PEEM) produced by FOCUS GmbH. A schematic of this PEEM is presented in figure 5.2. The light illuminates the sample at grazing incidence (typically $\sim 25°$) and generates photoelectrons. The photoelectrons are collected by an extractor and magnified with an objective, as well as several projective lenses. The contrast aperture

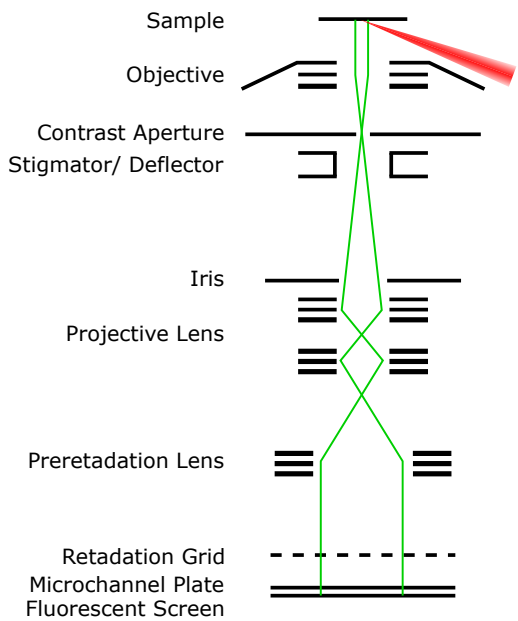

Figure 5.2: Principle of a photonemission electron microscope.

removes electrons propagating with large angles, which is similar to limiting the numerical aperture (NA) in optics, to optimize the spatial resolution. By applying and controlling the voltage of a retardation grid in front of the MCP and phosphor screen, electrons below a certain kinetic energy are suppressed. This grid acts as a high-pass filter. Finally, the image on the MCP detector is acquired by a CCD camera.

Photoemission

Photoemission is the electron source of this PEEM setup. Direct photoemission was first explained by Albert Einstein in 1905 [93]. A photon carrying an energy $\hbar\omega$, can be absorbed by an electron in a solid creating a hole. The electron escapes with kinetic energy $E_{\text{kin}} = \hbar\omega - P$, where P is the minimum energy required for the photoemission. From a modern perspective [94], P is usually broken down into two parts, $P = E_{\text{b}} + \Phi$, where E_{b} is the binding energy of the electron, i.e., the energy from a given ground state to the Fermi level, and Φ is the work function, which is the minimum energy required from the Fermi level to the free electron state. The final kinetic energy of photoelectron is $E_{\text{kin}} = \hbar\omega - E_{\text{b}} - \Phi$, where the work function is typically about 4-5 eV for a noble metal, and the binding energy is considered to be small for electrons around the Fermi level in a metal.

Before escaping from the metal surface, the excited electron can also scatter and share its energy with other electrons, depending on the electron mean free path length [94]. These electrons excited during the scattering process are called secondary electrons. When the excitation photon energy is relatively low, such as when using a mercury (Hg) lamp with $\hbar\omega \approx 4.9\,\mathrm{eV}$, the secondary electrons cannot be detected by the PEEM. This is because their small energy prevent them from escaping from the material. However, excitation with XUV light leads to more energetic primary photoelectrons, which scatter and generate secondary electrons, leading to a significant number of cascades of electrons. The broad energy distribution of these secondary electrons [88] may reduce the spatial resolution because of achromatic aberrations, as described in **Paper XI**.

In addition to single photon photoemission, multi-photon photoemission is utilized in our experiments, particularly in **Papers VIII-XI**. When using a low photon energy ($\sim 1.5\,\mathrm{eV}$ or 800 nm) NIR field, the photoemission process requires that multiple photons interact nonlinearly with the electron. We studied the electron yield as a function of the power of the IR field for gold nanoparticles in **Paper IX**. The electron yield was found to vary as $I^{3.4}$. This result implies that photoemission requires absorbing 3 to 4 photons, which matches the work function mentioned above (4-5 eV).

3 Experiments and Results

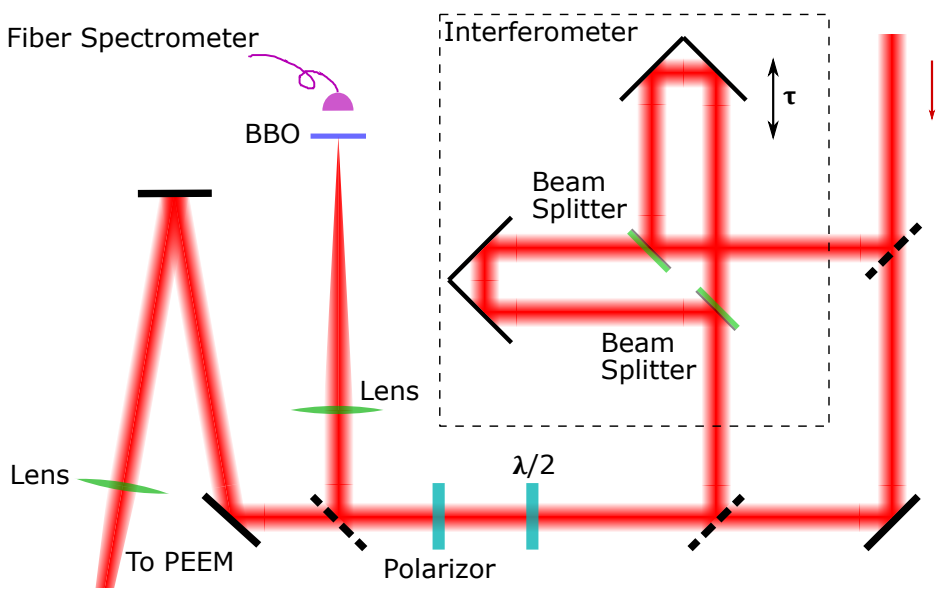

Figure 5.3: Scheme of the optical setup for the PEEM experiments

During this thesis work (**Papers VIII-XI**), we used both IR and XUV fields to study different metallic nanostructures, including nanocubes, bowtie nanoantennas, nanorices and nanowires. Table 5.1 summarizes the light source, nanoparticles and experimental methods used in **Papers VIII-XI**:

Table 5.1: Light source, nanoparticles and experimental methods used in **Papers VIII-XI**

Paper	Light Source	Object	Experimental Method
VIII	IR, Oscillator	Nanocubes	Influence of Laser Polarization
IX	IR, Oscillator	Bowtie Nanoantennas	Interferometric Autocorrelation
X	IR, Oscillator	Nanorices	Interferometric Autocorrelation
XI	XUV, HHG	Nanowires	Photoelectron Imaging

The optical setup for the IR experiments is shown in figure 5.3. The laser beam from the oscillator is sent to a compact Michelson interferometer, which splits the pulse into two replicas and delays them up to ± 250 fs with a piezo driven delay stage. For the polarization-dependent measurement, the interferometer was bypassed. A broadband half-wave ($\lambda/2$) plate and a polarizer were used to attenuate the beam power and rotate the polarization of the beam. The beam was subsequently focused by a single plano-convex lens ($f = 300\,\mathrm{mm}$) to the sample. A replica of the lens and the optical window were used to build an auxiliary beam line in air for characterizing the pulse duration at the focus, using the d-scan technique [32].

3.1 Influence of the IR Polarization on Plasmonic Excitation

In this experiment (**Paper VIII**), we study that the photoelectron yields from the corners of the silver nanocubes as a function of the polarization of the fundamental field. The nanocubes with a side dimension of $250\,\mathrm{nm}$ (figure 5.4(a)) are placed on an indium tin oxide (ITO) coated glass substrate. An example of experimental results is shown in figure 5.4(b)-(e) (see **Paper VIII** for more details). Using p-polarization (figure 5.4(b)), the top corner is the brightest spot, while with s-polarization (figure 5.4(d)), the two corners on the sides are lit up. Furthermore, using intermediate states of polarization, the bright spot moves between the right and left sides of the nanocube. To verify and understand the experimental results, a finite difference time domain (FDTD) simulation is employed. The FDTD based on solving Maxwell's equations allows us to simulate the near field at the nanocube. The signal strength, which is proportional to the electron yield, is estimated by calculating

$$S(\vec{r}) = \int_{-\infty}^{+\infty} \mathrm{d}t \, |E_{\mathrm{tot}}(\vec{r}, t)|^6 \tag{5.2}$$

corresponding to three-photon photoemission, where E_{tot} denotes the total electric field.

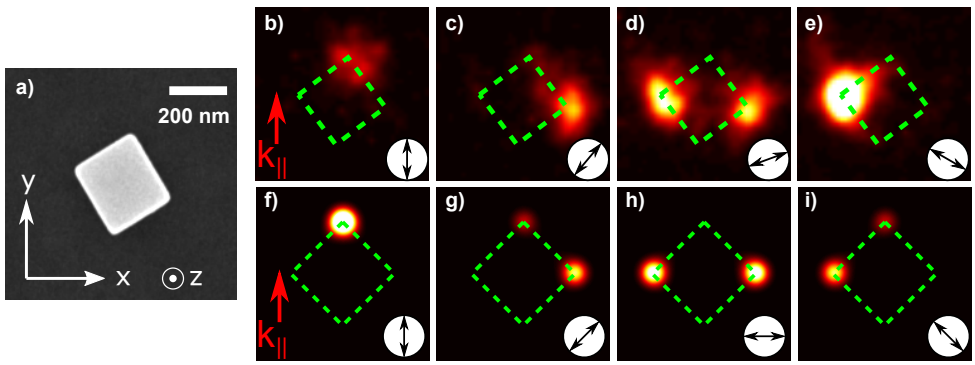

Figure 5.4: Nanocube sample, (a) Scanning Electron Microscope (SEM) image, (b)-(e) PEEM image with different polarizations of IR field, (f)-(i) Calculated electron yield according to FDTD simulations.

The simulation results (figure 5.4(f)-(i)) reproduce the experimental observation well. This result can be explained by separating the excitation due to s- and p-polarization, as

$$E_{\mathrm{tot}}(\vec{r},t) = E_{\mathrm{s}}(\vec{r},t)\cos(\theta) + E_{\mathrm{p}}(\vec{r},t)\sin(\theta). \tag{5.3}$$

where E_{s} and E_{p} are the excited near field when using s- and p-polarization respectively, and θ is the angle of the polarization with respect to s-polarization. S-polarization excites a mode in the x-direction with strong surface enhancement at the right and left corners. For p-polarization, the in-plane electric field component is in the y-direction, leading to enhancement at the top and bottom corners. However, due to the grazing incidence, the electric field component which is perpendicular to the (x, y) plane, can also excite another plasmon mode in the z-direction. The mode in the y-direction can interfere with this extra mode, so that the top corner is more visible than the bottom one. For the intermediate polarization, the total near field is given by the superposition of the modes excited by both the s- and p-polarization; by changing the phase relation, the interference maximum can appear either at the right or left corner.

3.2 IR-IR Interferometric Autocorrelation Experiments

In **Paper IX** and **X**, we use an interferometric method [95, 96], to provide information about the pulse structure in the vicinity of close to the nanostructures, as well as the carrier frequency, similar to an optical interferometric autocorrelation. The total near field on the nanoparticle is given by the superposition of the excited fields induced by the two pulses:

$$E_{\mathrm{tot}}(\vec{r},t) = E_0(\vec{r},t) + E_0(\vec{r},t-\tau) \tag{5.4}$$

where $E_0(\vec{r}, t)$ is the near field excited by a single fundamental pulse and τ is the time delay between the two pulse replicas. As in section 3.1, the signal is due to nonlinear photoemission with absorption of 3-4 photons (equation 5.2).

Nanorice

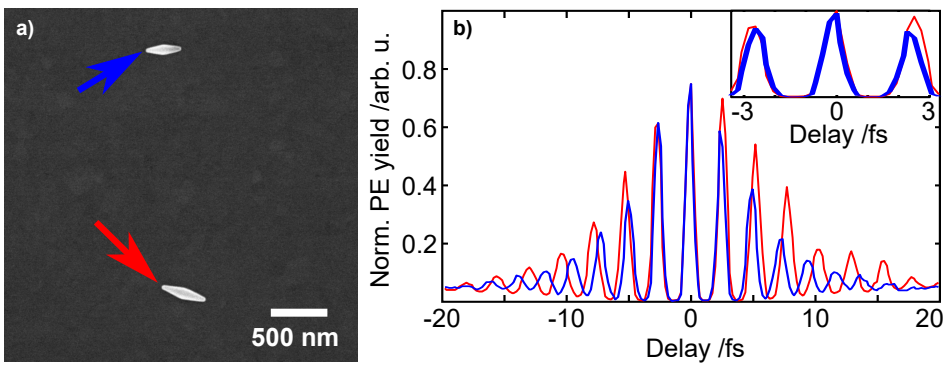

Figure 5.5: Nanorice sample, (a) SEM image and (b) auto-correlation traces of multiphoton photoemission yield. Two colors, blue and red, indicate the two nanoparticles and the corresponding auto-correlation traces. The insert magnifies the overlap range of the two traces.

The silver nanorice, which is very close to a nanoellipsoid whose resonance can be described analytically [97], has a simple and smooth geometry. In the experiment described in more details in **Paper x**, the nanorice samples can have a variable length around 320-600 nm with diameter of $\sim$ 100 nm. Figure 5.5(a) shows two nanorice particles with about 320 nm and 410 nm length respectively; the corresponding autocorrelation traces are presented in figure 5.5(b). For small time delays, as shown in the inset, the two traces are very similar; but for larger delays, the peaks are clearly separated from each other, i.e., the oscillation has a different frequency. This result, which is also validated by the FDTD simulations, can be explained by the fact that the length of the nanoparticle affects the "cavity" length of the plasmonic standing wave. The long and short nanoparticles are then resonant with long and short wavelength components of the optical field, leading to a difference in oscillation frequency.

Bowtie Nanoantennas

A typical bowtie nanostructure, which can be seen in figure 5.6(a-c), contains two isosceles triangle, with a 20 nm gap between the two narrow tips. This geometry leads to particularly high field enhancement, useful for strong field applications [98]. The bowtie samples used in this experiment are fabricated from a 25 nm gold film on a sapphire substrate with the

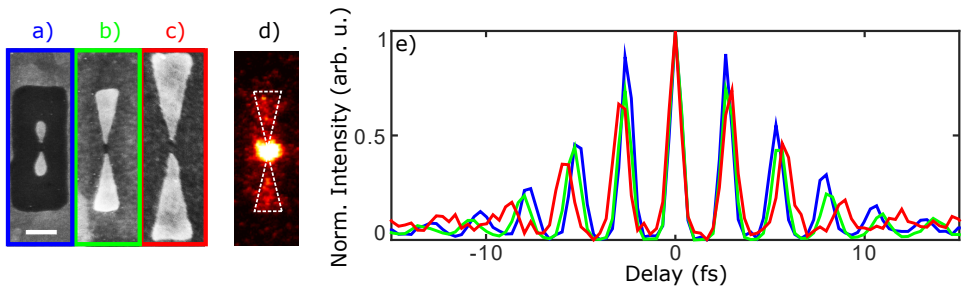

Figure 5.6: Nanobowtie sample, (a)-(c) SEM images for three different dimensions, (d)PEEM image with mercury lamp and IR field, and (e) corresponding auto-correlation traces. The colors of the image refer to the colors in (a), (b) and (c).

method described in **Paper IX**. The bowtie nanoantennas are fabricated on a 25 µm × 25 µm array so that they can be excited at the same time by the same laser pulse.

Similarly to the work on nanorices, we first study how the size of the nanoparticle influences the plasmonic response. The bowtie samples vary in length from 92 nm to 390 nm. Figures 5.6(a-c) show the scanning electron microscope (SEM) images of the bowtie nanoantenna with 92, 195 and 390 nm length respectively and figure 5.6(d) shows the strong field enhancement around the nanotip. Figure 5.6(e) presents the corresponding autocorrelation traces for the three bowtie samples. Similar to the nanorice, we find that the longer nanoparticle resonates at the longer wavelength.

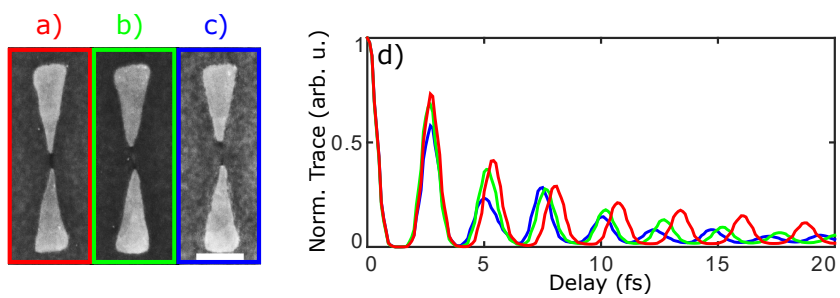

Figure 5.7: Nanobowtie sample, (a)-(c) SEM images for three similar sizes but different shapes, and (d) the calculated autocorrelation traces using FDTD simulations of the corresponding nanobowties.

In **Paper IX**, we also studied how the shape of the nanoparticle influences the plasmonic response. Due to the difficulty of the fabrication technique, the exact shape of the bowtie nanoantennas cannot be exactly reproduced. Results of the FDTD calculations are shown in figure 5.7(d), whose corresponding bowties are show in figure 5.7(a-c). These three traces have very different resonance frequencies which can be attributed to differences in gap length, radius of curvature of the tip or triangle length.

3.3 XUV Experiments

Paper XI presents a review of experimental effects towards "Atto-PEEM". In this article, different HHG setups as light sources for PEEM are presented. My contribution to this work was to obtain the first experimental image using PEEM illuminated by the XUV radiation generated from the 200 kHz laser system. Figure 5.8(b) presents the photoemission image of two silver nanowires (200 nm wide) on a gold substrate. This image was acquired with a 30 s integration time, and the FWHM width of the nanowire image is about 350 nm. It is compared to a similar image of silver nanowires using a 1 kHz system [88]. This image presented in figure 5.8(a) is obviously noisier than figure 5.8(b), even though the integration time is 400 s. The measured FWHM width of the nanowire in the image is about 900 nm. This work underlines that by using a high repetition rate (200 kHz) light source system, the signal-to-noise ratio and spatial resolution improve while the integration time is reduced by an order of magnitude.

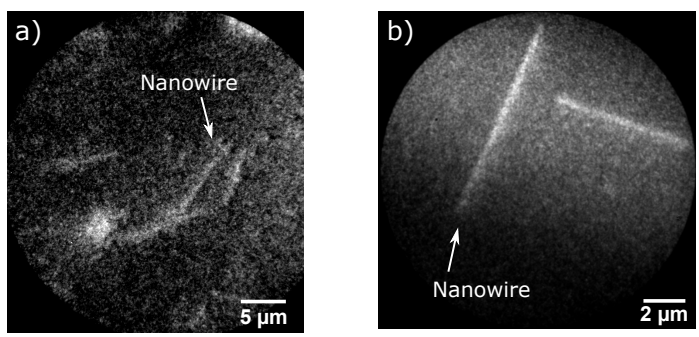

Figure 5.8: XUV-PEEM images acquired by (a) 1 kHz system [88], and (b) 200 kHz system.

Chapter 6

Conclusion and Outlook

1 Summary

In this thesis, we present a 200 kHz few-cycle OPCPA laser system (**Paper I**). This system provides 7.5 μJ sub-7 fs CEP-stabilized pulses for high-order harmonic generation and PEEM. To characterize the temporal profile of the ultrashort pulses, we developed a compact version of a single shot d-scan setup (**Paper V**). We have also developed a fast retrieval algorithm for d-scan traces (**Paper IV**). For characterizing the spatio-temporal coupling effects, a spatially-resolved Fourier transform spectrometer was demonstrated (**Paper VI**). This spectrometer was used to characterize the laser pulses from the OPCPA laser system as well as a vortex pulse generated from a spiral wave plate (**Paper VII**).

We generated high-order harmonics by tightly focusing the laser beam into a homemade high-pressure gas jet. By characterizing the spectra and the photon flux of the harmonics, we deduced conversion efficiencies of 4.0×10^{-8}, 1.3×10^{-6} and 4.2×10^{-6} using neon, argon and krypton respectively (**Paper I**). These conversion efficiencies are close to the record in the literature [99, 100]. We also studied HHG spectra as a function of the CEP and dispersion of the fundamental pulse (**Paper II** and **III**). Due to the phase difference between attosecond pulses in a pulse train, which is induced by the intensity-dependent dipole phase, the HHG spectra show a rich pattern of interference fringes. By using a multiple pulse interference model, the interference pattern was well reproduced and could be explained.

The IR and attosecond pulses were sent to a PEEM setup and used to study surface plasmonic dynamics of metallic nanoparticles. We studied the yield of electrons emitted by multiphoton absorption as a function of the polarization of the fundamental pulse in nanocubes (**Paper VIII**). An interferometric time-resolved scheme was used to study the

time-dependent response of bowtie nanoantennas (**Paper IX**) and nanorices (**Paper X**). We also used high-order harmonics to acquire PEEM images (**Paper XI**).

2 Outlook

The unstable beam profile from the fiber amplifier stages limits the performance of the laser system. An upgrade of the fiber laser system has now been ordered to solve this issue. The parametric amplifier stages have to be redesigned to benefit from the high pump pulse energy. In order to achieve higher output pulse energy, a third NOPA stage is also planned. Another possible direction is to use a frequency-domain optical parametric amplification (FOPA) scheme [101] and multiple pass geometry [102], to achieve high conversion efficiency in the OPA stages.

For high-order harmonic generation, one future direction is the generation of isolated attosecond pulses. To achieve isolated attosecond pulses using few-cycle driving pulses, gating technologies have to be implemented, such as noncollinear optical gating [103], polarization gating [104], lighthouse effect [49], etc. Our plan is to design and construct a two-color interferometer, using a combination of the fundamental field and its second harmonic, with the right phase difference so that every second attosecond pulse can be suppressed. Hence, it will be possible to gate one single attosecond pulse from a pulse train that ordinarily contains three attosecond pulses.

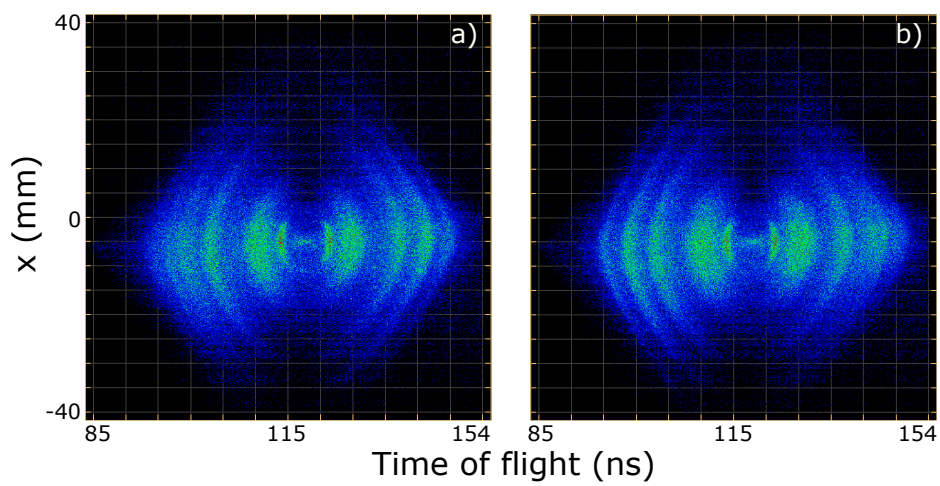

Figure 6.1: Preliminary result from the 3D electron spectrometer

For PEEM, a manuscript, which studies polarization-dependent electron yield by absorbing multiple photons of InAs nanowires, has been accepted by *Nano Letter* during the writing

progress. In near future, the goal for the PEEM project is still to achieve Atto-PEEM. However, the ultimate Atto-PEEM is still challenging. Further investigations are clearly needed to evaluate in which experiments temporal and spatial resolution can be combined. This includes looking for the "good" combination of nanoparticles and substrate.

A *Coincidences entre Ions et Electrons Localisés* (CIEL) setup to study ionization in atomic- and molecular systems in 3D [20, 105] has been built in our laboratory. This spectrometer has recently been tested. Figure 6.1 presents preliminary results acquired in helium by sending the XUV beam together with the driving fundamental IR pulse. The two 2D spectra are plotted as a function of the detector x-direction and time-of-flight, corresponding to the electron momentum component p_x and p_z respectively. These spectra are found to be CEP-dependent. In figure 6.1(a), the spectrum appears as continuum on the left side, while the spectrum shows individual harmonics on the right side. By varying the fundamental CEP by π, the spectrum shown in (b), the left–right symmetry of (a) is reversed.

In the future, by optimizing the laser system and using an XUV–IR interferometer, we plan to perform time-resolved experiments, such as RABBIT and streaking measurements, to study electron dynamics during the ionization process at an unprecedented repetition rate, using one of the first 200 kHz attosecond sources.

Scientific publications

Author contributions

Paper I: Compact 200 kHz HHG source driven by a few-cycle OPCPA

This paper presents an efficient 200 kHz high-order harmonic generation source driven by an OPCPA laser system. I shared the first authorship of this article with Anne Harth. I worked on optimizing the laser system, characterizing the pulse and measuring the spectrum and the flux of harmonic generation with Anne Harth. I analyzed the data of the complete characterization of the pulses. I also wrote a part of the manuscript and participated all the discussions about this work.

Paper II: Carrier-envelope phase dependent high-order harmonic generation with a high-repetition rate OPCPA-system

This paper presents our first harmonic generation result using the 200 kHz few-cycle OPCPA laser system. We demonstrated high-order harmonic generation with few µJ of pulse energy using tight focusing geometry. We also observed and discussed the CEP-dependence of the HHG. In this work, I participated to the experimental work, including optimizing the laser system and calibrating the XUV spectrometer. I also participated to the data analysis and discussions for the manuscript.

Paper III: Phase Control of Attosecond Pulses in a Train

This paper studies the dependence of HHG with dispersion and CEP. We present experimental results and theoretical interpretation based on a multiple pulse interference model and semi-classical calculations. I did the experiment together with Anne Harth, and developed the theoretical model. I took the major responsibility on writing the manuscript.

The first authorship of this article was shared with Anne Harth.

Paper IV: Fast iterative retrieval algorithm for ultrashort pulse characterization using dispersion scans

This paper presents a new fast algorithm for retrieving a dispersion scan trace for short pulse characterization. I worked on the laser system and participated to the data acquisition when using the OPCPA laser system. I verified the algorithm by performing independent simulations.

Paper V: Compact single-shot d-scan setup for the characterization of few-cycle laser pulses

This paper presents a design and implementation of the compact single-shot d-scan setup. I participated to the discussions on the design and did the ray-tracing simulations to verify the design. The first authorship of this article was shared with Maïté Louisy. I participated to building, optimizing and calibrating the setup as well as performing the data analysis. I also wrote a part of the manuscript.

Paper VI: Spatiotemporal characterization of ultrashort laser pulses using spatially resolved Fourier transform spectrometry

This paper presents a novel spatially-resolved Fourier transform spectrometer for spatio-temporal characterization of ultrashort pulses. We implemented this setup and characterized a pulse with angular chirp. I operated and optimized the laser for the measurements and participated to the discussions.

Paper VII: Spatiotemporal characterization of ultrashort optical vortex pulses

This paper presents the spatio-temporal characterization of a ultrashort vertex pulse using the spatially-resolved Fourier transform spectrometer. We demonstrated the power and precision of this 3D characterization method. In this work, I worked on preparing the laser system and participated on the discussions.

Paper VIII: Direct subwavelength imaging and control of near-field localization in individual silver nanocubes

In this paper, we studied the plasmonic localization of silver nano-cubes as a function of polarization of the fundamental pulses, by using ultrashort laser pulses and a photoelectron emission microscope. In this work, I prepared the laser system for the measurements, aligned the optical setup and participated to the discussions of the results.

Paper IX: Size and shape dependent few-cycle near-field dynamics of bowtie nanoantennas

This paper presents the measurements and simulations of near-field dynamics of bowtie nanoantennas. We performed an IR-IR pump-probe experiment to measure the electron yield as a function of time delay. In this work, I prepared the laser system and aligned the interferometer. I also participated to the data acquisition and discussion of the results.

Paper X: Nanoscale imaging of local few-femtosecond near-field dynamics within a single plasmonic nanoantenna

This paper presents a time resolved measurement of nanorice particles from which we can acquire information on plasmon dynamics. I prepared the laser system and the interferometer for the time-resolved measurements. I participated to the discussions of the experimental results.

Paper XI: Imaging Localized Surface Plasmons by Femtosecond to Attosecond Time-Resolved Photoelectron Emission Microscopy –"ATTO-PEEM"

This book chapter is a general summary of the up-to-date developments towards the atto-PEEM scheme for studying surface plasmon dynamics. It reviews the history of the Attosecond Time-Resolved Photoelectron Emission Microscopy and shows some current results from several research groups. I contributed to part of the experimental results from the Lund team, including preparing the OPCPA laser amplifier system, generating high-order harmonics and aligning the optical path to the PEEM setup. I also participated to the acquisition and to the discussion of the experimental results.

Acknowledgements

During the last four and a half years of this PhD study, I have met and worked with many people. These people are very important and their help and supports make this thesis possible.

First of all, I would like to thank my three supervisors. I thank my main supervisor, Anne L'Huillier, for providing me such an opportunity to join the amazing group in Lund and to work with a fascinating project. Thank her for giving me a great freedom on choosing and working on different topics. I also thank her for her helps and encouragements to me when I faced problems. Furthermore, I thank my co-supervisors, Cord L. Arnold and Miguel Miranda. Thank them for discussing physics, sharing the "tricks" on aligning lasers and fixing all the annoying problems in the lab, such as pumps and chillers.

During this thesis work, I acquired a lot of helps and supports from many collaborators. Therefore, I want to thank the "MHz" team: thank Anne Harth for being a "quasi-supervisor" who taught me a lot about the OPCPA; thank Piotr Rudawski for helping me since the very beginning of my study; thank Yu-chen Cheng for his fast learning; thank Sara Mikaelsson for her constantly positive attitude; thank Saikat Nandi for his rich knowledge of physics; thank Lisa Rämisch for bringing up interesting topics during coffee breaks and thank Jan Vogelsang for joining us. I want to thank Christoph M. Heyl for his well-understanding on HHG and great ideas; thank Maïté Louisy for working together with the single-shot d-scan; and thank Mathieu Gisselbrecht for all the interesting discussions and his rhetoric skills. I thank Johan Mauritsson for his kindness; thank Eleonora Lorek for her caring mind; thank Stefanos Carlström for his mathematics and multilingual skills. I want to thank the PEEM team: thank Anders Mikkelsen for his smart ideas and "infinity" amounts of samples; thank Arthur Losquin for his "optimistic" mind and being a plasmonic specialist; thank Erik Mårsell for his jokes and great skills on operating the PEEM; thank Lukas Wittenbecher for his modesty and being my neighbor; and thank Robin Svärd for working with us, even though that was just a few months. I thank the collaborators from Hanover, Uwe Morgner, Jan Ahrens, Oliver Prochnow and Thomas Binhammer, for enjoyable collaborations. I would also like to thank Mette B. Gaarde and Kenneth J. Schafer

for their valuable comments.

I would like to thank the rest of the atto-group. I want to thank the "10Hz" team: Fabian Brunner, Helene C. Alteirac, Jasper Peschel, Hampus Wikmark, Sylvain Maclot, Filippo Campi, Jan Lahl, Linnea Rading, Fernando Brizuela, Bastian Manschwetus and Per Johnsson for sharing the lab and wish them can achieve XUV-autocorrelation soon in the near future. I thank the "Atto-Lab" and "Development lab" people: Samuel Bengtsson, David Busto, Neven Ibrakovič, Marija Kotur, Marcus Isinger, Lana Neoričić, Shiyang Zhong, Emma Simpson, Chuang Lu, Anna Olofsson, Timothé Ramboazanaka, Diego Guenot, Esben Witting Larsen, David Kroon, Jana Preclíková for being a great neighbor.

I enjoyed the awesome working environment in the division. I firstly want to thank my officemates: Anne H., Yu-chen, Saikat, Sara, Samuel, Qian, Jenny, Arthur and Ingrid for the awesome offices. Especially, I want to thank Samuel for organizing the great office and many funny activities. Furthermore, I would like to thank Esben, Stefanos and Anne H. for a lot of interesting discussions with different interesting topics. I would like to thank the head of division Claes-Göran Wahlström and the administrative team, including Åke Johansson, Anne Petersson Jungbeck, Jakob Testad, Camilla Nilsson and Bertil Hermansson, for creating the great working environment and supporting our work. Finally, I also want to thank the rest of colleagues and friends in atomic physics. Particularly, I want to thank Amélie Jarnac and Xiaocui WaAng for the nice parties and thank Chien-Ming Tu for biking together to Lomma.

Finally, I want to thank all the friends with whom I had a lot of fun during my PhD. I would like to thank Haofeng "Kshui" Xu and Chuan "Sam" Wang for being my best friends even though we are so far away from each other. I thank Philippe Cyr for inviting me to visit his new family. I want to thank the LCBC friends: Bo Zhou, Yupan Bao, Lai "Future" Wei, Zhiwei Chang, Zhecheng Shao, Olof Nyman, Wenxin Ning, Chengdong Kong, Zhongshan Li, Zhendong "Rhinoceros" Wu, Fengyuan Jiang, Miaoxin Gong, Yongchao "Shuker" Zhang, Lu Chen and Minjie Zheng, for all the badminton games and parties.At the end, I want to thank my mother and father for their caring and support from China. I may not achieve a PhD in physics if we don't discuss physics and electronics since I was a child!

Thank you all! Tack så mycket!

References

[1] T. H. Maiman. Stimulated optical radiation in ruby. *Nature*, 187(4736):493–494, 1960.

[2] P. A. Franken, A. E. Hill, C. W. Peters, and G. Weinreich. Generation of optical harmonics. *Phys. Rev. Lett.*, 7(4):118, 1961.

[3] L. E. Hargrove, R. L. Fork, and M. A. Pollack. Locking of he⁻ne laser modes induced by synchronous intracavity modulation. *Appl. Phys. Lett.*, 5(1):4–5, 1964.

[4] U. Morgner, F. X. Kärtner, S. H. Cho, Y. Chen, H. A. Haus, J. G. Fujimoto, E. P. Ippen, V. Scheuer, G. Angelow, and T. Tschudi. Sub-two-cycle pulses from a kerr-lens mode-locked ti:sapphire laser. *Opt. Lett.*, 24(6):411–413, 1999.

[5] D. Strickland and G. Mourou. Compression of amplified chirped optical pulses. *Opt. Commun.*, 55(6):447 – 449, 1985.

[6] D. A. Grukh, V. A. Bogatyrev, A. A. Sysolyatin, V. M. Paramonov, A. S. Kurkov, and E. M. Dianov. Broadband radiation source based on an ytterbium-doped fibre with fibre-length-distributed pumping. *Quantum Electron.*, 34(3):247, 2004.

[7] S. Hädrich, M. Kienel, M. Müller, A. Klenke, J. Rothhardt, R. Klas, T. Gottschall, T. Eidam, A. Drozdy, P. Jójárt, Z. Várallyay, E. Cormier, K. Osvay, A. Tünnermann, and J. Limpert. Energetic sub-2-cycle laser with 216 w average power. *Opt. Lett.*, 41(18):4332–4335, 2016.

[8] A. Dubietis, R. Butkus, and A. P. Piskarskas. Trends in chirped pulse optical parametric amplification. *IEEE J. Sel. Topics Quantum Electron.*, 12(2):163–172, 2006.

[9] S. Prinz, M. Haefner, C. Y. Teisset, R. Bessing, K. Michel, Y. Lee, X. T. Geng, S. Kim, D. E. Kim, T. Metzger, et al. Cep-stable, sub-6 fs, 300-khz opcpa system with more than 15 w of average power. *Opt. Express*, 23(2):1388–1394, 2015.

[10] J. Rothhardt, S. Demmler, S. Hädrich, J. Limpert, and A. Tünnermann. Octave-spanning opcpa system delivering cep-stable few-cycle pulses and 22 w of average power at 1 mhz repetition rate. *Opt. Express*, 20(10):10870–10878, 2012.

[11] R. Budriūnas, T. Stanislauskas, J. Adamonis, A. Aleknavičius, G. Veitas, D. Gadonas, S. Balickas, A. Michailovas, and A. Varanavičius. 53 w average power cep-stabilized opcpa system delivering 5.5 tw few cycle pulses at 1 khz repetition rate. *Opt. Express*, 25(5):5797–5806, 2017.

[12] J. M. J. Madey. Stimulated emission of bremsstrahlung in a periodic magnetic field. *J. Appl. Phys.*, 42(5):1906–1913, 1971.

[13] D. A. G. Deacon, L. R. Elias, J. M. J. Madey, G. J. Ramian, H. A. Schwettman, and T. I. Smith. First operation of a free-electron laser. *Phys. Rev. Lett.*, 38:892–894, 1977.

[14] A. McPherson, G. Gibson, H. Jara, U. Johann, T. S. Luk, I. A. McIntyre, K. Boyer, and C. K. Rhodes. Studies of multiphoton production of vacuum-ultraviolet radiation in the rare gases. *J. Opt. Soc. Am. B*, 4(4):595–601, 1987.

[15] M. Ferray, A. L'Huillier, X. F. Li, L. A. Lompre, G. Mainfray, and C. Manus. Multiple-harmonic conversion of 1064 nm radiation in rare gases. *J. Phys. B: At., Mol. Opt. Phys.*, 21(3):L31, 1988.

[16] T. Popmintchev, M.-C. Chen, D. Popmintchev, P. Arpin, S. Brown, S. Ališauskas, G. Andriukaitis, T. Balčiunas, O. D. Mücke, A. Pugzlys, A. Baltuška, B. Shim, S. E. Schrauth, A. Gaeta, C. Hernández-García, L. Plaja, A. Becker, A. Jaron-Becker, M. M. Murnane, and H. C. Kapteyn. Bright coherent ultrahigh harmonics in the kev x-ray regime from mid-infrared femtosecond lasers. *Science*, 336(6086):1287–1291, 2012.

[17] J. Li, X. Ren, Y. Yin, K. Zhao, A. Chew, Y. Cheng, E. Cunningham, Y. Wang, S. Hu, Y. Wu, et al. 53-attosecond x-ray pulses reach the carbon k-edge. *Nat. Commun.*, 8(1):186, 2017.

[18] M. Garg, M. Zhan, T. T. Luu, H. Lakhotia, T. Klostermann, A. Guggenmos, and E. Goulielmakis. Multi-petahertz electronic metrology. *Nature*, 538(7625):359–363, 2016.

[19] M. I. Stockman, M. F. Kling, U. Kleineberg, and F. Krausz. Attosecond nanoplasmonic-field microscope. *Nat. Photonics*, 1(9):539–544, 2007.

[20] J. Ullrich, R. Moshammer, A. Dorn, R. Dörner, L. P. H. Schmidt, and H. Schmidt-Böcking. Recoil-ion and electron momentum spectroscopy: reaction-microscopes. *Rep. Prog. Phys.*, 66(9):1463, 2003.

[21] J. D. Jackson. *Classical electrodynamics.* New York : Wiley, cop. 1999, 1999.

[22] . Saleh, Bahaa E. A. and M. C. Teich. *Fundamentals of photonics. [Elektronisk resurs].* Wiley series in pure and applied optics. Hoboken, N.J. : Wiley, cop. 2007, 2007.

[23] G. Grynberg, A. Aspect, and C. Fabre. *Introduction to Quantum Optics. [Elektronisk resurs] : From the Semi-classical Approach to Quantized Light.* Cambridge : Cambridge University Press, 2010., 2010.

[24] T. Lang, A. Harth, J. Matyschok, T. Binhammer, M. Schultze, and U. Morgner. Impact of temporal, spatial and cascaded effects on the pulse formation in ultrabroadband parametric amplifiers. *Opt. Express*, 21(1):949–959, 2013.

[25] E. Goulielmakis, M. Uiberacker, R. Kienberger, A. Baltuska, V. Yakovlev, A. Scrinzi, T. Westerwalbesloh, U. Kleineberg, U. Heinzmann, M. Drescher, and F. Krausz. Direct measurement of light waves. *Science*, 305(5688):1267–1269, 2004.

[26] J. Armstrong. Measurement of picosecond laser pulse widths. *Appl. Phys. Lett.*, 10(1):16–18, 1967.

[27] R. Trebino, K. W. DeLong, D. N. Fittinghoff, J. N. Sweetser, M. A. Krumbügel, B. A. Richman, and D. J. Kane. Measuring ultrashort laser pulses in the time-frequency domain using frequency-resolved optical gating. *Rev. Sci. Instrum.*, 68(9):3277–3295, 1997.

[28] S. Akturk, C. D'Amico, and A. Mysyrowicz. Measuring ultrashort pulses in the single-cycle regime using frequency-resolved optical gating. *J. Opt. Soc. Am. B*, 25(6):A63–A69, 2008.

[29] C. Iaconis and I. A. Walmsley. Spectral phase interferometry for direct electric-field reconstruction of ultrashort optical pulses. *Opt. Lett.*, 23(10):792–794, 1998.

[30] V. V. Lozovoy, I. Pastirk, and M. Dantus. Multiphoton intrapulse interference. iv. ultrashort laser pulse spectral phase characterization and compensation. *Opt. Lett.*, 29(7):775–777, 2004.

[31] V. Loriot, G. Gitzinger, and N. Forget. Self-referenced characterization of femtosecond laser pulses by chirp scan. *Opt. Express*, 21(21):24879–24893, 2013.

[32] M. Miranda, C. L. Arnold, T. Fordell, F. Silva, B. Alonso, R. Weigand, A. L' Huillier, and H. Crespo. Characterization of broadband few-cycle laser pulses with the d-scan technique. *Opt. Express*, 20(17):18732–18743, 2012.

[33] S. Akturk, X. Gu, P. Bowlan, and R. Trebino. Spatio-temporal couplings in ultrashort laser pulses. *J. Opt.*, 12(9):093001, 2010.

[34] H. Vincenti and F. Quéré. Attosecond lighthouses: How to use spatiotemporally coupled light fields to generate isolated attosecond pulses. *Phys. Rev. Lett.*, 108:113904, 2012.

[35] K. T. Kim, C. Zhang, T. Ruchon, J.-F. Hergott, T. Auguste, D. Villeneuve, P. Corkum, and F. Quéré. Photonic streaking of attosecond pulse trains. *Nat. Photonics*, 7(8):651–656, 2013.

[36] G. Gariepy, J. Leach, K. T. Kim, T. J. Hammond, E. Frumker, R. W. Boyd, and P. B. Corkum. Creating high-harmonic beams with controlled orbital angular momentum. *Phys. Rev. Lett.*, 113:153901, 2014.

[37] F. Eilenberger, A. Brown, S. Minardi, and T. Pertsch. Imaging cross-correlation frog: measuring ultrashort, complex, spatiotemporal fields. *Opt. Express*, 21(22):25968–25976, 2013.

[38] T. Witting, F. Frank, W. A. Okell, C. A. Arrell, J. P. Marangos, and J. W. G. Tisch. Sub-4-fs laser pulse characterization by spatially resolved spectral shearing interferometry and attosecond streaking. *J. Phys. B: At., Mol. Opt. Phys.*, 45(7):074014, 2012.

[39] T. Witting, D. R. Austin, T. Barillot, D. Greening, P. Matia-Hernando, D. Walke, J. P. Marangos, and J. W. G. Tisch. Self-referenced characterization of space–time couplings in near-single-cycle laser pulses. *Opt. Lett.*, 41(10):2382–2385, 2016.

[40] G. Pariente, V. Gallet, A. Borot, O. Gobert, and F. Quéré. Space–time characterization of ultra-intense femtosecond laser beams. *Nat. Photonics*, 10(8):547–553, 2016.

[41] M. Miranda, T. Fordell, C. Arnold, A. L'Huillier, and H. Crespo. Simultaneous compression and characterization of ultrashort laser pulses using chirped mirrors and glass wedges. *Opt. Express*, 20(1):688–697, 2012.

[42] W. Hoppe. Beugung im inhomogenen primärstrahlwellenfeld. i. prinzip einer phasenmessung von elektronenbeungungsinterferenzen. *Acta Crystallogr. Sec. A*, 25(4):495–501, 1969.

[43] D. Fabris, W. Holgado, F. Silva, T. Witting, J. W. G. Tisch, and H. Crespo. Single-shot implementation of dispersion-scan for the characterization of ultrashort laser pulses. *Opt. Express*, 23(25):32803–32808, 2015.

[44] B. Bates, M. McDowell, and A. C. Newton. Correction of astigmatism in a czerny-turner spectrograph using a plane grating in divergent illumination. *J. Phys. E: Sci. Instrum.*, 3(3):206, 1970.

[45] D. R. Austin, T. Witting, and I. A. Walmsley. Broadband astigmatism-free czerny-turner imaging spectrometer using spherical mirrors. *Appl. Opt.*, 48(19):3846–3853, 2009.

[46] Y. An, Q. Sun, Y. Liu, C. Li, and Z.-Q. Wang. The design of astigmatism-free crossed czerny-turner spectrometer. *Optik*, 124(16):2539 – 2543, 2013.

[47] F. Böhle, M. Kretschmar, A. Jullien, M. Kovacs, M. Miranda, R. Romero, H. Crespo, U. Morgner, P. Simon, R. Lopez-Martens, et al. Compression of cep-stable multi-mj laser pulses down to 4 fs in long hollow fibers. *Laser Phys. Lett.*, 11(9):095401, 2014.

[48] J. Bromage, C. Dorrer, and J. D. Zuegel. Angular-dispersion-induced spatiotemporal aberrations in noncollinear optical parametric amplifiers. *Opt. Lett.*, 35(13):2251–2253, 2010.

[49] T. Hammond, G. G. Brown, K. T. Kim, D. Villeneuve, and P. Corkum. Attosecond pulses measured from the attosecond lighthouse. *Nat. Photonics*, 10(3):171, 2016.

[50] A. Mair, A. Vaziri, G. Weihs, and A. Zeilinger. Entanglement of the orbital angular momentum states of photons. *Nature*, 412(6844):313–316, 2001.

[51] J. E. Curtis, B. A. Koss, and D. G. Grier. Dynamic holographic optical tweezers. *Opt. Commun.*, 207(1):169 – 175, 2002.

[52] M. Zürch, C. Kern, P. Hansinger, A. Dreischuh, and C. Spielmann. Strong-field physics with singular light beams. *Nat. Phys.*, 8(10):743, 2012.

[53] L. Allen, M. W. Beijersbergen, R. J. C. Spreeuw, and J. P. Woerdman. Orbital angular momentum of light and the transformation of laguerre-gaussian laser modes. *Phys. Rev. A*, 45:8185–8189, 1992.

[54] K. Sueda, G. Miyaji, N. Miyanaga, and M. Nakatsuka. Laguerre-gaussian beam generated with a multilevel spiral phase plate for high intensity laser pulses. *Opt. Express*, 12(15):3548–3553, 2004.

[55] S. Carlström. *Sub-cycle control of strong-field processes on the attosecond timescale.* Lund : Division of Atomic Physics, Department of Physics, Lund University, 2017, 2017.

[56] J. L. Krause, K. J. Schafer, and K. C. Kulander. High-order harmonic generation from atoms and ions in the high intensity regime. *Phys. Rev. Lett.*, 68:3535–3538, 1992.

[57] P. B. Corkum. Plasma perspective on strong field multiphoton ionization. *Phys. Rev. Lett.*, 71(13):1994, 1993.

[58] A. L'Huillier, M. Lewenstein, P. Salières, P. Balcou, M. Y. Ivanov, J. Larsson, and C. G. Wahlström. High-order harmonic-generation cutoff. *Phys. Rev. A*, 48(5):R3433–R3436, 1993.

[59] M. Lewenstein, P. Balcou, M. Y. Ivanov, A. L' huillier, and P. B. Corkum. Theory of high-harmonic generation by low-frequency laser fields. *Phys. Rev. A*, 49(3):2117, 1994.

[60] Y. Mairesse, A. de Bohan, L. J. Frasinski, H. Merdji, L. C. Dinu, P. Monchicourt, P. Breger, M. Kovačev, R. Taïeb, B. Carré, H. G. Muller, P. Agostini, and P. Salières. Attosecond synchronization of high-harmonic soft x-rays. *Science*, 302(5650):1540–1543, 2003.

[61] K. Varjú, Y. Mairesse, B. Carré, M. Gaarde, P. Johnsson, S. Kazamias, R. López-Martens, J. Mauritsson, K. Schafer, P. Balcou, et al. Frequency chirp of harmonic and attosecond pulses. *J. Mod. Opt.*, 52(2-3):379–394, 2005.

[62] M. Murakami, J. Mauritsson, and M. B. Gaarde. Frequency-chirp rates of harmonics driven by a few-cycle pulse. *Phys. Rev. A*, 72:023413, 2005.

[63] N. Dudovich, O. Smirnova, J. Levesque, Y. Mairesse, M. Y. Ivanov, D. Villeneuve, and P. B. Corkum. Measuring and controlling the birth of attosecond xuv pulses. *Nat. Phys.*, 2(11):781–786, 2006.

[64] E. Mansten. *Measurement and control of attosecond light fields.* Lund reports on atomic physics: 406. Lund : Department of Physics, Faculty of Engineering, Lund University, 2009, 2009.

[65] D. Shafir, H. Soifer, B. D. Bruner, M. Dagan, Y. Mairesse, S. Patchkovskii, M. Y. Ivanov, O. Smirnova, and N. Dudovich. Resolving the time when an electron exits a tunnelling barrier. *Nature*, 485(7398):343–346, 2012.

[66] S. Carlström, J. Preclíková, E. Lorek, E. W. Larsen, C. M. Heyl, D. Paleček, D. Zigmantas, K. J. Schafer, M. B. Gaarde, and J. Mauritsson. Spatially and spectrally resolved quantum path interference with chirped driving pulses. *New J. Phys.*, 18(12):123032, 2016.

[67] M. Ammosov, N. Delone, and V. Krainov. Tunnelling ionization of complex atoms and of atomic ions in an alternating electromagnetic field. *Sov. Phys. JETP*, 64(6):1191–1194, 1986.

[68] J. Samson and W. C. Stolte. Precision measurements of the total photoionization cross-sections of he, ne, ar, kr, and xe. *J. Electron Spectrosc. Relat. Phenom.*, 123(2):265–276, 2002.

[69] C. M. Heyl, C. L. Arnold, A. Couairon, and A. L' Huillier. Introduction to macroscopic power scaling principles for high-order harmonic generation. *J. Phys. B: At., Mol. Opt. Phys.*, 50(1):013001, 2017.

[70] C. M. Heyl. *Scaling and gating attosecond pulse generation.* Lund reports on atomic physics: 496. Lund : Division of Atomic Physics, Department of Physics, Faculty of Egineering, Lund University ; Marburg : Department of Physics, Philipps-Universität Marburg/University of Marburg, 2014, 2014.

[71] C. Heyl, H. Coudert-Alteirac, M. Miranda, M. Louisy, K. Kovacs, V. Tosa, E. Balogh, K. Varjú, A. L' Huillier, A. Couairon, et al. Scale-invariant nonlinear optics in gases. *Optica*, 3(1):75–81, 2016.

[72] E. Lorek, E. W. Larsen, C. M. Heyl, S. Carlström, D. Paleček, D. Zigmantas, and J. Mauritsson. High-order harmonic generation using a high-repetition-rate turnkey laser. *Rev. Sci. Instrum.*, 85(12):123106, 2014.

[73] T. Harada and T. Kita. Mechanically ruled aberration-corrected concave gratings. *Appl. Opt.*, 19(23):3987–3993, 1980.

[74] G. Bird. *The DSMC Method*. CreateSpace Independent Publishing Platform, 2013.

[75] J. W. Cooper. Photoionization from outer atomic subshells. a model study. *Phys. Rev.*, 128(2):681–693, 1962.

[76] M. Krebs, S. Hädrich, S. Demmler, J. Rothhardt, A. Zaïr, L. Chipperfield, J. Limpert, and A. Tünnermann. Towards isolated attosecond pulses at megahertz repetition rates. *Nat. Photonics*, 7(7):555–559, 2013.

[77] E. Mansten, J. Dahlström, J. Mauritsson, T. Ruchon, A. L' Huillier, J. Tate, M. Gaarde, P. Eckle, A. Guandalini, M. Holler, et al. Spectral signature of short attosecond pulse trains. *Phys. Rev. Lett.*, 102(8):083002, 2009.

[78] W. Holgado, C. Hernández-García, B. Alonso, M. Miranda, F. Silva, L. Plaja, H. Crespo, and I. Sola. Continuous spectra in high-harmonic generation driven by multicycle laser pulses. *Phys. Rev. A*, 93(1):013816, 2016.

[79] W. Holgado, C. Hernández-García, B. Alonso, M. Miranda, F. Silva, O. Varela, J. Hernández-Toro, L. Plaja, H. Crespo, and I. J. Sola. Tunable high-harmonic generation by chromatic focusing of few-cycle laser pulses. *Phys. Rev. A*, 95:063823, 2017.

[80] H. Muller. Reconstruction of attosecond harmonic beating by interference of two-photon transitions. *Appl. Phys. B*, 74(1):s17–s21, 2002.

[81] Y. Mairesse and F. Quéré. Frequency-resolved optical gating for complete reconstruction of attosecond bursts. *Phys. Rev. A*, 71(1):011401, 2005.

[82] V. G. Veselago. The electrodynamics of substances with simultaneously negative values of ϵ and μ. *Soviet Physics Uspekhi*, (4):509, 1968.

[83] R. H. Ritchie. Plasma losses by fast electrons in thin films. *Phys. Rev.*, 106:874–881, 1957.

[84] P. K. Jain, X. Huang, I. H. El-Sayed, and M. A. El-Sayed. Review of some interesting surface plasmon resonance-enhanced properties of noble metal nanoparticles and their applications to biosystems. *Plasmonics*, 2(3):107–118, 2007.

[85] D. R. Smith, J. B. Pendry, and M. C. Wiltshire. Metamaterials and negative refractive index. *Science*, 305(5685):788–792, 2004.

[86] W. Cai, U. K. Chettiar, A. V. Kildishev, and V. M. Shalaev. Optical cloaking with metamaterials. *Nat. Photonics*, 1(4):224–227, 2007.

[87] W. L. Barnes, A. Dereux, and T. W. Ebbesen. Surface plasmon subwavelength optics. *Nature*, 424(6950):824, 2003.

[88] E. Mårsell, C. L. Arnold, E. Lorek, D. Guenot, T. Fordell, M. Miranda, J. Mauritsson, H. Xu, A. L'Huillier, and A. Mikkelsen. Secondary electron imaging of nanostructures using extreme ultra-violet attosecond pulse trains and infra-red femtosecond pulses. *Ann. Phys.*, 525(1-2):162–170, 2013.

[89] S. A. Maier. *Plasmonics: Fundamentals and Applications*. Springer, 2007.

[90] L. Tonks and I. Langmuir. Oscillations in ionized gases. *Phys. Rev.*, 33:195–210, 1929.

[91] C. Kittel. *Introduction to solid state physics.* New York : Wiley, cop. 1996, 1996.

[92] D. Hoff, M. Kruger, L. Maisenbacher, A. M. Sayler, G. G. Paulus, and P. Hommelhoff. Tracing the phase of focused broadband laser pulses. *Nat. Phys.*, advance online publication, 2017.

[93] A. Einstein. Über einen die erzeugung und verwandlung des lichtes betreffenden heuristischen gesichtspunkt. *Ann. Phys.*, 322(6):132–148, 1905.

[94] S. Hüfner. *Photoelectron spectroscopy : principles and applications.* Advanced texts in physics. Berlin : Springer, cop. 2003, 2003.

[95] O. Schmidt, M. Bauer, C. Wiemann, R. Porath, M. Scharte, O. Andreyev, G. Schönhense, and M. Aeschlimann. Time-resolved two photon photoemission electron microscopy. *Appl. Phys. B*, 74(3):223–227, 2002.

[96] A. Kubo, K. Onda, H. Petek, Z. Sun, Y. S. Jung, and H. K. Kim. Femtosecond imaging of surface plasmon dynamics in a nanostructured silver film. *Nano Lett.*, 5(6):1123–1127, 2005. PMID: 15943454.

[97] L. D. Landau and E. M. Lifšic. *Electrodynamics of continuous media.* Course of theoretical physics: 8. Oxford : Pergamon, 1960, 1960.

[98] S. Kim, J. Jin, Y.-J. Kim, I.-Y. Park, Y. Kim, and S.-W. Kim. High-harmonic generation by resonant plasmon field enhancement. *Nature*, 453(7196):757–760, 2008.

[99] J. Rothhardt, M. Krebs, S. Hädrich, S. Demmler, J. Limpert, and A. Tünnermann. Absorption-limited and phase-matched high harmonic generation in the tight focusing regime. *New J. Phys.*, 16(3):033022, 2014.

[100] A. Cingöz, D. C. Yost, T. K. Allison, A. Ruehl, M. E. Fermann, I. Hartl, and J. Ye. Direct frequency comb spectroscopy in the extreme ultraviolet. *Nature*, 482(7383):68–71, 2012.

[101] B. E. Schmidt, N. Thiré, M. Boivin, A. Laramée, F. Poitras, G. Lebrun, T. Ozaki, H. Ibrahim, and F. Légaré. Frequency domain optical parametric amplification. *Nat. Commun.*, 5, 2014.

[102] J. Ahrens, O. Prochnow, T. Binhammer, T. Lang, B. Schulz, M. Frede, and U. Morgner. Multipass opcpa system at 100 khz pumped by a cpa-free solid-state amplifier. *Opt. Express*, 24(8):8074–8080, 2016.

[103] M. Louisy, C. Arnold, M. Miranda, E. Larsen, S. N. Bengtsson, D. Kroon, M. Kotur, D. Guénot, L. Rading, P. Rudawski, et al. Gating attosecond pulses in a noncollinear geometry. *Optica*, 2(6):563–566, 2015.

[104] I. Sola, E. Mével, L. Elouga, E. Constant, V. Strelkov, L. Poletto, P. Villoresi, E. Benedetti, J.-P. Caumes, S. Stagira, et al. Controlling attosecond electron dynamics by phase-stabilized polarization gating. *Nat. Phys.*, 2(5):319–322, 2006.

[105] M. Gisselbrecht, A. Huetz, M. Lavollée, T. J. Reddish, and D. P. Seccombe. Optimization of momentum imaging systems using electric and magnetic fields. *Rev. Sci. Instrum.*, 76(1):013105, 2005.

Printed by Media-Tryck, Lund 2017 NORDIC ECOLABEL, 3041 0903

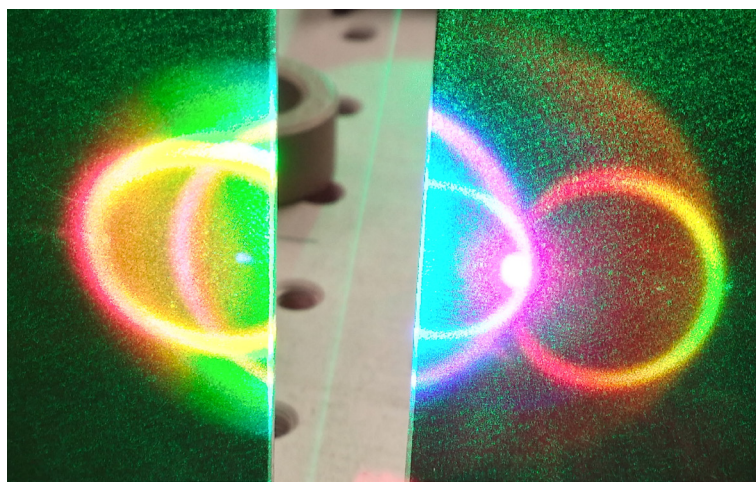

LUND UNIVERSITY

Faculty of Engineering, LTH
Department of Physics
Division of Atomic Physics

ISBN: 978-91-7753-557-7 (print)
ISBN: 978-91-7753-558-4 (pdf)
ISSN 0281-276